Soft X-ray diffraction imaging with and without lenses

and

Radiation damage studies

A Dissertation Presented

by

Tobias Beetz

to

The Graduate School

in Partial Fulfillment of the Requirements

for the Degree of

Doctor of Philosophy

in

Physics

Stony Brook University

May 2004

State University of New York
at Stony Brook

The Graduate School

Tobias Beetz

We, the dissertation committee for the above candidate for the Doctor of Philosophy degree, hereby recommend acceptance of the dissertation.

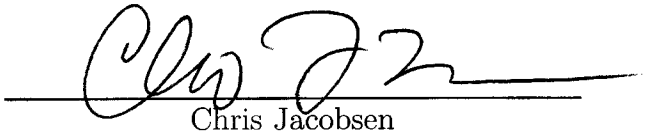

Chris Jacobsen
Professor
Department of Physics and Astronomy, Stony Brook

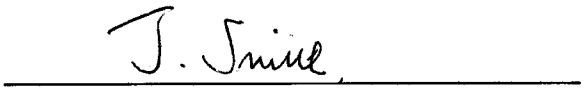

Jack Smith
Professor
Department of Physics and Astronomy, Stony Brook

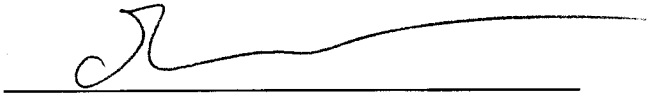

Thomas Weinacht
Assistant Professor
Department of Physics and Astronomy, Stony Brook

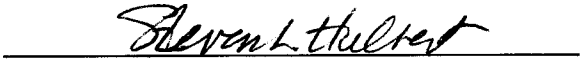

Steven Hulbert
Physicist
Brookhaven National Laboratory

This dissertation is accepted by the Graduate School.

Graduate School

Abstract of the Dissertation

Soft X-ray diffraction imaging with and without lenses

and

Radiation damage studies

by

Tobias Beetz

Doctor of Philosophy

in

Physics

Stony Brook University

2004

Conventional tomography in soft X-ray microscopes has delivered 100-200 nm 3D images of biological specimens. As the transverse resolution - roughly given by the width of the outermost zone of the zone plate - is further improved, the depth of focus decreases as the square of the outermost zone width presenting a challenge to improved resolution in this approach. One solution to this dilemma is not to record images, but to record holograms of the specimen. In this thesis, we show that this can be done by magnifying the far-field hologram with a zone plate onto a CCD camera. This allows for fast data acquisition, making 3D imaging feasible. We describe the development of a new experimental apparatus to record the

holograms, together with experimental results obtained at the National Synchrotron Light Source. In addition, lensless diffraction imaging has the potential to overcome the resolution limitations imposed by zone plates. We describe lensless diffraction imaging experiments done at the Advanced Light Source together with obtained 2D and 3D reconstructions. Finally, it has been shown that radiation damage sets a fundamental limit to studies with ionizing radiation; cryo methods are known to ease these limits. We report measurements on mass loss and decrease in C=O bond strength as measured by oxygen edge XANES (NEXAFS) spectroscopy in thin films of poly(methyl methacrylate), or PMMA, studied in a vacuum at room temperature and at liquid nitrogen temperature.

To Meghan and my parents.

Contents

List of Figures **ix**

List of Tables **xii**

Acknowledgements **xiii**

1 Imaging with X rays **1**
1.1 X-ray interactions with matter 2
1.2 X-ray sources 8
1.3 Lenses for X rays - zone plates 11
1.3.1 Zone plate properties 12
1.3.2 Transverse resolution 13
1.3.3 Longitudinal resolution or Depth of focus 13
1.4 X-ray microscopy 13

2 Experimental setup **18**
2.1 Experimental chamber 19
2.1.1 Goniometer and sample holder 20
2.1.2 Motor stages and drive electronics 24
2.1.3 Detector system 27
2.1.4 Vacuum system 30
2.1.5 Control software 30
2.1.6 Chamber and support system 32
2.2 National Synchrotron Light Source beamline X1-A 32
2.3 Advanced Light Source beamline 9.0.1 37
2.3.1 Properties of the zone plate monochromator 40
2.3.2 Choosing the right photon energy 49

3 In-line (Gabor) holography **52**
3.1 Fundamentals of holography 53
3.1.1 The hologram as a superposition of zone plates 54

3.1.2 Hologram reconstruction 56
3.1.3 Empty specimen requirement 58
3.1.4 How many fringes do we need to detect? 58
3.1.5 Fringe visibility 59
3.1.6 Coherence requirements in holography 59
3.1.7 Detector resolution 62
3.1.8 3D in-line holography 62
3.2 A brief history of in-line holography 64
3.3 Experimental realization of Gabor holography 66
3.3.1 Detector 66
3.3.2 Experimental geometry 67
3.4 First holography data set 70
3.4.1 Experimental setup 70
3.4.2 The data and analysis 71
3.4.3 IDL simulations 73
3.5 Second holography data set 76
3.5.1 The modified experimental setup 76
3.5.2 Data collection 77
3.5.3 Reconstruction 77
3.6 Discussion and the future of in-line holography 79

4 Diffraction imaging **82**
4.1 Fundamentals of diffraction imaging 83
4.1.1 The phase problem 83
4.1.2 Nyquist-Shannon sampling theorem 84
4.1.3 Implications of the Nyquist-Shannon sampling theorem on diffraction imaging 85
4.1.4 Resolution in a diffraction pattern 88
4.1.5 Oversampling ratio 89
4.1.6 Field of view 90
4.1.7 Coherence requirements in diffraction imaging 90
4.2 A brief history of diffraction imaging 93
4.3 Reconstructing diffraction patterns 94
4.4 Experimental demonstration 96
4.4.1 The sample 96
4.4.2 Experimental conditions 97
4.4.3 Combining diffraction with imaging/holography 98
4.4.4 Reconstruction of the experimental data 106
4.5 Extending diffraction imaging to 3D 111
4.6 Discussion and future developments 111

5 Radiation damage **114**
5.1 Fundamentals of radiation damage 115
5.1.1 Radiation dose 115
5.2 Image resolution 116
5.3 Cryo fixation to improve radiation resistance 120
5.4 Cryo fixation to preserve chemical states - a study in PMMA . 121
5.4.1 Experimental description 122
5.4.2 Results 124
5.4.3 Implications 127
5.5 Conclusions 127

A Propagation **128**
A.1 Propagation in IDL 129

B Motor amplifier box **130**

C Multimedia CD **137**
C.1 Progress of the reconstruction algorithm 137
C.2 3D reconstruction 137

D The Fourier transform and its properties **138**

E Protocol for zone plate imaging with the diffraction chamber **140**

F Soft X-ray radiation damage studies in PMMA using a cryo STXM (reprint) **143**

G List of Publications **148**

Bibliography **150**

List of Figures

1.1 Carbon and water penetration depth as a function of energy . 5
1.2 Photon cross sections 7
1.3 Schematic of an undulator 9
1.4 Brightness of X-ray sources 10
1.5 Schematic of a zone plate 12
1.6 Comparison of TXM and STXM 14
1.7 Zone plate and order-sorting aperture 16
1.8 Schematic of the cryo-STXM 17

2.1 Schematic of the chamber elements 20
2.2 JEOL goniometer system 21
2.3 Schematic of JEOL goniometer system 22
2.4 Schematic of JEOL main drive with vacuum fittings 23
2.5 Gatan cryo sample holder 25
2.6 JEOL room-temperature sample holder 25
2.7 Motorized stages for optics 26
2.8 CCD camera with beamstop and photodiode stages. 29
2.9 Control software structure 31
2.10 Graphical User Interface (GUI) 33
2.11 Graphical User Interface to control devices 34
2.12 Calculated X1 undulator output 35
2.13 Schematic of the NSLS X1-A beamline 36
2.14 Schematic of optics X1-A2 beamline 37
2.15 Schematic of the ALS beamline 9.0.1 38
2.16 Layout of the ALS beamline 9.0.1 38
2.17 Schematic of the ALS 9.0.1 zone plate monochromator 39
2.18 View of the ALS 9.0.1 endstation 40
2.19 Schematic of the horizontal plane at ALS beamline 9.0.1 . . . 42
2.20 Zone plate monochromator spectra in dependence of the horizontal Beryllium window position 44
2.21 Profile of the zone plate monochromator 45

2.22 Speckle from a collection of 50 nm diameter gold spheres . . . 49
2.23 Spectrum of the ALS zone plate monochromator 50

3.1 General holography setup 53
3.2 The hologram as a superposition of zone plates 54
3.3 Hologram reconstruction 57
3.4 Plane and volume diffraction grating 63
3.5 Principle of 3D in-line holography 64
3.6 In-line holography using a zone plate 67
3.7 Gabor holography using a zone plate 68
3.8 Holograms of 1 μm diameter latex spheres. 72
3.9 Mapping the zone plate 73
3.10 Computer simuation - pinhole and off-axis zone plate 74
3.11 Computer simulation - fringes due to an off-axis zone plate . . 75
3.12 Computer simulation - magnified view of the positive first-order image 75
3.13 Modified experimental setup for recording in-line holograms using a CCD 76
3.14 Hologram of latex spheres and a gold dot 78
3.15 Focus scan 78
3.16 Latex spheres reconstruction 79
3.17 Gold sphere reconstruction 80

4.1 Nyquist-Shannon sampling theorem 84
4.2 Implications of the Nyquist-Shannon sampling theorem 86
4.3 Demonstration of sampling the diffraction pattern 87
4.4 Schematic of the diffraction geometry 88
4.5 Schematic of reconstruction algorithm 95
4.6 View of the pyramid sample 97
4.7 Experimental schematic diagram for diffraction imaging 98
4.8 Usage of the window corner to record a clean diffraction pattern 99
4.9 Demonstration of missing low spatial frequency information . 100
4.10 Diffraction patterns with different exposure times 101
4.11 Combined diffraction pattern of the pyramid sample 102
4.12 Zone plate image of the pyramid sample 104
4.13 Patching the diffraction pattern with a zone plate image . . . 106
4.14 Combined diffraction pattern 107
4.15 Pyramid reconstruction 108
4.16 Goodness-of-fit for pyramid reconstruction 109

5.1 Radiation damage in a glutaraldehyde-fixed *Vicia faba* chromosome 116
5.2 Resolution vs. Dose 118
5.3 Fading of diffraction spots 120
5.4 Mass loss from Epon 812 for different temperatures 121
5.5 Chemical structure of PMMA 123
5.6 Area scan of damaged PMMA region 124
5.7 Oxygen XANES spectra of PMMA in dependence of the dose and the temperature 125
5.8 Loss of C=O peak intensity and mass loss as a function of dose and temperature 126

A.1 Schematic diagram of the Fresnel-Kirchhoff diffraction formalism 128

B.1 Connections to the motor amplifier box 131

E.1 Zone plate imaging protocol with the new chamber 142

List of Tables

2.1 Zone plate monochromator parameters 41
2.2 Parameters of the ALS storage ring and ALS 9.0.1 beamline . 42

3.1 Experimental parameters of the first holography experiment . 71
3.2 Experimental parameters of the second holography experiment 77

4.1 Experimental parameters for the diffraction experiment 101

Acknowledgements

There are so many people that have contributed to the work presented here and/or to my life besides school. Here is my attempt to remember everyone and to keep it significantly shorter than the rest of the dissertation.

I would like to start by saying a big "Thank you!" to my advisor Chris Jacobsen. Working with Chris during my first year as an exchange student made me decide to stay on at Stony Brook and get my PhD. That is one decision I will never regret. He has always been available to give me good advice on my professional career as well as on personal issues. I will always be amazed by the energy that Chris has in all aspects of life. Janos Kirz has always given me great advice on the many occasions I was stuck at the beamline and thought that nothing would work. I am glad that I had his help and I also really enjoyed the many parties he and Gina had at their house. Michael Feser has been a colleague and friend since my first year at Stony Brook. He introduced me to the instrumentation and software while we were working on STXM4 and always made sure that I understood whatever he explained. Thanks for all the discussions, zone plate monochromators, trips, parties and Baileys! Sue Wirick has been essential in making it through the days and nights at the beamline. Her caring for me has always brightened up my days. I would like to thank Benjamin Hornberger, Holger Fleckenstein, David Shapiro, and Enju Lima for many stimulating discussion and help.

The development of the new experimental chamber was possible with the help of Chris Jacobsen who brought in the money to pay for everything, wrote an impressive amount of the control software and led the project in the right direction. Janos Kirz contributed to many aspects of the experimental chamber including arrangements for moving and setup of the experiment at the ALS. David Shapiro took on the design of several mechanical assemblies and the implementation of a vacuum interlock system. Enju Lima has helped programming the Graphical User Interface. The efforts were supported by Chi-Chang Kao's group at BNL. Onur Mentes took over the design of the CCD section together with the programming of the CCD. Cecilia Sanchez-Hanke designed the cold trap and took care of choosing a pumping system for

the apparatus. I am also thankful to the many people at the Stony Brook electronics and machine shop, the NSLS, and the ALS who have helped at various stages of the development of the apparatus.

The experiments at the ALS were made possible with the help of Malcolm Howells. I really enjoyed working with him during my time at Berkeley. Thanks also for the great dinners that we had and for letting us enjoy your house during our trip. Thanks to Stefano Marchesini for a productive time at the ALS as well as for his hospitality. I very much enjoyed the dinners, movies, and the Bhangra party with Madhu. After hearing great things about Henry Chapman for many years, I finally got to meet and work with him and see why I heard all those great things about him. Thank you so much for all of your help! I am also thankful to John Spence, Haifeng He and Uwe Weierstall who are part of the west-coast team. Thanks to all of them for letting me join the diffraction imaging efforts at Berkeley and for making it a successful project.

I wish to thank Malcolm Howells and Janos Kirz for sharing their calculations on radiation damage. Michael Feser and Barry Winn have helped me many times during my software and hardware struggles while using the cryo-STXM and Jaan Mannik helped with the PMMA sample preparation.

My parents have supported and encouraged me throughout my life whenever they could, even after I decided to not go back to Germany after my first year. For that, I will always be thankful. Thanks to my sister and her family for all those phone calls and their hospitality (You still have a few more years to visit us on Long Island!). Diane and Lee have always taken interest in my work and life and I am glad that they did.

I am thankful for all my friends that I had throughout the years and who have filled my last few years with joy. Thanks to Benjamin, Holger, Anke, Xoch and Nathan, Michael and Juana, Tanya, Max, Lauren, Jeff, Onur, Anja, Thorsten, Nicole, Finn and Peer, Uli, Sven, Francis, Darja, Donna and Arty, Christian, Markus, Katja, Ela, Andi, Kiki, Mirna, Alexis and Christian, Ryan, Tante Britta and Onkel Günther, Lucas, Pete, Tom and Stacy, Gram, Uncle Marky, Jack, Debbie, Lynn and Steve.

I also thank the organizers of the Universität Würzburg for making it possible for me to come to Stony Brook and the German Academic Exchange Program (DAAD) for financial support during my first year. I am thankful to the staff of the Stony Brook Physics department. The members of my thesis committee deserve special recognition for reading and greatly improving this thesis.

Meghan - thank you for being my partner, for being my stress outlet, for sharing the trips that we have taken, for the many cakes and cookies you baked, for the love, attention, and patience that you have given, for listening

to endless practice talks, for the laughter that you have brought into my life, for being there whenever I needed you, for all the little things that I have learned to appreciate, for sticking through the hard times, for proof-reading my thesis, for reminding me of deadlines, for all the sunsets at West Meadow, for singing and dancing, and for so many other things ... THANK YOU!

Chapter 1

Imaging with X rays

This chapter describes the interactions of X rays with matter, along with available X-ray sources. In addition, an overview of the properties of zone plate lenses used in this dissertation is given together with a description of the existing X-ray microscopes at Stony Brook.

1.1 X-ray interactions with matter

That X rays are electromagnetic waves was first demonstrated by Laue from X-ray diffraction patterns. Electromagnetic waves are solutions to the wave equation, derived from Maxwell's equations [Jackson 1975]. When an electromagnetic wave is incident on an atom's electrons, it will force the electrons to oscillate around their equilibrium position. This motion can be described as a series of damped harmonic oscillators with the incident oscillatory electric field $\vec{E}$ of the X-ray as the driving force. The displacement $\vec{x}$ of an electron from its equilibrium position leads to a **dipole moment** $\vec{p}$ of the atom

$$\begin{aligned} \vec{p} &= -e\vec{x} \\ &= \frac{e^2}{m_e} \cdot \frac{1}{\omega_0^2 - \omega^2 - i\omega\gamma} \vec{E}, \end{aligned} \tag{1.1}$$

where m_e is the mass of the electron, and γ is the damping constant. In a medium consisting of many atoms, this effect results in a bulk **polarization** P of the medium. The polarization is related to the electric field by the **electric susceptibility** χ_e

$$\vec{P} = \epsilon_0 \chi_e \vec{E}. \tag{1.2}$$

From Eq. (1.1), the electric susceptibility becomes

$$\begin{aligned} \chi_e &= \frac{n_a e^2}{\epsilon_0 m_e} \sum_j \frac{F_j}{\omega_j^2 - \omega^2 - i\omega\gamma_j} \\ &= \frac{n_a r_e \lambda^2}{4\pi^2 \epsilon_0} \sum_j \frac{\omega^2 F_j}{\omega_j^2 - \omega^2 - i\omega\gamma_j}. \end{aligned} \tag{1.3}$$

Here, $r_e = e^2/m_e c^2$ is the classical radius of the electron, n_a is the number of atoms per unit volume, and we have to sum over all oscillator indices. We have also assumed, that each electron has a binding frequency ω_j, an oscillator strength F_j and a damping constant γ_j [Jackson 1975]. The sum over all oscillator strengths is

$$\sum_j F_j = Z, \tag{1.4}$$

where Z is the total number of electrons. If we have a mixture of different atoms, Eq. (1.3) is going to be a weighted sum over the different atom types.

For X rays, the frequency ω of the incident wave is much higher than the resonant frequency ω_j of most oscillators ($\omega \gg \omega_j$), meaning that the incident photon energy is much bigger than the binding energies. In addition to that, the absorption per wavelength for X rays is negligible. Therefore the damping constants γ_j are generally small ($\gamma/\omega \ll 1$) and can be neglected ($\gamma \to 0$). We can then write Eq. (1.3) as

$$\begin{aligned} \chi_e &= -\frac{n_a r_e \lambda^2}{4\pi^2 \epsilon_0} \sum_j F_j \\ &= -\frac{n_a r_e \lambda^2}{4\pi^2 \epsilon_0} Z \end{aligned} \tag{1.5}$$

The electric susceptibility is also expressed in terms of the **dielectric constant** ϵ of a medium as

$$\epsilon = \epsilon_0(1 + \chi_e). \tag{1.6}$$

Complex index of refraction.

We can now introduce the **index of refraction** n in a medium where the wavevector is $k = 2\pi/\lambda$ as

$$\begin{aligned} n &= \frac{k}{k_0} \\ &= \frac{\sqrt{\mu\epsilon}\omega}{\sqrt{\mu_0\epsilon_0}\omega}. \end{aligned}$$

Here we have used the **magnetic permeability** μ, which is expressed as

$$\mu = \mu_0(1 + \chi_m), \tag{1.7}$$

in analogy with Eq. (1.6) for the dielectric constant. Inserting both equations into Eq. (1.7) gives

$$\begin{aligned} n &= \sqrt{(1+\chi_e)(1+\chi_m)} \\ &\simeq \sqrt{1+\chi_e} \\ &\simeq 1 + \frac{1}{2}\chi_e + ..., \end{aligned} \tag{1.8}$$

where we have used the fact that the electric susceptibility is small compared to 1, and neglected the even smaller magnetic susceptibility. Inserting the

result for the electric susceptibility from Eq. (1.5) we end up with

$$n \approx 1 - \frac{1}{2}\frac{n_a r_e \lambda^2}{4\pi^2 \epsilon_0} \sum_j F_j. \tag{1.9}$$

For X rays, Eq. (1.9) is generally written as

$$n = 1 - \delta - i\beta \tag{1.10}$$

$$= 1 - \frac{n_a r_e \lambda^2}{2\pi}(f_1 + i f_2), \tag{1.11}$$

where

$$\delta = \frac{n_a r_e \lambda^2}{2\pi} f_1 \tag{1.12}$$

and

$$\beta = \frac{n_a r_e \lambda^2}{2\pi} f_2. \tag{1.13}$$

The quantity $f = f_1 + i f_2$ is also called the **atomic scattering factor**, where f_1 represents the effective number of electrons that phase shift the wave and f_2 the attenuation. Henke *et al.* [Henke 1993] tabulated the values for f_1 and f_2 and found that f_1 is usually positive and f_2 is always positive (corresponding to absorption).

Absorption and phase shift

Let us look at a plane wave with amplitude ψ_0, and initial wavevector k, incident on a material with thickness z. The amplitude of the wave after the material is

$$\psi = \psi_0 e^{-ikn z} \tag{1.14}$$

$$= \psi_0 e^{-ikz} e^{ik\delta z} e^{-k\beta z}.$$

If we are just interested in the intensity, we find

$$\begin{aligned} I &= \psi^\star \cdot \psi \\ &= \psi_0 (e^{ikz} e^{-ik\delta z} e^{-k\beta z}) \cdot \psi_0 (e^{-ikz} e^{ik\delta z} e^{-k\beta z}) \\ &= I_0 e^{-2k\beta z} \\ &= I_0 e^{-\mu z}, \end{aligned} \tag{1.15}$$

where $I_0 = \psi_0^2$ and we have introduced the **attenuation coefficient** μ as

$$\begin{aligned} \mu &= 2k\beta \\ &= \frac{4\pi\beta}{\lambda}. \end{aligned} \tag{1.16}$$

Eq. (1.15) is also called Beer's law and describes the absorption due to matter. We can express Eq. (1.16) in terms of f_2 from Eq. (1.13) and end up with

$$\mu = 2k\frac{n_a r_e \lambda^2}{2\pi} f_2. \tag{1.17}$$

Figure 1.1 shows the interaction length $1/\mu$ for soft X rays in carbon and water. The energy range between 284 eV (carbon K-edge) and 530 eV

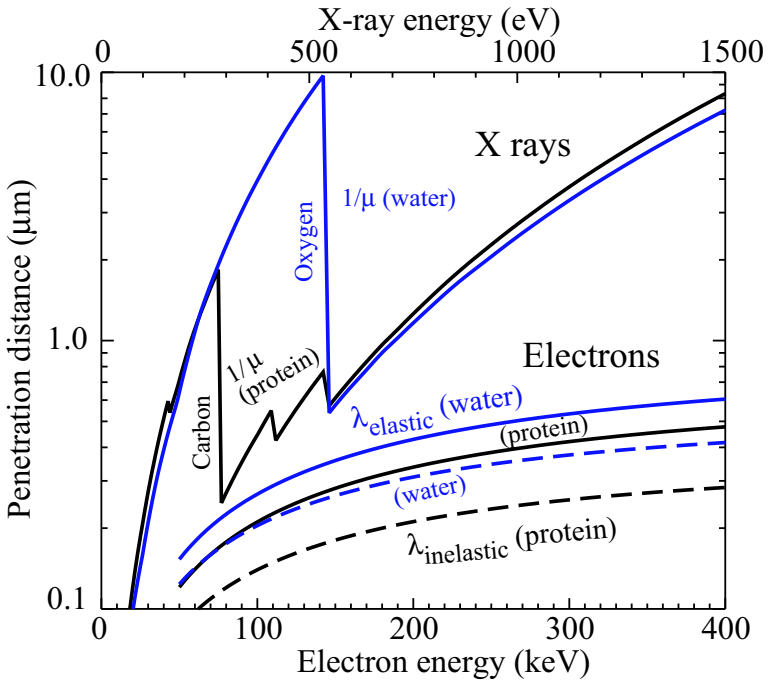

Figure 1.1: Interaction length $1/\mu$ for soft X rays in carbon and water, showing large contrast in the water window. The interaction length for electrons is plotted for comparison. [reprinted from [Kirz 1995]].

(oxygen K-edge) is called the **water window**. In that energy region, carbon

is absorbent whereas water is transparent, providing a natural contrast for organic specimens. The electron interaction length (defined in the same way as Eq. (1.15) for X rays) is also plotted in Figure 1.1 for comparison. There is no water window for electrons so that the contrast of organic material in a thin layer of water or ice is very low. To get some natural contrast, electron microscopists usually defocus the electron beam, to get an image with some phase contrast. In addition to the contrast, one also sees that the overall size of specimens can be much larger when using X rays, since the X-ray absorption is much less than the electron absorption. This is of great advantage when imaging whole biological cells *in vitro*, which can be several microns thick.

In addition to the absorption, there is a phase change given by

$$\Delta\varphi \;=\; k\delta z = \frac{2\pi}{\lambda}\delta z. \tag{1.18}$$

Using Eq. (1.12) this becomes

$$\Delta\varphi \;=\; \frac{2\pi}{\lambda}\frac{n_a r_e \lambda^2}{2\pi} f_1 z. \tag{1.19}$$

In both equations the factor δ and f_1 are properties of the medium and have been tabulated by Henke *et al.* [Henke 1982].

Cross section

When an X ray is incident on matter, the interaction between the electromagnetic wave and the electrons in the matter can be described by one of the following processes:

- **Photoelectric absorption** - the incident photon is absorbed by an atom, giving rise to characteristic absorption spectra
- **Elastic (coherent) scattering** - the photon is coherently scattered off an electron without loss in energy
- **Inelastic (incoherent or Compton) scattering** - the photon is scattered off an electron and loses some of its energy to the electron. Such a scattering process is incoherent.

Figure 1.2 shows the cross sections in carbon for photoelectric absorption σ_{ab}, coherent scattering σ_{coh}, and incoherent scattering σ_{inc} based on data from Henke *et al.* [Henke 1993] and Hubbell *et al.* [Hubbell 1980]. It is evident that inelastic scattering cross section is small for X-ray energies smaller than

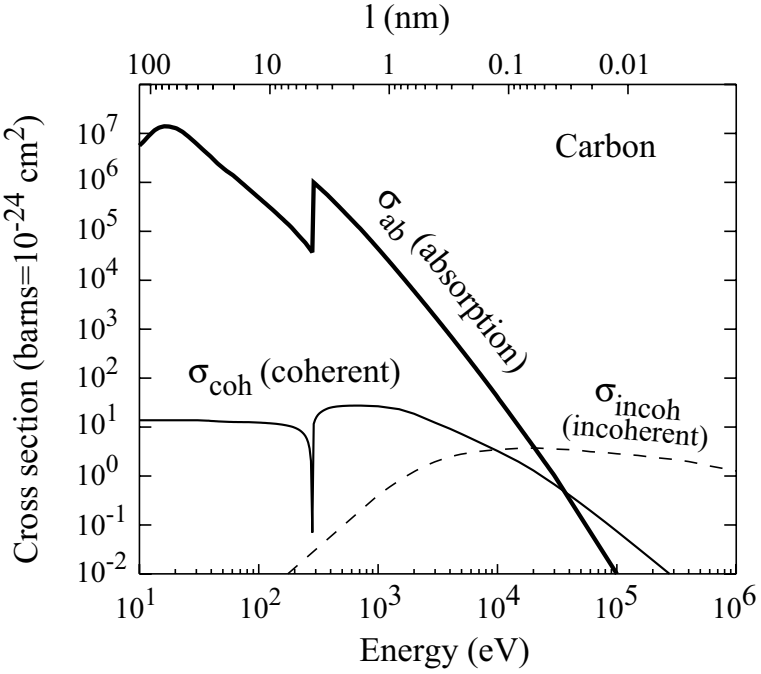

Figure 1.2: Photon cross sections in carbon, showing the contributions of photoelectric absorption $\sigma_{\rm ab}$, coherent scattering $\sigma_{\rm coh}$, and incoherent scattering $\sigma_{\rm inc}$. Data from Henke [Henke 1993] *et al.* and Hubbel *et al.* [Hubbell 1980]. [reprinted from [Kirz 1995]].

a few keV and is therefore ignored in the following discussion. We can also see that multiple scattering can be neglected for energies below 10 keV, since the cross section for absorption is much larger than the cross section for elastic scattering.

Following Jackson [Jackson 1975], we can write the elastic scattering cross section, also called the Thomson cross section, for an unpolarized electromagnetic wave incident on a free electron as

$$\frac{d\sigma_{\text{coh}}}{d\Omega} = r_e^2 \cdot \frac{1}{2}(1 + \cos^2 \Theta). \tag{1.20}$$

Integrating gives the total cross section

$$\sigma_{\text{coh}} = \frac{8\pi}{3} r_e^2. \tag{1.21}$$

Now, if we are dealing with an atom instead of a single electron, where the electrons are spaced closer together than the wavelength of the incident radiation, the scattering amplitudes from the individual electrons will add up coherently. Therefore Eq. (1.21) becomes

$$\sigma_{\text{coh}} = \frac{8\pi}{3} r_e^2 |f_1 + i f_2|^2. \tag{1.22}$$

1.2 X-ray sources

X-ray sources have come a long way from the time when X rays were discovered by Röntgen in 1895 to the current sources available today. **X-ray tubes** were the first sources that produced X rays and they still find usage as sources for medical imaging. They operate by shooting an electron beam into a metal target. The emitted radiation consists of 'Bremsstrahlung' (electrons are decelerated in the metal target and emit radiation) and characteristic radiation (electrons eject an inner shell electron which is then replaced by an outer shell electron thus producing the characteristic radiation). In the 1940's, synchrotron radiation was discovered at the General Electric laboratory in Schenectady, New York. Synchrotron radiation is emitted when charged particles are deflected by magnetic fields. The first experiments with synchrotron radiation were done in a parasitical way at synchrotrons built for particle physics research. These X-ray sources are also called **first generation sources**. At the beginning of the 1980's **second generation sources** started operation at Brookhaven (NSLS), Daresbury (SRS), Berlin (BESSY) and other locations. The sources were specifically built for using synchrotron radiation, by offering

a large number of experimenters access to the intense radiation. A major step forward in generating radiation at synchrotrons came with the introduction of insertion devices, such as the undulator. A schematic diagram of an undulator together with an electron beam is shown in Figure 1.3. Here, the electron

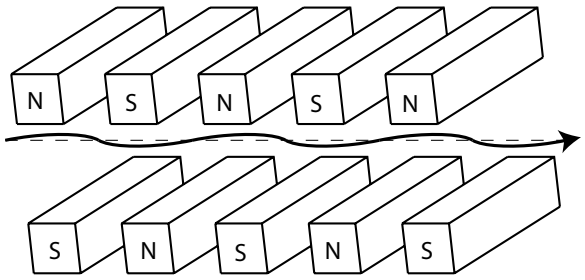

Figure 1.3: Schematic of an undulator: the electron beam is deflected by an alternating magnet structure, producing a narrow radiation cone and improved monochromaticity.

beam is deflected by the periodic magnet structure of the undulator, resulting in a narrow radiation cone and improved monochromaticity ($\Delta\lambda/\lambda = 1/N$, where N is the number of magnet periods). The spectral brightness is of great importance for experiments discussed in this thesis (see Section 2.2, and 2.3). It is defined as

$$B = \frac{\text{photon flux}}{\text{source area} \cdot \text{solid angle} \cdot 0.1\%\text{bandwidth}}. \tag{1.23}$$

With the need for more and more insertion devices, **third generation sources**, built with many straight sections to implement insertion devices and very low electron beam emittance, started up operations in Grenoble (ESRF), Argonne (APS), Berkeley (ALS), and many others labs. Older second generation sources such as the NSLS were also upgraded with insertion devices wherever possible. Figure 1.4 shows the brightness as a function of energy for a number of available X-ray sources. The success of synchrotron research has sparked new construction of sources around the world, so that there are about 50 synchrotron sources currently operating worldwide. The **fourth generation sources**, currently under development in Hamburg (TTF-FEL) and Stanford

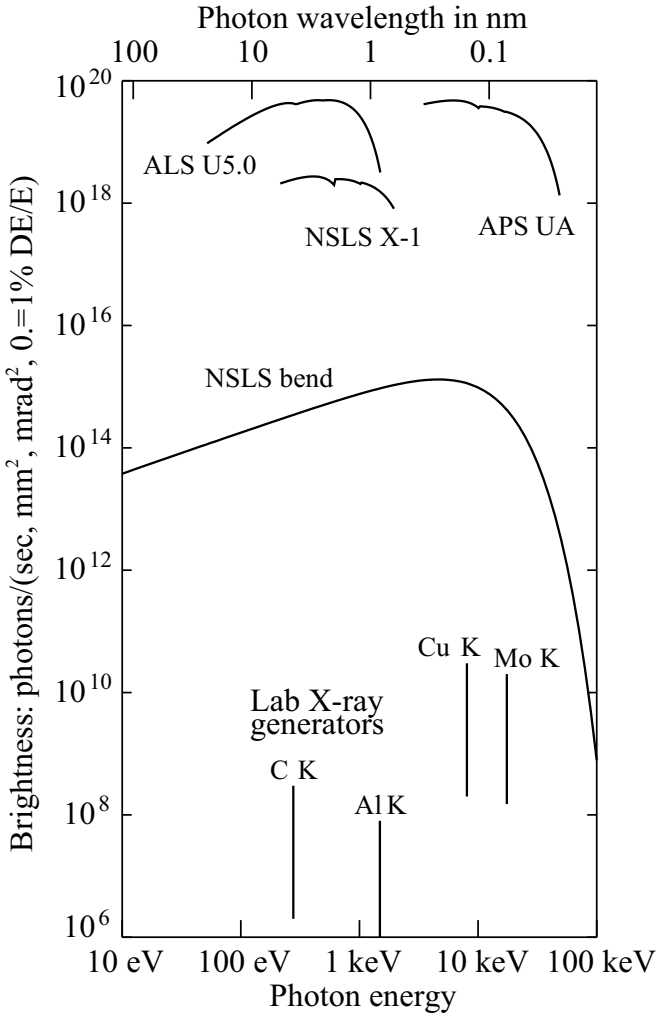

Figure 1.4: Comparison of the brightness as a function of energy for a number of available X-ray sources.

(LCLS), will be drastically different from todays sources. Those new sources, which are called free-electron lasers (FEL's), use a linear electron accelerator (LINAC) and a long undulator ($\sim$ 100 m) to amplify the radiation in a single pass and reach orders of magnitude higher 'peak' brightness than current third generation sources. They also offer very short time duration, coherent X-ray radiation. Another development is the energy recovering linac (ERL). Here, a LINAC accelerates an electron bunch, which is then injected into a storage ring for just one pass, before the energy of the electron bunch is recovered in order to accelerate a new electron bunch. Whereas the ERL does not reach the peak brightness of an FEL, it can provide a much higher average brightness, comparable to current third-generation sources. Because FEL's and ERL's are single-pass devices, the electron dynamics is much different from storage rings. This results in round electron bunches rather than cigar-shaped electron bunches for the storage rings, offering much shorter radiation pulses.

Because of the high brightness of undulator radiation beamlines, they are the ideal sources for the experiments described in this dissertation.

1.3 Lenses for X rays - zone plates

Zone plates have been the most successful lenses for focusing soft X rays. State-of-the-art zone plates can provide high resolution and high focusing efficiencies. They are circular diffraction gratings consisting of alternating opaque and transparent zones (Figure 1.5). The line width decreases with the radius.

According to Wood [Wood 1934], the first zone plate was produced in 1871 by Lord Rayleigh but his results were not published. They were first mentioned in the literature by Soret [Soret 1875]. In the 50's and 60's Baez and colleagues looked into the idea of using zone plates to do X-ray microscopy [Baez 1950, Baez 1960, Baez 1961]. In 1972, Sayre proposed to use electron beam microfabrication techniques to produce zone plates for focusing X-rays [Sayre 1972]. Zone plates were successfully used in the Transmission X-ray Microscope (TXM) developed at Göttingen [Schmahl 1974, Niemann 1983, Niemann 1994] and the Stony Brook Scanning Transmission X-ray Microscope (STXM) [Kirz 1980, Rarback 1988, Feser 2000] with more microscopes operating at other synchrotron and lab based sources.

In the following we will briefly summarize important properties of zone plates, which find use in the remainder of this thesis. For a detailed derivation of the formulae, the reader is referred to the literature when necessary.

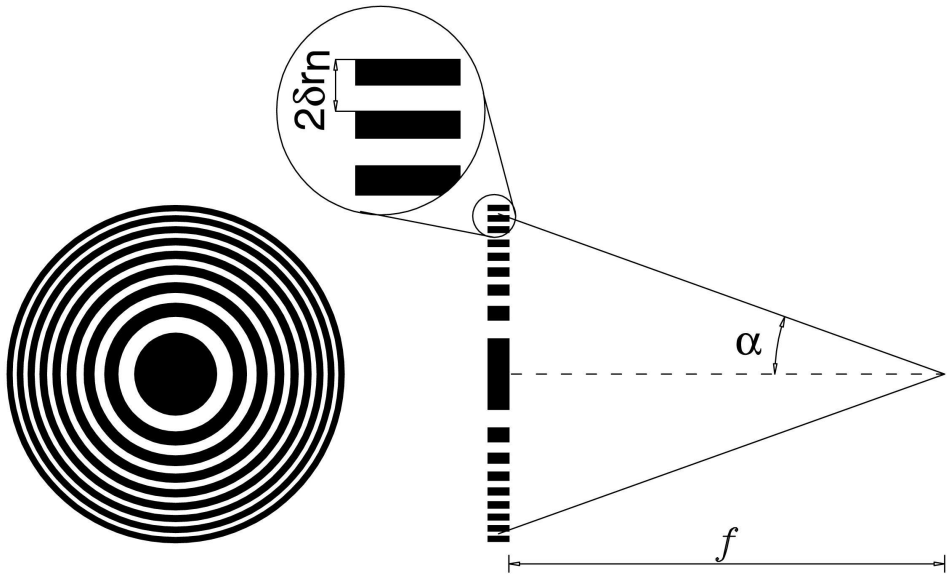

Figure 1.5: Schematic of a zone plate. Alternating opaque and transparent rings diffract incident radiation to form a focus spot.

1.3.1 Zone plate properties

The zones of a zone plate have to be arranged so that the path difference between two adjacent zones is one wavelength. It follows then for the radius of the n-th zone r_n

$$r_n^2 = mn\lambda f + m^2 n^2 \frac{\lambda^2}{4}, \tag{1.24}$$

where m is the m-th diffraction order and f is the focal length of the zone plate. The second term is for spherical aberration and can usually be neglected. Another relationship involving the diameter $2r_N$ and the outermost zone width δ_{rN} is given by

$$2r_N\delta_{r_N} = m\lambda f. \tag{1.25}$$

Solving this equation for r_N, we can substitute the result into Eq. (1.24) and solve for the number of zones in a zone plate:

$$N = \frac{m\lambda f}{4{\delta_{r_N}}^2}. \tag{1.26}$$

1.3.2 Transverse resolution

Zone plates can be treated as normal thin lenses, when the number of zones is more than 100 [Michette 1986]. The diffraction-limited **transverse resolution** is then given by the Rayleigh criterion for a circular aperture as

$$\begin{aligned} \delta_t &= 0.61\frac{\lambda}{N.A.} && (1.27)\\ &= 1.22\delta_{r_N}, && (1.28) \end{aligned}$$

since the numerical aperture is $N.A. = \frac{\lambda}{2\delta_{r_N}}$.

1.3.3 Longitudinal resolution or Depth of focus

In addition to the transverse resolution, we must also consider the **longitudinal resolution** or **depth of focus** (DOF). Using again the Rayleigh resolution criterium, we get

$$\begin{aligned} \delta_l &= 1.22\frac{\lambda}{(N.A.)^2}\\ &= 4.88\frac{{\delta_{r_N}}^2}{\lambda}. && (1.29) \end{aligned}$$

As an example we take $\lambda = 2.34$ nm which corresponds to an energy of 530 eV and $\delta_{r_N} = 20$ nm and get a depth of focus of $\delta_l = \pm 0.83\mu$m.

1.4 X-ray microscopy

Submicron resolution soft X-ray microscopy was pioneered in the mid 70s mainly by the Stony Brook group and by the Göttingen group. The Stony Brook group focused on the development of Scanning Transmission X-ray Microscopes (STXM's), whereas the Göttingen group focused on Transmission X-ray Microscopes (TXM's). Figure 1.6 shows a schematic diagram of both microscope types. In a TXM the X-ray source is imaged onto the specimen by a condensor zone plate, which is wobbled to provide an even illumination on the sample [Niemann 1992]. A high resolution zone plate behind the specimen images the sample onto a 2D pixel detector. The phase space (phase space = source size · solid angle) that can be used in a TXM is large compared to the phase space for STXM's. A bending magnet source is therefore well matched to the TXM. An image can be acquired within a few seconds, which makes the

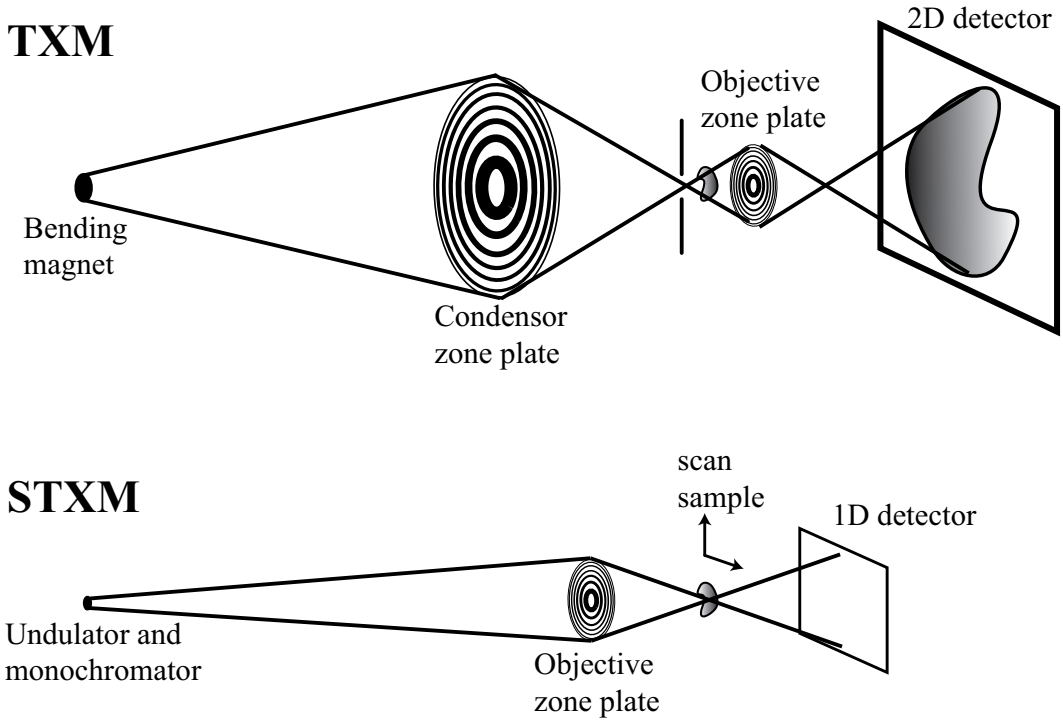

Figure 1.6: Comparison of TXM and STXM. In a TXM, a condensor zone plate focuses the X rays onto the specimen. A high resolution zone plate after the specimen images the specimen onto a detector. In a STXM, the X rays are focused onto the specimen, which is then scanned through the focused beam. The transmitted X rays are detected by a detector for each sample position.

TXM well suited for tomography, where images of a specimen are collected at several rotation angles to yield a 3D reconstruction of the object [Weiß 2000].

In STXMs, X rays are focused by a high resolution zone plate onto the specimen which is then scanned through the focal spot. A detector behind the specimen measures the transmitted intensity at each pixel, to give a 2D image of the object. To achieve a diffraction limited focus spot, the phase space accepted by the zone plate has to be smaller than λ^2 [Buckley 1988, Jacobsen 1992, Winn 2000a]. Undulator sources provide a high flux in a small phase space and are therefore well suited for STXMs. To achieve the diffraction limited focus spot, one also needs to illuminate the zone plate coherently, which can be achieved by using a slit in front of the zone plate. A monochromator is used to provide the necessary spectral resolution [Rarback 1990b, Winn 2000a]. The spectral resolution achieved by a monochromator is dependent on the size of the incident beam. By limiting the extent of the beam, a narrow spectral bandwidth can be obtained. There is a trade-off between narrow spectral bandwidth and photon flux. Fortunately, due to the small phase space of the undulator radiation, there are still enough photons left for imaging even at spectral bandwidth of $\lambda/\Delta\lambda = 3000$ [Winn 2000a]. The STXM is therefore well suited for X-ray absorption near-edge spectroscopy (XANES) to study the chemical compositions of samples (see Section 5.4 for more details). Microspectroscopy, the combination of imaging and spectroscopy, makes STXMs powerful in studying the chemical composition of samples at high resolution [Jacobsen 2000]. Considering radiation damage to the specimen, STXMs have the advantage that the low efficient optic is before the specimen rather than behind as is the case for TXMs. The image acquisition time for high resolution imaging is around a few minutes at the NSLS. Tomography has been demonstrated with a STXM [Wang 2000, Winn 2000b] but present NSLS STXMs cannot really compete with the rapid data collection possible with the TXMs.

Our group operates three STXMs at the National Synchrotron Light Source (NSLS) (see Section 2.2 for more details). Two of them have the specimen at room temperature [Feser 2000], while one keeps the specimen cooled to liquid nitrogen temperature (cryo-STXM) to protect the specimen against damaging radiation (see also Chapter 5) [Maser 2000]. The optics of the microscopes are identical: the zone plate focuses the X rays onto the sample. A central stop on the zone plate and an order-sorting aperture (OSA) prevent all orders, except for the first order, from reaching the specimen. Figure 1.7 shows a schematic diagram of the zone plate together with the OSA. The cryo-STXM (see Figure 1.8 for a schematic diagram of the instrument) was used for the radiation damage studies in PMMA, described in Chapter 5.

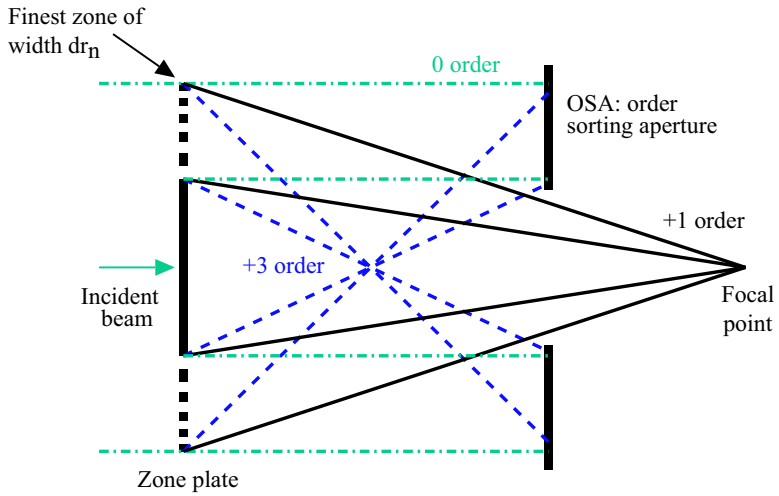

Figure 1.7: The zone plate focuses the X rays onto the specimen. A central stop on the zone plate and an order-sorting aperture prevent all orders, except for the first order, from reaching the specimen. [reprinted from [Kirz 1995]]

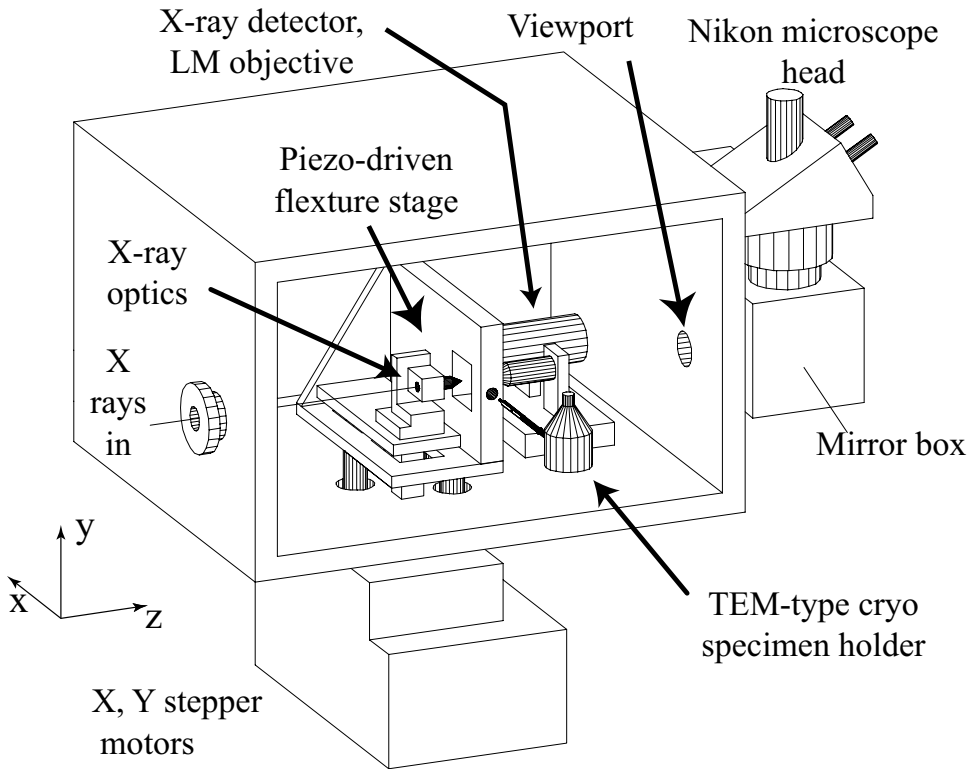

Figure 1.8: Schematic of the cryo-STXM. The X-ray beam enters the vacuum chamber and is incident on the zone plate and OSA assembly. The specimen is inserted into the chamber on a cryo-cooled sample transfer holder, which rests in the piezo stage. The piezo stage is used to scan the sample through the X-ray focus and the transmitted radiation is recorded using a photomultiplier tube. The optical elements and the sample piezo stage are mounted onto stepper motors. A telescope can be used to align the microscope components. [reprinted from [Wang 1998]]

Chapter 2

Experimental setup

This chapter describes the experimental apparatus which was developed to do high-resolution 3D imaging. Experiments were done at beamline X1A at the National Synchrotron Light Source (NSLS) and beamline 9.0.1 at the Advanced Light Source (ALS). Therefore this chapter discusses the details of both beamlines.

2.1 Experimental chamber

In order to obtain high resolution 3D images one has to collect several hundred views of the specimen, since there is only limited depth resolution on each view (for more details refer to Section 3.1.8). To make this feasible, it is necessary to automate the data collection process. In addition, one has to protect the sample against radiation damage from the incident X rays.

The chamber used for the experiments in this dissertation was designed to meet the following requirements:

- cryogenic sample temperatures to protect specimens against radiation damage
- high tilt system to minimize missing data for 3D data sets
- motorized stages to rapidly and automatically position optics and beam defining apertures
- flexible setup to accommodate different beamlines and different experiments
- graphical user interface (GUI) to give the microscope user an easy and intuitive way to acquire data
- automation of data collection

Since there are no commercial chambers available that would meet all our requirements, we started designing and constructing one for our experiments. Development of the chamber used for our experiments was a team effort, led by Chris Jacobsen and Janos Kirz with support from Chi-Chang Kao's group at Brookhaven. Important contributions included these by David Shapiro on the design of several mechanical assemblies and on the vacuum interlock system; Onur Mentes on mounting and programming of the CCD camera; Enju Lima on client-server programming; and Cecilia Sanchez-Hanke on the design of the cold trap, helping make the development a success. Many additional people helped at various stages of installation and debugging of the chamber at the NSLS and ALS. Figure 2.1 shows the schematic diagram of the main elements inside the constructed experimental chamber. The pinhole is located on the so-called 'upstream motor stack' (see Section 2.1.2). The sample is translated

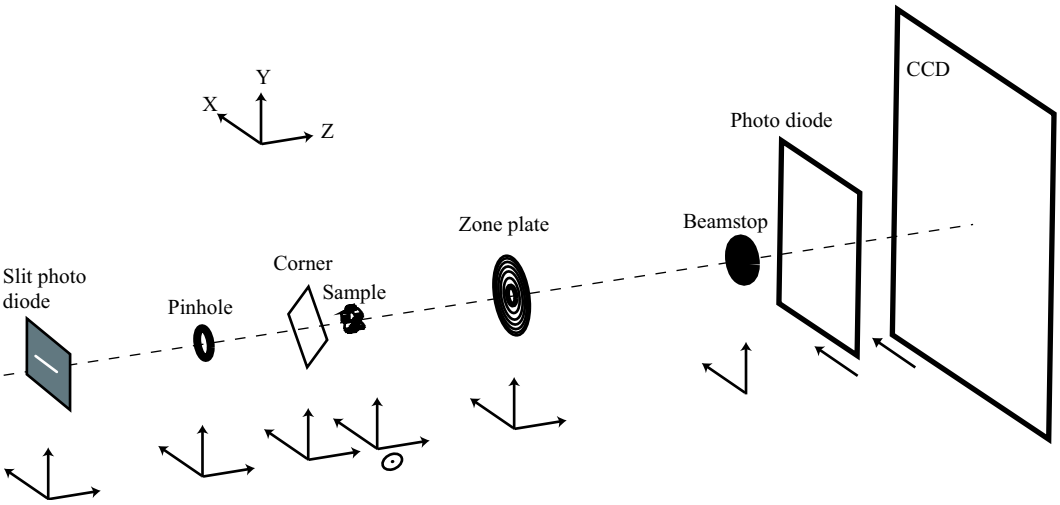

Figure 2.1: Schematic of the elements used inside the vacuum chamber. The direction of motion is indicated by arrows. Sample rotation is done around the X-axis.

in XYZ[1] and rotated around the X-axis by the goniometer (see Section 2.1.1). A downstream motor stack holds a corner to block out scattering from the upstream pinhole when diffraction patterns are collected (see Section 4.4.2). It also holds a zone plate for imaging the sample. The optical elements can also be moved in XYZ. A beamstop on an XY setup is used to block the straight beam from reaching the CCD. A photodiode can be inserted to measure flux while aligning the various elements.

2.1.1 Goniometer and sample holder

Sample positioning is done with a commercially available motorized three-axis goniometer system by JEOL USA, Inc. The system is part of their JEM-2010 FasTEM, a transmission electron microscope. We were happy enough to just receive the goniometer system without ordering the rest of the rather expensive microscope! All of the goniometer motor control is outside the

[1]In the right-handed coordinate system used the beam travels along the Z-axis as indicated in the Figure 2.1. The positive Y-axis is vertical up and the positive X-axis is horizontal to the right, when looking into the beam.

vacuum and the sample is inserted into the vacuum chamber via an airlock. Figure 2.2 shows the goniometer attached to the vacuum chamber together with a view of the goniometer from inside the vacuum chamber. Vacuum fittings were designed to attach the goniometer drives to the chamber.

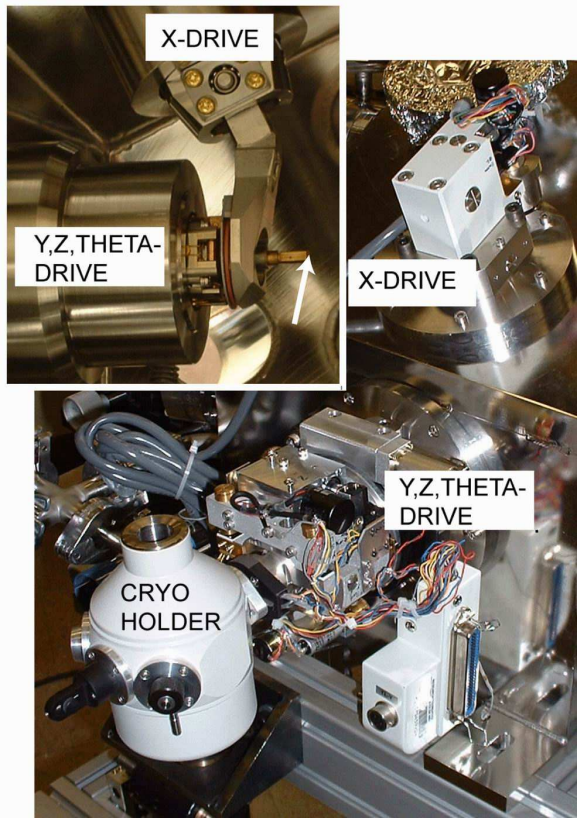

Figure 2.2: View of the goniometer system purchased from JEOL USA, Inc. The inset shows the goniometer inside the vacuum chamber. The sample position is indicated by the arrow.

A schematic diagram of the goniometer together with a sample transfer holder is shown in Figure 2.3. The main goniometer drive sits horizontally and provides motion in YZ and Θ. The horizontal drive is mounted to the chamber at a 25^o angle and provides motion along the X-axis by pushing the sample

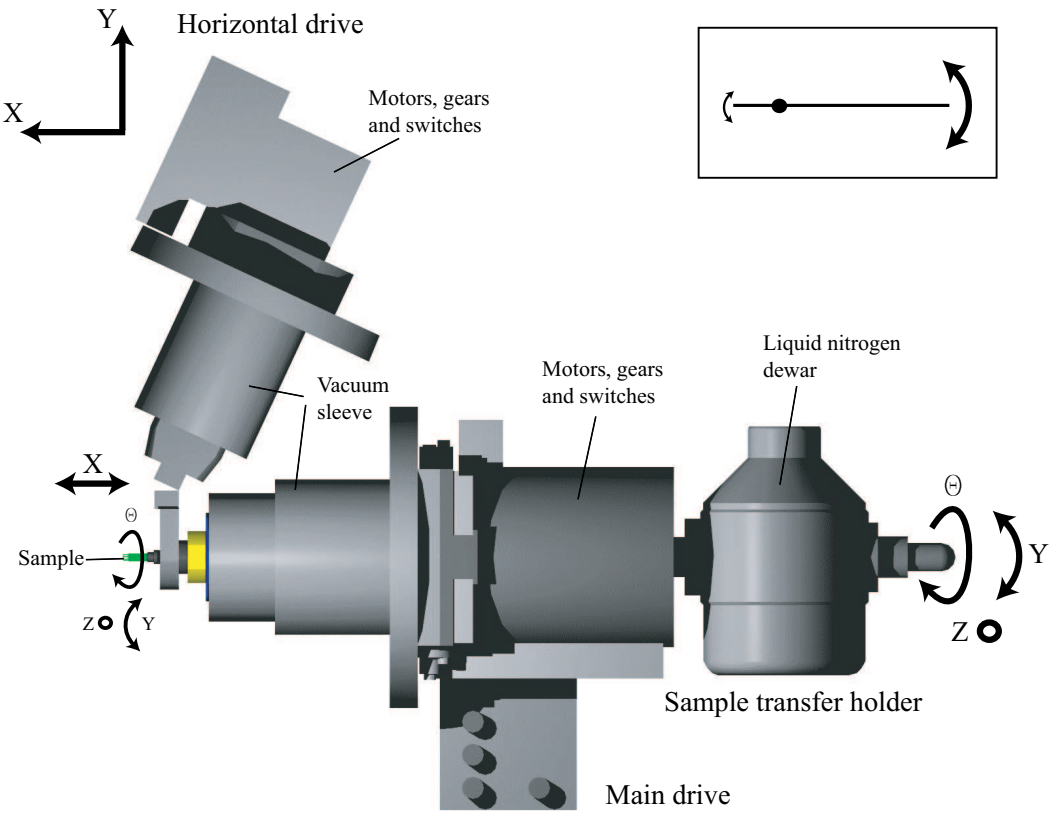

Figure 2.3: Schematic of the JEOL goniometer system together with vacuum fittings and a cryo sample transfer holder. All motors, encoders, gears and switches are outside the vacuum. The horizontal drive provides motion along the X-axis. The main drive provide motion along the Y- and Z-axis and rotation around the X-axis. The YZ motion on the outside of the goniometer is demagnified at the sample position, since the sample transfer holder is pivoted around a position inside the vacuum sleeve (see also small inset).

transfer holder in and out against the vacuum force. Whereas this motion is truly along the X-axis, the Y and Z motions are describing a motion along an arc as indicated in the figure. The small inset in Figure 2.3 shows the scheme behind this: a large motion at the outside of the chamber moves a rod up and down. The rod is pivoted around a ball end, therefore demagnifying the motion on the shorter end of the rod, corresponding to the sample position. In the goniometer, this ball end is located inside the vacuum sleeve. The sphere is equipped with several holes that provide pumping connections when the airlock is pumped out to insert a sample transfer holder. A close-up of this region is shown in Figure 2.4. The goniometer sphere, which is the pivot

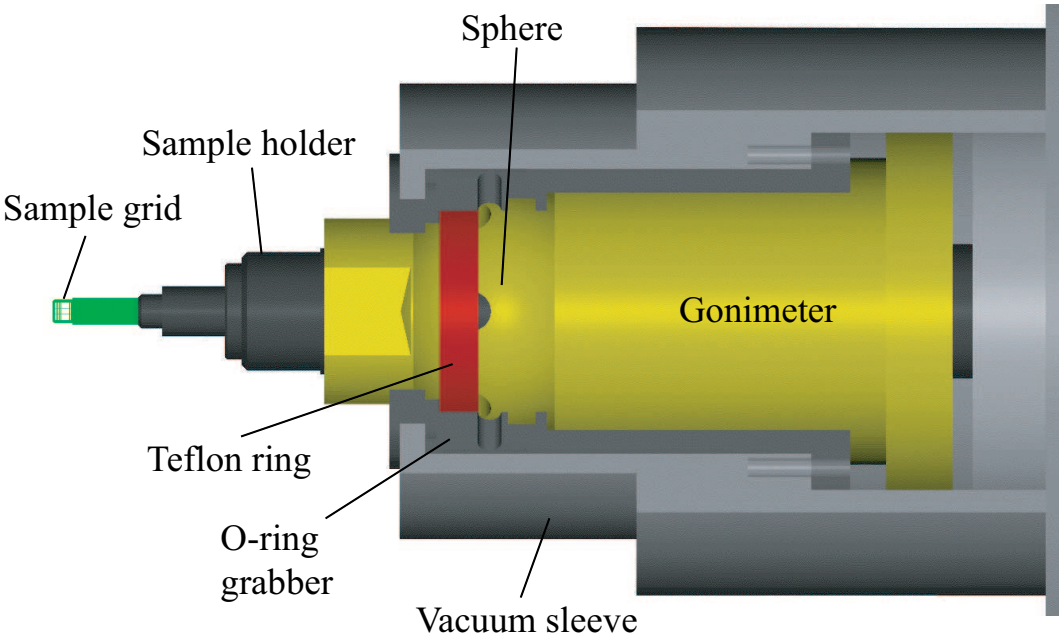

Figure 2.4: Schematic of the JEOL main drive together with vacuum fittings, sample holder and sample grid. Part of the vacuum fittings are cut away so that the inside of the goniometer becomes visible. The goniometer sphere, which is the pivot point, rests against a Teflon ring providing smooth movement of the sphere when rotated. The 'O-ring grabber' is a metal piece which is in between the vacuum sleeve and the goniometer sphere. It has several O-rings for airlock pumping connections and vacuum separation between the chamber vacuum and the outside.

point, rests against a Teflon ring providing smooth movement of the sphere when rotated. The 'O-ring grabber' is a metal piece which is in between the vacuum sleeve and the goniometer sphere. It has several O-rings for airlock pumping connections and vacuum separation between the chamber vacuum and the outside. All goniometer motors are DC-motors with encoder feedback to accurately position the sample.

The sample can be inserted on a sample holder through the goniometer airlock. We have two sample holders that fit the goniometer system. One is a Gatan 630 high-tilt cryo specimen holder on which the sample can be cooled to liquid nitrogen temperature to minimize radiation damage during data acquisition (see Figure 2.5). Cryo holders normally use round copper grids which are supported by a rather bulky copper frame for good thermal contact to the liquid nitrogen reservoir. Such a holder makes it difficult to go to large tilt angles. Our Gatan holder is equipped with almost free-standing slotted copper specimen grids that allow for an angular tilt range of $\pm 80°$. The grid can be retracted between two copper faces, so that cryo specimens are protected when transferred into the chamber.

The second sample holder is a JEOL room-temperature holder (see 2.6) which is cheaper and more robust than the Gatan holder and can be used for samples that do not require cooling.

2.1.2 Motor stages and drive electronics

To quickly align various optical components like zone plates, beam defining apertures or phosphor screens, the new experimental chamber makes use of two in-vacuum XYZ motorized translation stages with sub-micron precision.

The stages were manufactured by National Aperture and are driven by in-vacuum DC motors with encoder feedback. One of the motor stacks is positioned upstream of the sample, the other downstream of the sample. The optics mounts are designed to hold several optical components to give great flexibility to change components without breaking the vacuum. All stages can be moved and scanned using the custom control and data acquisition software described in Section 2.1.5.

All stages and the goniometer motors are controlled by two Galil motion controllers with ethernet interfaces on a private network. In collaboration with Chuck Pancake of the Stony Brook electronics shop, we developed a custom amplifier that provides the necessary current to drive the motors (commercial motor drivers exist, but the number required would have been expensive, bulky, and would have required awkward cabling.). A detailed description of the custom amplifier can be found in Appendix B. Using custom control software

Figure 2.5: View of the Gatan cryo sample holder. The dewar can be filled with liquid nitrogen to cool the sample. The small image shows a close-up of the tip of the holder, where a high-tilt copper grid is inserted. The grid can be retracted between two copper plates to protect cryo specimens during transfer into the vacuum chamber.

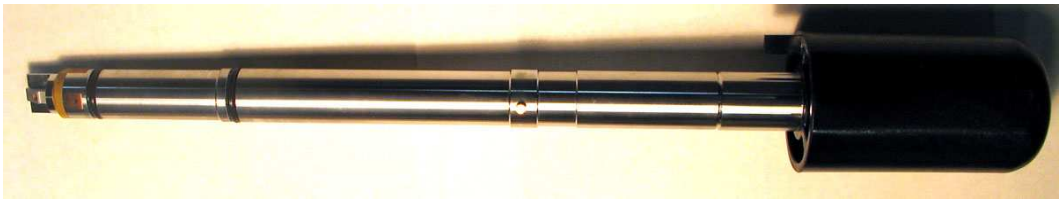

Figure 2.6: JEOL room-temperature sample holder.

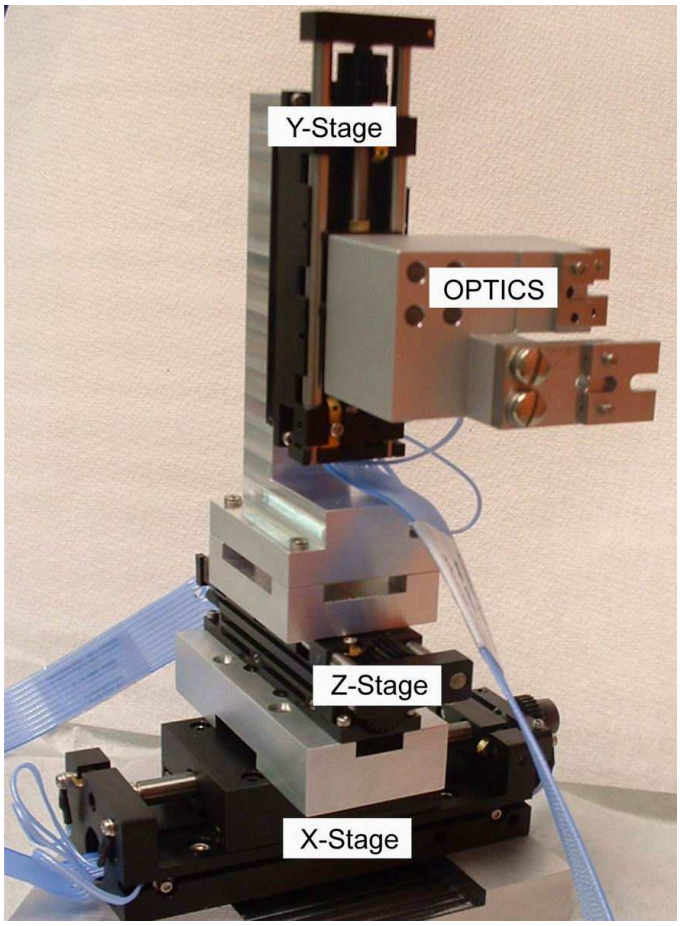

Figure 2.7: Two motorized XYZ stacks hold optics and beam defining apertures that can be positioned around the sample.

we are able to move or scan all motors and collect CCD images (see also Section 2.1.5).

During the initial evaluation of a loaner stage, the stage appeared to be rigid enough for our needs and we therefore ordered them for our system. It turned out that the stages are not rigid at all when mounted as an XYZ setup. Subsequent tuning of the stacks by National Aperture barely improved the situation. During the first holography experiments, we even added several springs to make the stages less prone to vibrations. However, the achieved stability was not satisfactory for the holography experiment (see Chapter 3), which are very sensitive to vibrations. The diffraction experiment (see Chapter 4) is much less sensitive to vibrations and works well with the current setup. Note, that for in-line holography, a certain shift between the specimen and the imaging zone plate results in a shifted hologram and therefore the fringes are washed out. For diffraction imaging, the shifted object will have the same diffraction pattern as the original object and an additional constant phase factor (see Appendix D Eq. D.3), which has no influence on the recorded intensity of the diffraction pattern. This is of course only true if the shift does not result in a changed illumination of the object. In the diffraction experiments presented in this thesis, we made sure that the illumination is constant over an area significantly larger than the object (see Eq. (4.18) for more details).

2.1.3 Detector system

The detector is a completely in-vacuum backside illuminated CCD camera from Roper Scientific (MTE-2 camera with EEV chip, 1340x1300 pixels with 20 micron pixel size). Modern, cooled CCD cameras make long exposure times possible. Thermoelectric cooling also allows for rapid camera warm-up time in case the chamber needs to be vented to atmospheric pressure. Measurements of the dark noise at -45^oC were made by David Shapiro and were about 95 $\pm$ 8 counts for exposure times ranging from 10 ms to 100 s [Shapiro 2004]. In addition to the measured noise of $\pm$ 8 counts, we have to consider shot noise, which is directly proportional to the square root of the number of incident photons. The total expected noise can then be written as

$$N_{\text{noise}} = \sqrt{N_{\text{shot}}^2 + N_{\text{CCD}}} \tag{2.1}$$

$$= \sqrt{\sqrt{N}^2 + \sigma^2}, \tag{2.2}$$

where $\sigma = \pm 8$ counts. Adapting the Rose criterium [Rose 1948], we require a signal to noise ratio of 5:1 in order to distinguish the signal from the noise.

We write

$$\begin{aligned} \mathrm{SNR} = 5 &= \frac{N}{N_{\mathrm{noise}}} \\ &= \frac{N}{\sqrt{\sqrt{N}^2 + \sigma^2}}, \end{aligned} \tag{2.3}$$

where N is now the minimum detectible signal. Inserting $\sigma = \pm 8$ counts and solving the quadratic equation, gives 54 counts for the minimum detectable signal. An incident 750 eV photon already generates 750 eV/3.63 counts/eV = 207 counts, which is much more than the minimum detectable signal. In fact, the shot noise for the single photon is about 14 counts.

The detector system can be translated parallel to the beam axis inside the chamber over a distance of 17 cm. The translation stage is already equipped with a stepping motor, but has not been implemented in the software and a motor amplifier for stepping motors has to be purchased. The CCD's position closest to the specimen, 10 cm, allows for recording high resolution diffraction data and its furthest position from the specimen, 1 m with the insertion of an extension tube, allows for high magnification zone plate imaging in diffraction tomography. A motorized stage underneath the camera makes it possible to translate the camera transverse to the beam by 5 cm to record off-axis zone plate images or higher resolution diffraction data. Unfortunately, the stage frequently got stuck when moving, since the hoses from the CCD water cooling were putting some sideways forces on the carriage that holds the CCD. Therefore the stage is currently disabled until a better way of supporting the CCD is found. A motorized in-vacuum stage in front of the CCD camera carries a photo diode for alignment purposes (see Figure 2.8). This photo diode can be used to measure the photon flux. The quantum efficiency of the photodiode is essentially the photon energy divided by the electron-hole pair creation energy (about 3.63 eV). That means that the number of photons per second n_{Photons} is given by

$$n_{\mathrm{Photons}} = \frac{3.63 \text{ eV}}{E} \cdot \frac{I}{q}. \tag{2.4}$$

Here E is the photon energy in electron volts, I is the measured current in Amperes and $q = 1.6 \cdot 10^{-19}$ C is the charge of the electron in Coulombs. A choice of beamstops to block out the direct x-ray beam can be mounted on an XY motor stack.

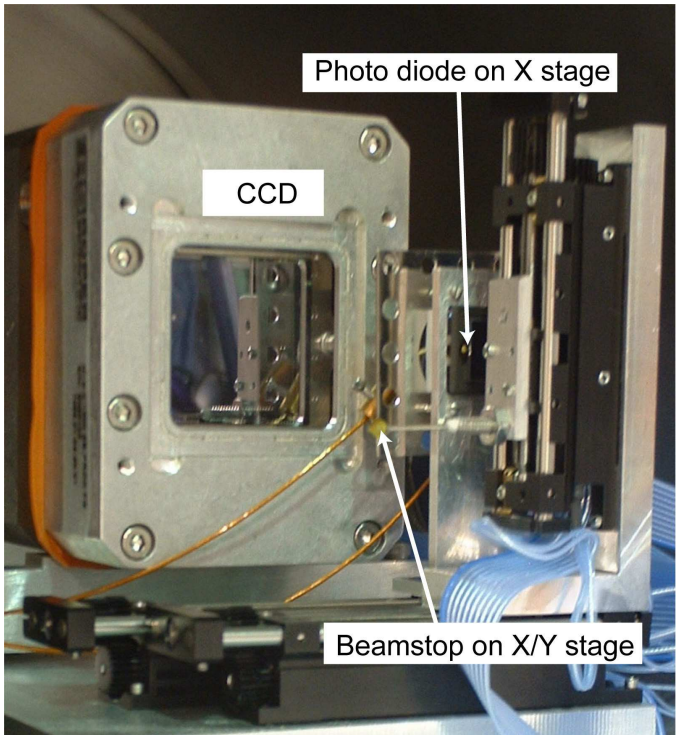

Figure 2.8: CCD camera with beamstop and photodiode stages. The beamstop can be moved along the X- and Y-axis, while the photodiode and CCD may be moved along the X-axis. The entire unit is mounted on a platform which can be translated from outside along the Z-axis.

2.1.4 Vacuum system

The chamber is pumped down by a 60 liter Pfeiffer turbo pump, backed by a Varian scroll pump. At low pressure, an ion pump can be used instead to further improve the vacuum and to minimize vibrations due to the turbo pump. However, because of some vacuum problems with the ion pump, which are probably due to the flexible bellows between the pump and the chamber, the pump is currently not mounted. The airlock is pumped by a small Varian scroll pump. A cold-cathode gauge and a convectron gauge measure the vacuum and are used for a custom-built vacuum interlock built by David Shapiro and Barrett Clay of the NSLS. Valves and pumps are controlled using a touch-screen connected to the vacuum interlock.

2.1.5 Control software

The Galil motor controllers and the Roper CCD controller are controlled by a 750 MHz Dell workstation running RedHat Linux. We developed software written in C++ that handles communication with each of the devices and provides functions (i.e., 'move motor to micron position', 'do XY scan', 'acquire image', etc.) that can be used by other C++ programs. The software is built on the Roper-supplied CCD driver and Galil-supplied ethernet subroutines. To make the operation intuitive to a user, we further developed a graphical user interface (GUI) written in IDL. Using IDL for the GUI also has the advantage that IDL provides an extensive library for image manipulation which is essential for data analysis. As an alternative to the GUI, the user can also choose the dt_script routine which reads commands from a previously generated text file. This operation is very useful for automatic data collection since several commands to move motors or acquire images can be listed in the text file and then executed by the dt_script routine without further user interaction.

To combine the virtues of having IDL as a GUI and the underlying device communication in C++, we adopted a client-server scheme which is illustrated in Figure 2.9.

If the user would, for example, want to move a motor, he would click a button in dt_gui. This button then evokes a function in dt_client which generates the command that contains the motor name and the new desired position. The generated command is sent over a TCP/IP port to the server, where it is processed by dt_services. Next, dt_services sends instructions to the galil_mot class, which then executes the command on the Galil motor controller. After the completion of the command on the Galil controller, feedback about success

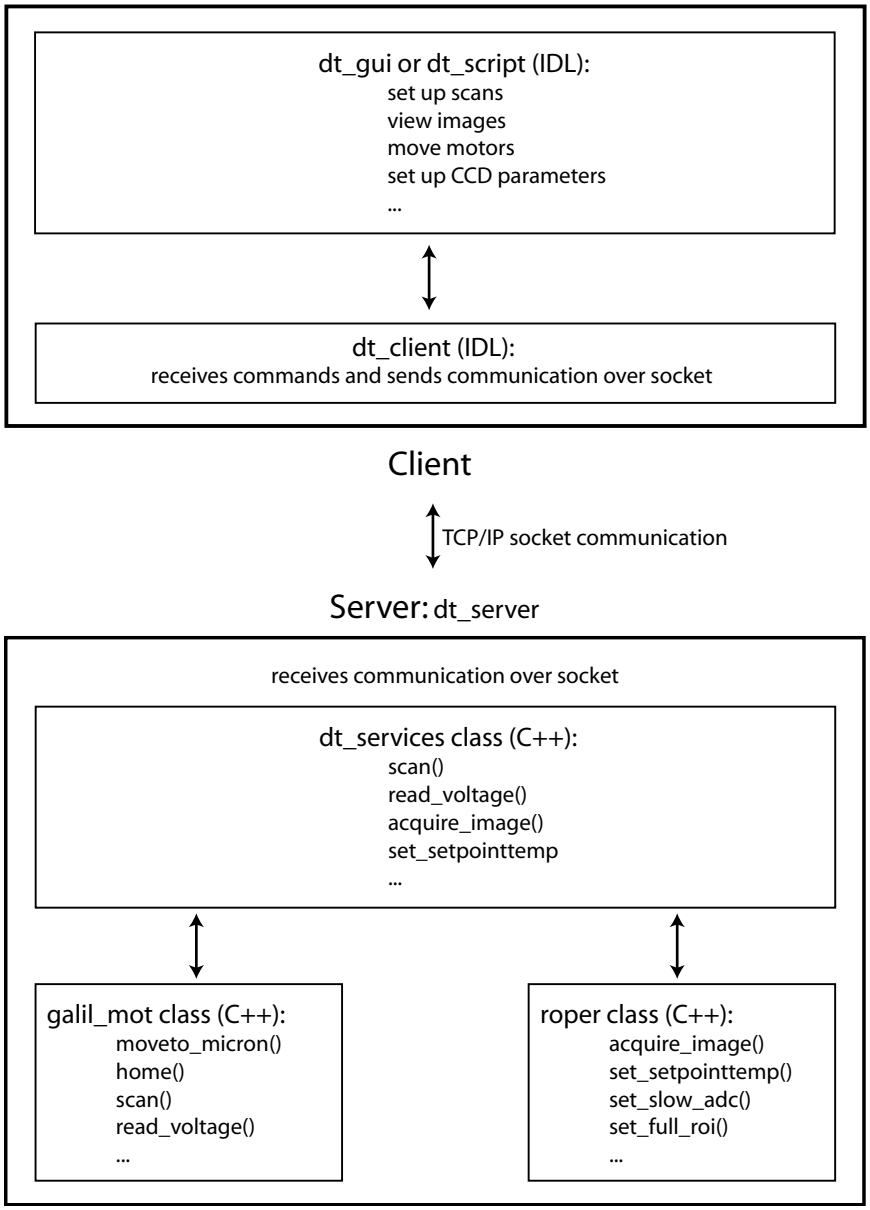

Figure 2.9: Structure of the control software showing the graphical user interface or scripting interface on the client side and the device communication software on the server side.

or failure of the command is sent back to user interface via the reverse order.

The client and server could in principal be on different computers which are connected over the network. This is the virtue of having all device communication separated from the user computer and therefore being less sensitive to tasks which are run on the client side. The client-server scheme will also be used in the software which is under development for a new generation Scanning Transmission X-ray Microscope at the NSLS.

Figure 2.10 shows a screenshot of the main GUI including the image display and manipulation widget, whereas Figure 2.11 shows a screenshot of the available control widgets for the CCD and motors.

2.1.6 Chamber and support system

We designed the chamber to fit the JEOL goniometer, the Roper CCD, motor stages, etc and had it manufactured by Norcal, Inc. The chamber has a number of viewports through which the X-ray beam can be seen on phosphor screens. An access door provides an easy way of reaching into the chamber to switch optical components on the stages, making adjustments straightforward so that downtime is minimized.

The whole experimental chamber is mounted on a moveable frame, equipped with actuators that allow precise positioning of the experimental chamber in all directions including tilt. This was necessary since the chamber was used at different beamlines during the initial operations and we needed to minimize the setup time between the experiments.

The frame is also equipped with a linear slider underneath the CCD section which allows the CCD section to slide back in order to insert an extension tube needed for holography experiments where a high magnification is required.

2.2 National Synchrotron Light Source beamline X1-A

The X1-A beamline at the National Synchrotron Light Source (NSLS) at Brookhaven National Laboratory (BNL) is an undulator beamline providing soft X rays for experiments requiring spatial and temporal coherence. The undulator serving the endstations of the X1-A beamline is located in a low-β section of the storage ring, where the electron beam size is small, but has a large divergence [Rarback 1990a].

The current X1-A beamline and undulator are designed to deliver coherent X rays in the energy range from 250 to 800 eV [Winn 2000a]. Figure 2.12 shows

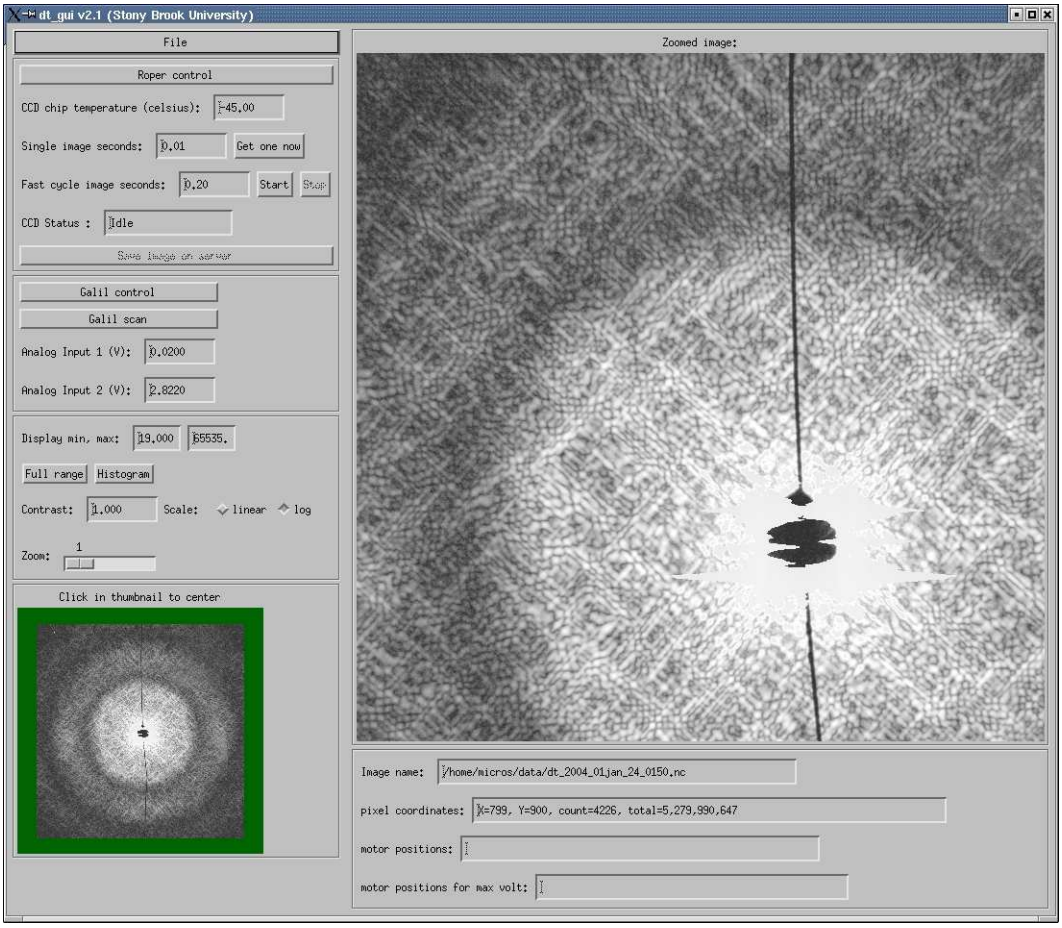

Figure 2.10: Graphical User Interface to acquire, display, and manipulate the CCD and scan images.

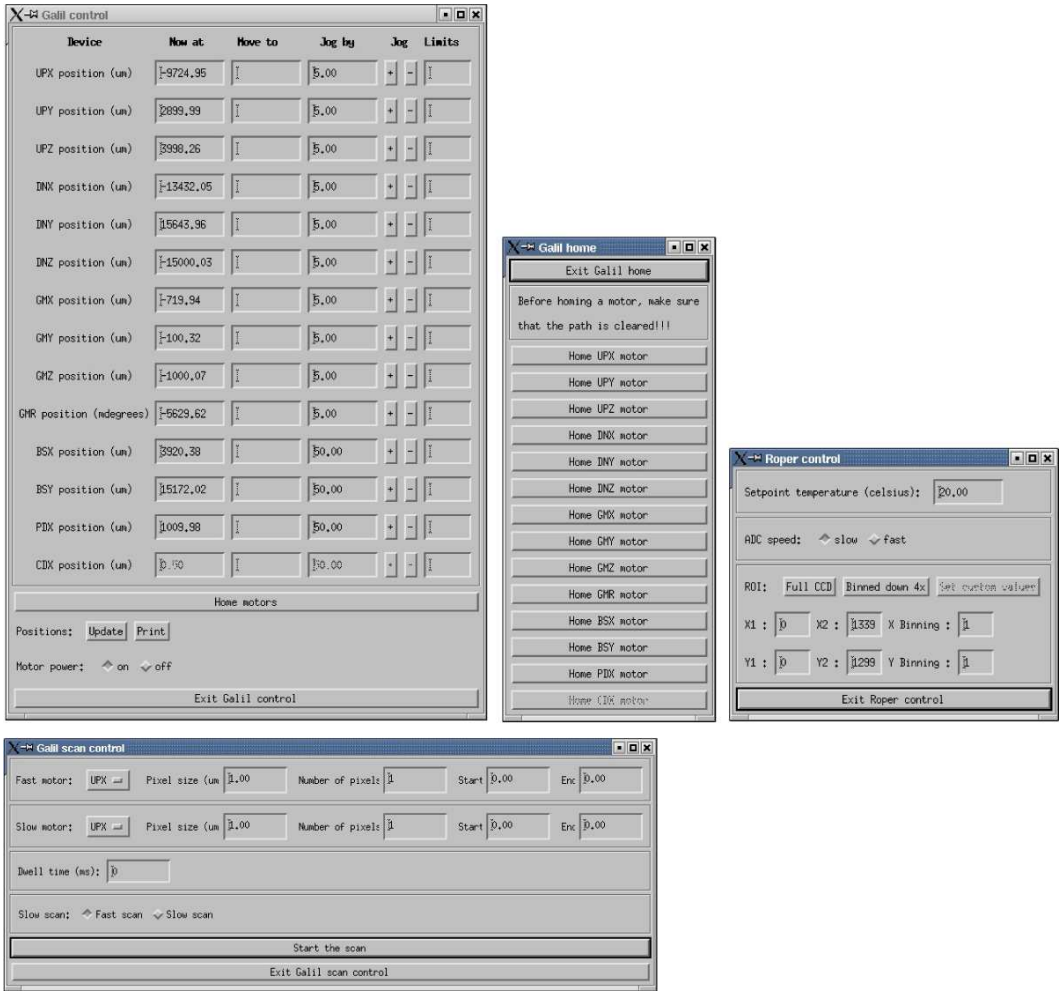

Figure 2.11: Graphical User Interface to control motors, set up scans, and set CCD parameters.

the calculated undulator output as a function of energy.

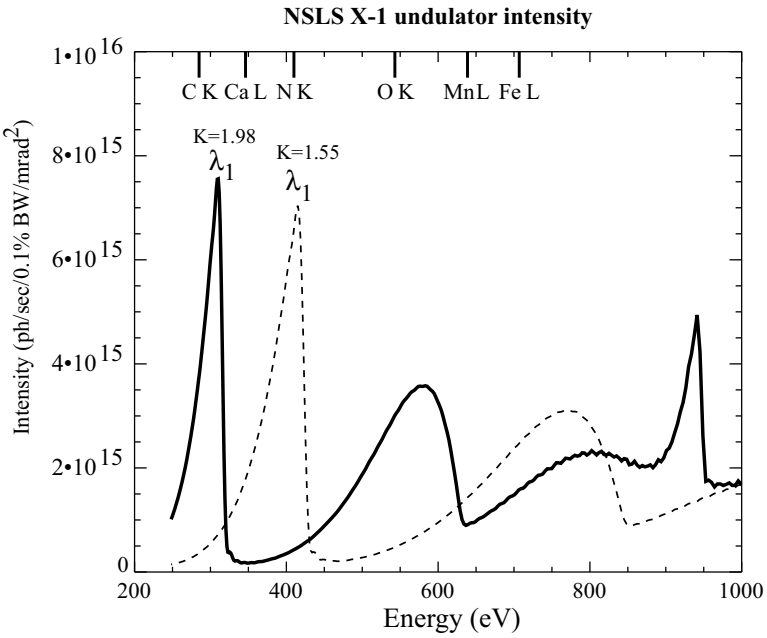

Figure 2.12: Calculated output of the NSLS X1 undulator. By changing the undulator gap, a different energy range can be accessed [reprinted from [Winn 2000a]].

The emittance of the electron beam, which is the product of the electron beam size and the divergence, is about $\epsilon_x = 75$ nm rad in the horizontal and about $\epsilon_y = 0.15$ nm rad in the vertical. The large horizontal emittance of the NSLS storage ring also results in a broadening of the undulator harmonics, since a range of single-electron emission angles are contributing to the total flux observed. This broadening makes it possible to do spectroscopy experiments without the need for changing the undulator gap.

Due to the large horizontal emittance, the X-ray beam can also be split by scraping mirrors into several beamlines operating simultaneously. About 35% of the radiation coming from the undulator is deflected to the X1-A branch whereas the rest goes to the X1-B beamline. The X1-A beam is then divided equally into two branchlines - X1-A1 and X1-A2. Both beamlines are

in principal identical, except that X1-A2 is optimized for energies around the carbon K-edge whereas X1-A1 is optimized for the oxygen K-edge. Both use a spherical grating monochromator and several slits to define the temporal and spatial coherence of the X-ray beam.

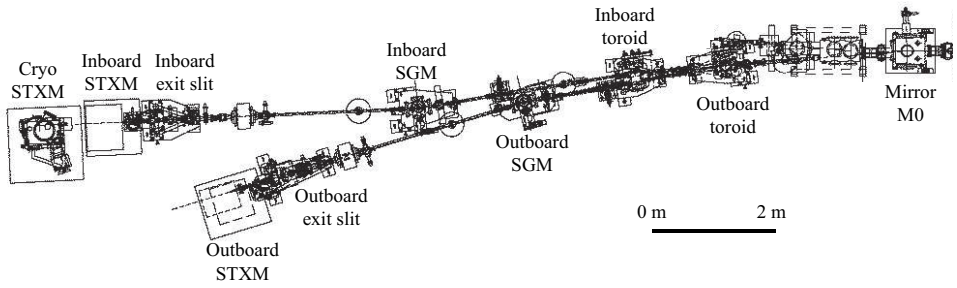

Figure 2.13: Schematic top view of the NSLS X1-A beamlines [reprinted from [Winn 2000a]].

Figure 2.13 shows the layout of the X1-A1 and X1-A2 branchlines [reprinted from [Winn 2000a]]. Two identical room-temperature Scanning Transmission X-ray Microscopes (STXMs) are located on each of the X1-A branchlines. In addition to the room-temperature STXM [Feser 2001] the X1-A1 branch also has a cryo STXM [Maser 2000], which can be used for radiation sensitive specimens. The cryo STXM was also used for the radiation damage studies described in Chapter 5.

The spherical grating monochromator with fixed exit arm provides good spectral resolution since the coherent part of the beam is kept small at the grating. Adjustment of the energy resolution is therefore made by changing the size of the entrance slit, trading good spectral resolution with less photon flux or lower spectral resolution with higher photon flux.

The transverse coherence is adjusted by the opening of the exit slit. In the vertical plane, the toroidal mirror focuses the undulator source onto the vertical exit slit and the spherical grating monochromator focuses the undulator source in the horizonal plane (see Figure 2.14). Behind the exit slits, order-sorting mirrors provide a way of cutting off unwanted higher energies, which would otherwise come through in addition to the desired energy. They

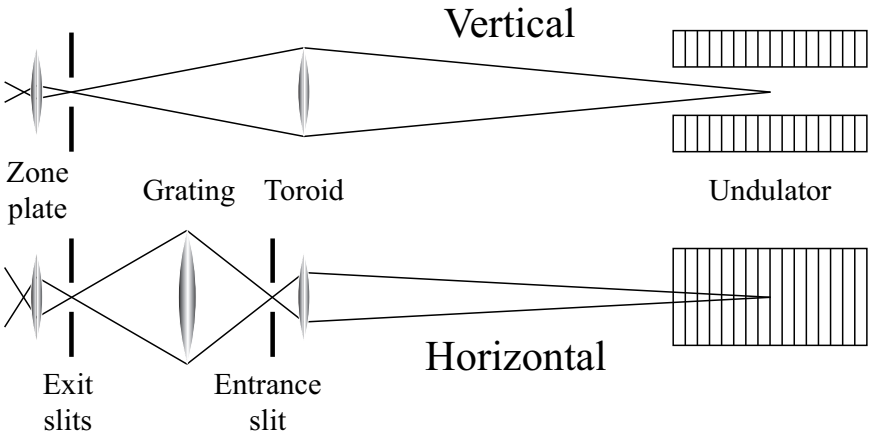

Figure 2.14: Schematic of the optics used in the X1-A2 branch. The X1-A1 branch uses a similar arrangement. [reprinted from [Winn 2000a]].

consist of two parallel grazing-incidence mirrors with the incident angle chosen so that one obtains good reflectivity at the desired energy and low reflectivity at higher energies. Therefore the mirrors effectively cut off higher energies. After the order-sorting mirrors, the beam passes a small silicon nitride window, which separates the ultra-high vacuum section of the beamline from the lower- or no-vacuum section of the experimental stations.

2.3 Advanced Light Source beamline 9.0.1

Beamline 9.0.1 located at the Advanced Light Source (ALS) at Lawrence Berkeley National Laboratory (LBL) is a beamline that shares the undulator output with another beamline [Heimann 1997]. The undulator is a 10 cm period undulator providing near-UV photon energies in the first harmonic. This radiation is used in the other beamline 9.0.2 as a pink beam (a once reflected but unmonochromatized undulator beam) for chemical dynamics experiments. Experiments on beamline 9.0.1 are designed to work off the third undulator harmonic, providing photons from about 500 eV to 800 eV. An off-axis zone plate monochromator provides the necessary spectral resolving power needed for the diffraction and holography experiments described in this thesis [Howells 2002]. Figure 2.15 shows the schematic diagram of beamline

9.0.1 and Figure 2.16 shows the layout.

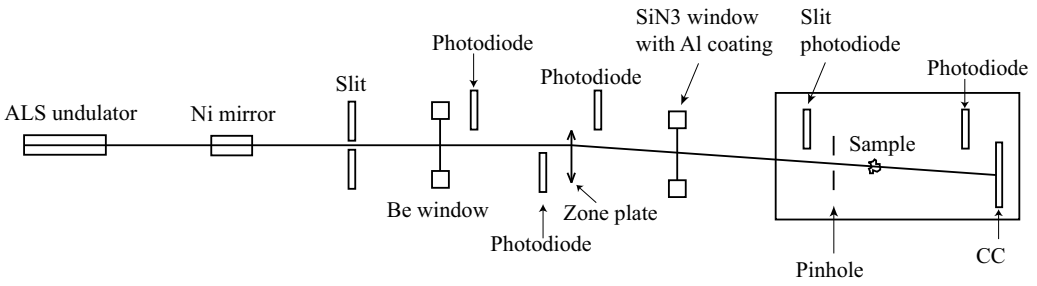

Figure 2.15: Schematic of the ALS beamline 9.0.1: X rays generated in the undulator are deflected by a Ni mirror and pass through a Be window. The zone plate serves as a monochromator and deflects the X-ray beam downwards. The pinhole selects the energy and defines the coherence. The X-ray beam is then passed onto the sample and the diffracted light detected with the CCD. Several photodiodes and a shutter allow interception and measurement of the X-ray beam along the beamline.

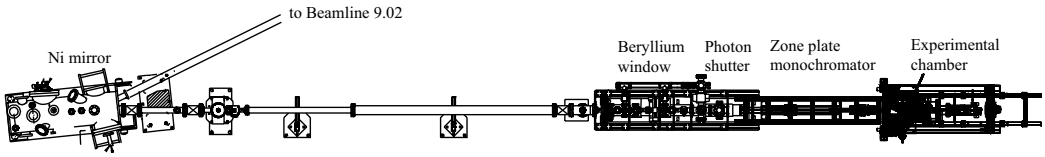

Figure 2.16: Layout of the ALS beamline 9.0.1. The distance between the Ni mirror and the experimental chamber is about 10 m.

The photons coming from the undulator are passed through a 0.8 mm by 0.8 mm Beryllium window. The Beryllium window also gets rid of the unwanted first harmonic of the undulator and separates the ultra-high vacuum section, connected to the ALS storage ring, from the high-vacuum section of

the zone plate monochromator and the experimental endstation. After the X-ray beam passes the Beryllium window, it is incident on the off-axis zone plate monochromator. The monochromator is a segment of a larger mathematical zone plate (see Figure 2.17), which acts as a grating. The properties of the monochromator are discussed in the following sections.

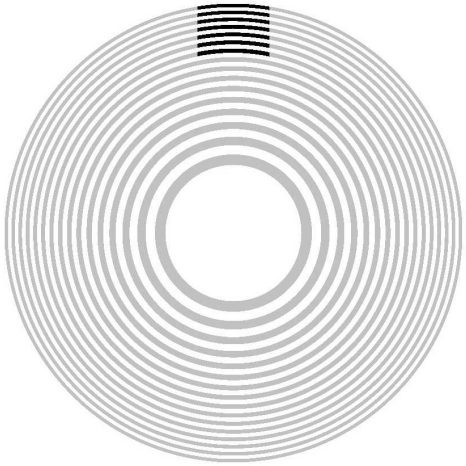

Figure 2.17: Schematic of the ALS 9.0.1 zone plate monochromator. The actual zone plate window, where the zones are written, is just a small area (black zones) of the whole mathematical zone plate (grey zones).

A 5 μm diameter pinhole in the experimental chamber is placed at the positive first-order focus of the zone plate monochromator. The pinhole has the purpose of selecting the energy of the X rays since the zone plate monochromator is a chromatic optic, which spreads the energies along the optical axis. In addition to selecting the energy, the pinhole also serves as an aperture, defining the transverse coherence as discussed in Section 3.1.6. Between the zone plate monochromator and the pinhole is a silicon frame which has an opening of about 400 μm and blocks out all zone plate orders except for the desired first order. A silicon nitride window coated with a 20 nm Al coating can be inserted to block out any visible light that comes down the beampipes from various gauges and stray light. Several photodiodes are located along the beamline which can be inserted to measure the intensity of the X-ray beam.

Figure 2.18 shows a picture of the actual beamline with the experimental chamber.

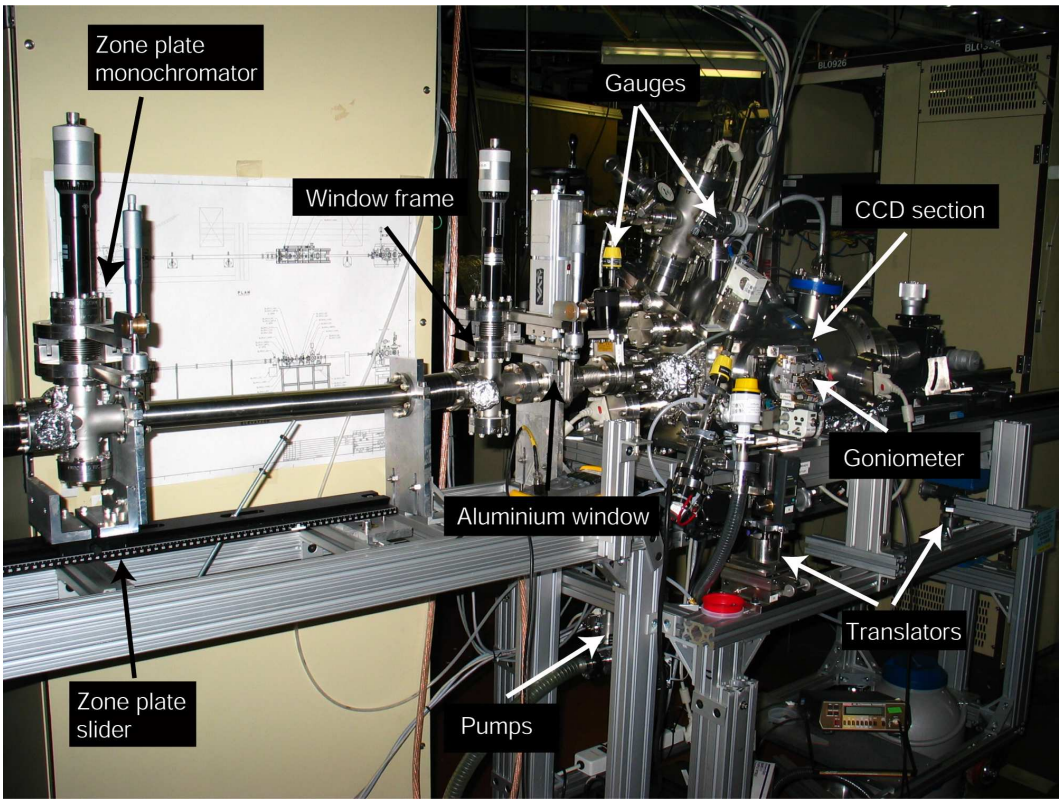

Figure 2.18: View of the ALS 9.0.1 endstation. Shown on the left side is the zone plate monochromator setup with the manual slider to change the energy. Downstream of it is the window frame and Aluminium window setup and the experimental chamber.

2.3.1 Properties of the zone plate monochromator

We started using the second generation of zone plate monochromators produced by Xradia, Inc. and designed by M. Howells. Table 2.1 summarizes the design parameters of the zone plate monochromator.

Mathematical diameter [mm]	7.116
Outermost zone width [nm]	250
Number of half-period zones in segment	1818
Number of half-period zones in entire mathematical zone plate	7011
Au zone thickness [nm]	200
Cu coating on upstream side [nm]	100
Cu coating on downstream side [nm]	100
Size of written area [μm^2]	700x700
Size of zone plate membrane [μm^2]	500x500

Table 2.1: Parameters of the ALS 9.0.1 zone plate monochromator.

Spectral resolution

We start by looking at the spectral resolving power of the zone plate monochromator. Using the Rayleigh criterion, the first dark ring of the diffraction pattern for wavelength $\lambda + \Delta\lambda/2$ should coincide with the peak of the central disk for wavelength $\lambda - \Delta\lambda/2$. We can derive the spectral resolving power as

$$R = \frac{\lambda}{\Delta\lambda} \tag{2.5}$$

$$= \frac{N}{2}, \tag{2.6}$$

where N is the number of half-periods [Niemann 1974, Thieme 1988]. With the number of half-periods given in Table 2.1 we can expect a spectral resolution of $R = 909$, which is sufficient for the diffraction experiments.

Matching the source size

The photons from the undulator are diverging as they travel along the beamline. 16 m downstream of the undulator is a Nickel mirror at a 3^o incident angle to the beam, which reflects the beam into the 9.0.1 beamline. The mirror is a focusing mirror with the focus being another 16 m downstream (see Figure 2.19).

Table 2.2 summarizes the ALS storage ring and ALS 9.0.1 parameters.

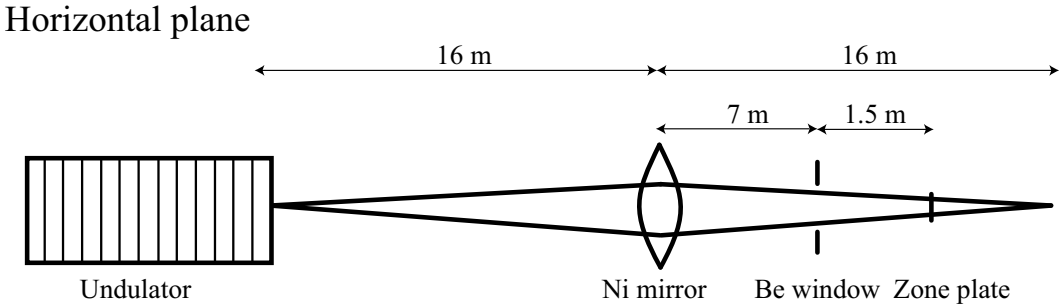

Figure 2.19: Schematic of the horizontal plane at ALS beamline 9.0.1. The divergent beam from the undulator source is focused by the Nickel mirror.

Horizontal beam size σ_h	310 μm
Horizontal divergence σ'_h	23 μrad
Vertical beam size σ_v	23 μm
Vertical divergence σ'_v	6.5 μrad
Source to focusing mirror distance d_{S2M}	16.0 m
Focusing mirror to focus distance d_{M2F}	16.0 m
Focusing mirror to Beryllium window distance d_{M2BW}	7.0 m
Beryllium window to zone plate distance d_{BW2ZP}	1.5 m

Table 2.2: Parameters of the ALS storage ring and ALS 9.0.1 beamline [ALS 2004].

We can now calculate the expected beam size at the Beryllium window for the horizontal and vertical plane. For the horizontal plane the expected beam size s_h is

$$s_h = \sigma_h + \sigma'_h(d_{\mathrm{M2F}} - d_{\mathrm{M2BW}} - d_{\mathrm{BW2ZP}}), \tag{2.7}$$

and the expected size for the vertical plane is

$$s_v = \sigma_v + \sigma'_v(d_{\mathrm{S2M}} + d_{\mathrm{M2BW}}). \tag{2.8}$$

Using the values from Table 2.2 we find $s_h = 482$ μm and $s_v = 172$ μm. From this we see that the 800 μm by 800 μm Beryllium window is large enough to let the desired X-ray pass. To calculate now the expected beam size at the zone plate location, we have to add $\sigma'_{h/v} \cdot d_{\mathrm{BW2ZP}}$ to s_h and s_v to get $s_h = 517$ μm and $s_v = 182$ μm. Comparing this to the 500 μm by 500 μm zone plate window, we see that the illumination across the zone plate window might not be uniform.

Heatload

Since the incident beam has a very high power density of 0.37 W/mm^2, the heatload on the zone plate has to be carefully evaluated to prevent thermal damage. It is therefore important to have a good heat conduction path across the zone plate window. In our case this is assured by the copper coating on the zone plate (for a detailed calculation of the heatload see Howells *et al.* [Howells 2002]).

Position dependence

Positioning of the zone plate monochromator is done by a manual translation-tilt stage as shown in Figure 2.18. The whole setup sits on a manual slider to change the photon energy.

Previously, zone plate spectra were recorded by moving a slit in the vertical direction and measuring the transmitted photon flux. Since this was done manually, it took about 30-60 minutes to acquire an accurate spectrum. With the new chamber that we developed, this process is automated. In addition to automating the recording process, we also installed a new photodiode which is covered by a 25 μm wide and 3 mm long slit aperture. Such an arrangement makes it possible to record a complete zone plate spectrum in about 1 minute. We can therefore optimize the position of the Beryllium window and the zone plate to be exactly on-axis by looking at the spectrum depending on the position offset from the undulator axis. Shown in Figure 2.20 is

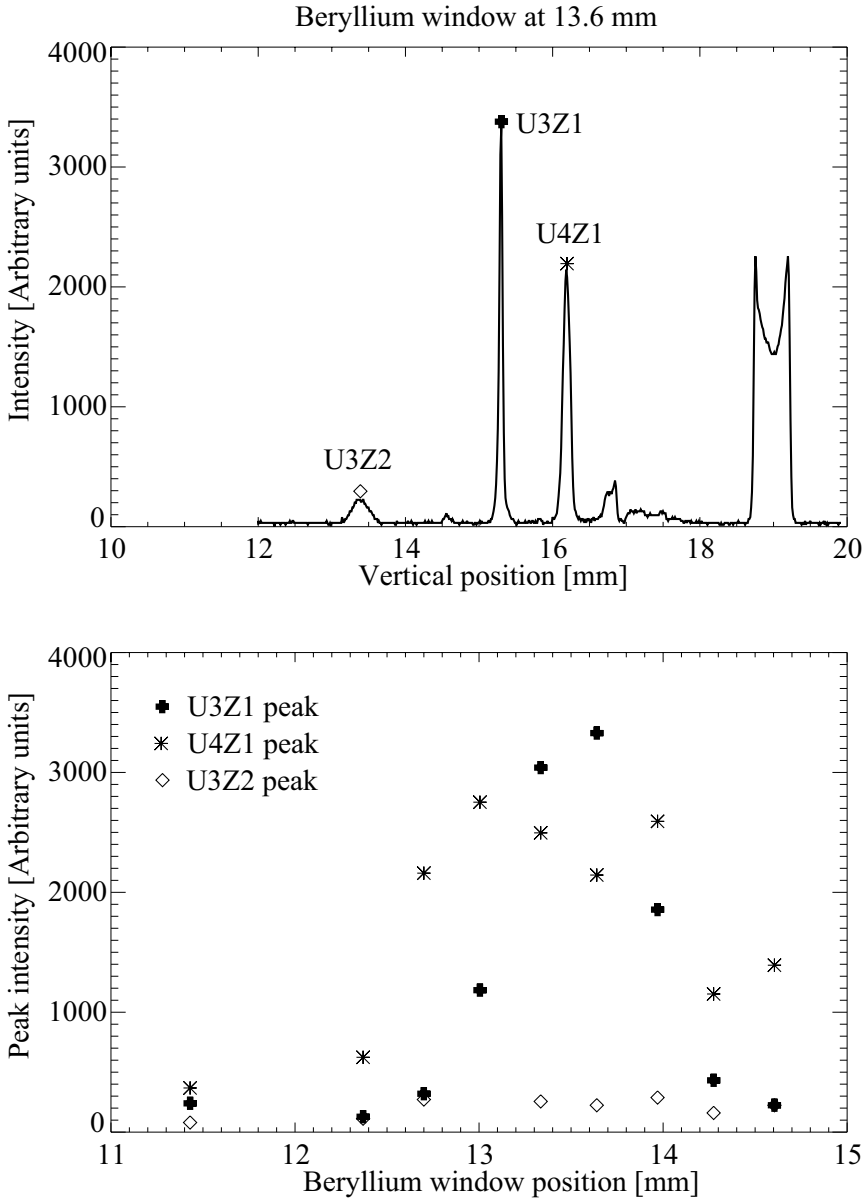

Figure 2.20: Top: sample spectrum of the zone plate monochromator taken at optimum position of the Beryllium window. To find this optimum position, spectra are taken at various positions. Bottom: Peak intensity for U3Z1, U4Z1 and U3Z2 at various Beryllium window positions.

a spectrum recorded at the optimum Beryllium window position. The image shows that different harmonics, beside the wanted third undulator harmonic and first zone plate harmonic (U3Z1), are present. By moving the Beryllium window, the intensity of U3Z1 can be maximized. A spectrum is recorded at each window position. As the window is moved, the other unwanted orders change their intensity. This is summarized in the bottom graph of Figure 2.20 for U3Z1, U4Z1 and U3Z2.

Efficiency of the zone plate monochromator - Theory

Total absorption Another important property of the zone plate monochromator is its efficiency. We start out by calculating the intensity after the zone plate, where we have to consider the absorption in the two copper layers and in the silicon nitride layer (see Figure 2.21). At the locations of the gold zones,

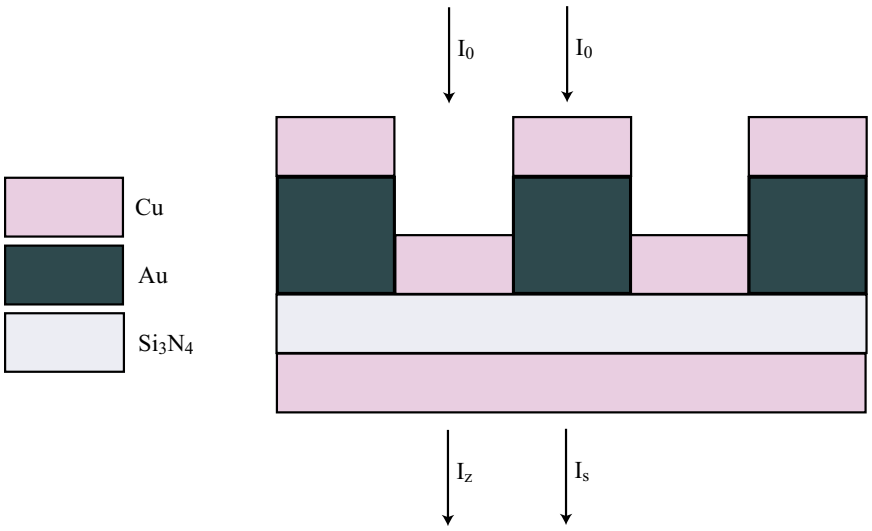

Figure 2.21: Schematic of the profile of the ALS zone plate monochromator. The gold zones are 200 nm thick and are on top of a 100 nm thick silicon nitride window. A 100 nm thick copper layer is added on top and bottom of the zone plate to provide a good heat path.

we also have to include the absorption due to the gold. The transmission

through the transparent zones is

$$T_{\mathrm{S}} = T_{\mathrm{Cu}} T_{\mathrm{SiN_3}}, \tag{2.9}$$

where T_{Cu} and $T_{\mathrm{SiN_3}}$ is the transmission coefficient for the copper layer and the silicon nitride layer. The transmission coefficients are given as $T = e^{-\mu t}$, where μ is the absorption coefficient and t the thickness. The transmission after the opaque zones is

$$T_{\mathrm{Z}} = T_{\mathrm{Cu}} T_{\mathrm{SiN_3}} T_{\mathrm{Au}}, \tag{2.10}$$

where T_{Au} is the transmission coefficient for the gold zones. If the incident intensity is given by I_0, and assuming a mark to space ratio is 1:1, we can write for the transmitted intensity

$$\begin{aligned} I_{\mathrm{Trans}} &= I_{\mathrm{S}} + I_{\mathrm{Z}} \\ &= T I_0 \\ &= \frac{1}{2}(T_{\mathrm{S}} + T_{\mathrm{Z}}) I_0. \end{aligned} \tag{2.11}$$

Finally, the total absorption A follows from $1 = A + T$ and therefore

$$\begin{aligned} A &= 1 - \frac{1}{2} T_{\mathrm{Cu}} T_{\mathrm{SiN_3}} (1 + T_{\mathrm{Au}}) \\ &= 1 - \frac{1}{2} e^{-\mu_{\mathrm{Cu}} t_{\mathrm{Cu}}} e^{-\mu_{\mathrm{SiN_3}} t_{\mathrm{SiN_3}}} (1 + e^{-\mu_{\mathrm{Au}} t_{\mathrm{Au}}}). \end{aligned} \tag{2.12}$$

As described later, most of the diffraction experiments were done at 750 eV. Looking up the transmission coefficients for each material and its thickness [Henke 1993], we end up with an expected **total absorption** due to the zone plate of $A = 72\%$.

Diffraction efficiency The **diffraction efficiency** for the n-th order is given [Kirz 1974] by

$$\epsilon_n = \frac{1}{n^2 \pi^2} (1 + e^{-2kz\beta} - 2e^{-kz\beta} \cos(kz\delta)). \tag{2.13}$$

At 750 eV and a gold thickness of 200 nm, the diffraction efficiency in the first-order is $\epsilon_1 = 13.4\%$.

Efficiency of the zone plate monochromator - Experiment

A silicon photodiode was used to compare the intensity with and without the zone plate. The measured intensity without the zone plate is 2.3 mA at 750 eV and a storage ring current of 350 mA. The intensity on the photodiode drops to 0.8 mA when the zone plate is inserted. To verify the expected absorption from the zone plate, we have to account for the different area of the Beryllium window and the zone plate window. The area of Beryllium window is $A_{\mathrm{Be}} = 800^2\ \mu\mathrm{m}^2$, whereas the area of the zone plate window is only $A_{\mathrm{ZP}} = 500^2\ \mu\mathrm{m}^2$. Therefore we should expect an incident intensity of $I_0 = A_{\mathrm{ZP}}/A_{\mathrm{Be}} \cdot 2.345$ mA $= 0.91$ mA. However, using the calculated absorption factor from Eq. (2.12), we would expect to measure an intensity of $I_{\mathrm{Trans}} = (1 - A)I_0 = 0.26$ mA.

Possible reasons for this discrepancy could be some variations of the actual size of the Beryllium and zone plate window. Furthermore, as we have seen in Section 2.3.1, the size of the zone plate window is not ideally matched to the the size of the X-ray beam at the zone plate location. This would result in an uneven illumination of the zone plate, which in turn would make our flux per area calculations inaccurate.

Using the spectrum shown in Figure 2.23, we can calculate the first-order diffraction efficiency. If we integrate the intensity in the first-order I_{+1} and also integrate the intensity in the zero-order I_0, we find $f = I_0/I_{+1} = 3.2$. We are assuming now, that the measured transmitted intensity of $I_{\mathrm{Trans}} = 0.8$ mA is mainly due to the zero-order and positive and negative first-order of the zone plate and therefore write

$$\begin{aligned} I_{\mathrm{Trans}} &= I_{+1} + I_{-1} + I_0 \\ &= 2I_{+1} + fI_{+1} \\ &= (2 + f)I_{+1}. \end{aligned} \tag{2.14}$$

Here we have assumed that $I_{-1} = I_{+1}$ in agreement with Eq. (2.13). The diffraction efficiency can now be written as

$$\begin{aligned} \epsilon_{+1} &= \frac{I_{+1}}{I_0} \\ &= \frac{I_{\mathrm{Trans}}/(2 + f)}{I_0} \\ &= \frac{(1 - A)I_0/(2 + f)}{I_0} \\ &= \frac{1 - A}{2 + f}. \end{aligned}$$

In this case , we found $A = 0.7$ from our theoretical calculations in Eq. (2.12) and $f = 3.2$ from the measured spectrum. We therefore end up with an efficiency of $\epsilon_{+1} = 5.4\%$, which is less than the expected 13.4%.

The difference can be attributed to the fact that we have neglected other wavelengths that might contribute to the zero order. Furthermore, there is some error in the thickness of the zones and heat conduction material, which contributes to the observed difference. One would expect a lower efficiency, if the gold thickness is decreased (for example, $\epsilon_{+1} = 8.4\%$ at a gold thickness of 150 nm). There is also the possibility, that some residual resist was left during the zone plate fabrication process, which would degrade the efficiency. A combination of these factors could explain the low measured efficiency.

Photons for the experiment. The large number of coherent photons contributing to the diffraction pattern is of great importance to keeping exposure times low. At the ALS 9.0.l beamline the intensity after a 5 μm pinhole in the zone plate monochromator first-order focus is about 150 nA at 750 eV and a storage ring current of 330 mA. Using Eq. (2.4) we calculate that this current corresponds to $4.5 \cdot 10^9$ photons per second. Accounting for the area of the pinhole (5 μm diameter pinhole), we finally arrive at $2.3 \cdot 10^8$ photons per second per μm^2.

We can now compare the coherent flux density at the ALS 9.0.1 beamline with one at the NSLS X1 beamline. A typical flux for the diffraction experiment at X1 was about 2 nA or $8.6 \cdot 10^8$ photons per second through a 10 μm diameter pinhole at a photon energy of 530 eV. This translates into $1.1 \cdot 10^6$ photons per second per μm^2. We can see that the coherent flux density at the ALS is about 200 times higher than at the NSLS. This increase in flux is due to the slightly different design of the NSLS versus the ALS. The ALS is designed to put the coherent flux into a smaller area, and furthermore the source has an improved brightness. In addition to that, the ALS 9.0.1 beamline is also simple and efficient, therefore contributing to the increased photon flux density.

With the available flux at beamline 9.0.1, exposure times for diffraction patterns ranged from 0.1 seconds for the low spatial frequency information up to 100 seconds for the highest spatial frequency information recorded. Such short exposure times enable us to collect a complete diffraction pattern set in a few minutes. This makes it possible to collect diffraction patterns at many viewing angles needed for complete 3D reconstruction as will be shown in Chapter 4.

2.3.2 Choosing the right photon energy

The initial experiments were designed to run at about 520 eV, just below the oxygen K-edge, where carbon material is absorbent and water is transparent (see Section 1.1). Figure 2.22 shows the diffraction pattern of a collection of 50 nm diameter gold spheres with the energy tuned to 520 eV. The diffrac-

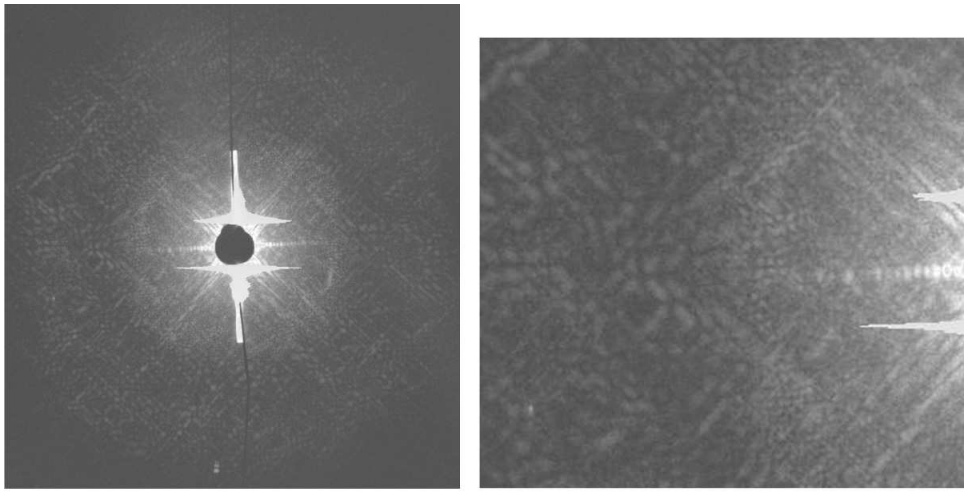

Figure 2.22: Speckle from a collection of 50 nm diameter gold spheres. Image a) shows the complete diffraction pattern and b) shows a magnified part of the diffraction pattern. Both images exhibit two speckle sizes. The larger speckle size is emerging from the desired energy, whereas the smaller speckle size at half the distance from the central beam results from double the desired energy.

tion pattern shows speckle emerging from the 520 eV and the first zone plate order (third undulator harmonic and first zone plate order: U3Z1). Speckle is a phenomenon that occurs when imaging with a coherent beam. In our case, the observed speckle is due to an introduced phase shift along the scattering object, leading to a dephased amplitude spread function at the observation plane. The size of the speckle is proportional to the wavelength and inversely proportional to the sample size. As will be discussed in Section 4.1.4, Eq.

(4.13), the size d can be written as

$$x = \frac{\lambda z}{d}, \tag{2.15}$$

where d is the object size, λ the wavelength and z the distance between the detector and the object. In addition to the desired speckle pattern (from U3Z1) we can alse see another speckle pattern in Figure 2.22, which appears at half the radius. The speckles in this second pattern are half the size as the speckle due to U3Z1. We concluded that the second speckle pattern must be due to the sixth undulator harmonic combined with the second zone plate order (U6Z2). Both energies are focused by the zone plate monochromator to the same focal spot on the optical axis and therefore contribute to the diffraction pattern. To effectively cut off the higher energy we moved to 750 eV in the third undulator harmonic. At this energy, the sixth undulator harmonic (1500 eV) is cut off by the upstream nickel mirror. A spectrum recorded at 750 eV is shown in Figure 2.23 and diffraction patterns taken at this energy are discussed in Chapter 4.

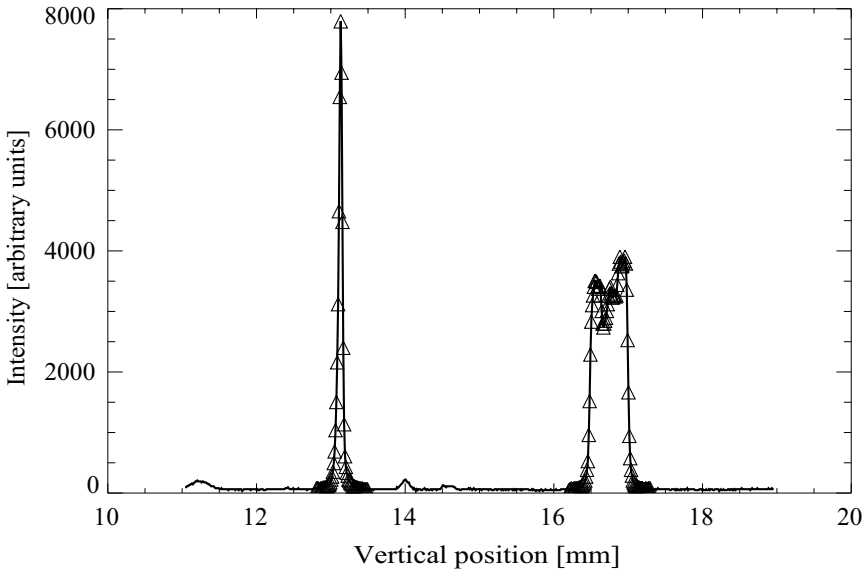

Figure 2.23: Spectrum of the ALS zone plate monochromator taken at 750 eV. The zero and first order are clearly visible. The triangles indicate the parts of the spectrum that were used for the diffraction efficiency calculations.

Going to a higher energy works well for non-hydrated samples; for samples with a thick ice layer, absorption above the oxygen K-edge would otherwise render the specimen opaque. To effectively eliminate the higher order contributions when working just below the oxygen K-edge, which is desirable for hydrated specimens, an order sorting mirror assembly must be installed. Such an assembly is already in use at the X1 beamlines at the NSLS [Dayton 2000] and could be copied and employed at the 9.0.1 beamline at the ALS for future experiments.

Chapter 3

In-line (Gabor) holography

This chapter describes the use of in-line holography as a tool for 3D imaging using soft X rays. I start out with a brief history of in-line holography, followed by a more detailed discussion of the basic principles of holography. The third section includes experimental considerations and limitations and also describes some experimental results. The chapter will conclude with a discussion of the results and an outlook for applying in-line holography to future experiments.

3.1 Fundamentals of holography

In general, a hologram is the recorded superposition or interference of a wave emerging from an object and a reference plane wave. Figure 3.1 shows the general arrangement for recording in-line holograms. Here, an object is illuminated with a coherent reference wave A. The object gives rise to a scattered wavefield B. The recorded hologram or interference pattern is obtained from the intensity of the complex superposition of wavefield A and B at the detector plane. As we will see later, the phase and amplitude of the diffracted wavefield are encoded in the hologram so that a reconstruction of the scattering object is possible.

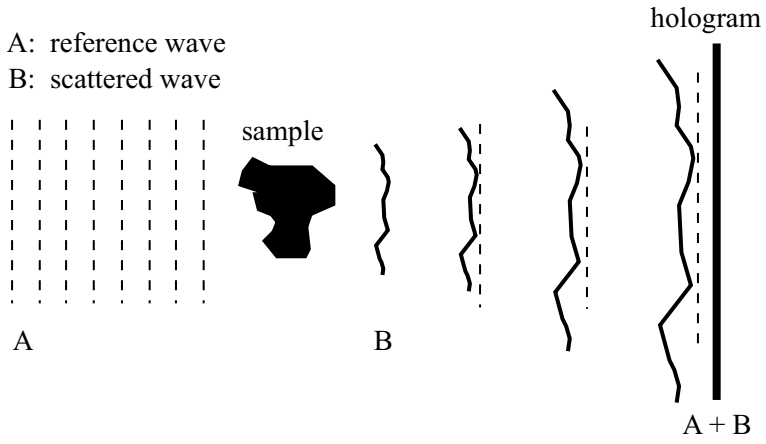

Figure 3.1: A wavefield A is incident on a scattering object. The scattered wave B and the reference wave interfere and form the hologram.

The intensity of the interference pattern (hologram) where A is the reference wave and B is the scattered wave can be written as

$$\begin{aligned} I &= |A+B|^2 \\ &= (A+B)(A+B)^\star \\ &= AA^\star + B^\star B + AB^\star + A^\star B \\ &= I_r + I_s + AB^\star + A^\star B. \end{aligned} \tag{3.1}$$

Here we have substituted $I_r = AA^\star$ and $I_s = BB^\star$ as the uniform intensity of the reference wave and the intensity of the scattered wave (diffraction pattern), respectively. The terms $AB^\star$ and $A^\star B$ represent the hologram and will be discussed in more detail in Section 3.1.2.

3.1.1 The hologram as a superposition of zone plates

A very intuitive model of generating a hologram was developed in 1950 by Rogers [Rogers 1950]. He proposed to think of the scattering object as a collection of individual point scatterers. The interference of the scattered wavefield from such a point scatterer with the reference wave will be a Fresnel zone plate (see Section 1.3) at the detector plane. With each point scatterer producing a zone plate, the recorded hologram is then the complex superposition of all the zone plates. Figure 3.2 illustrates the construction of the hologram from three point sources. The picture of a hologram as a superposition of zone plates is

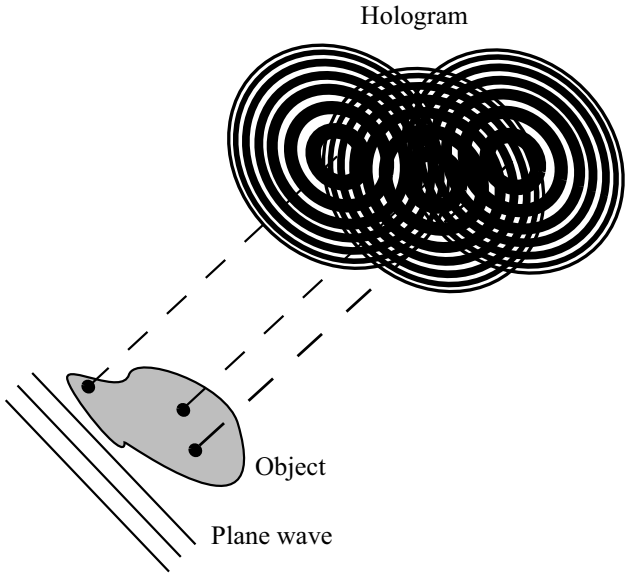

Figure 3.2: The hologram as a superposition of zone plates: each point in the object produces a zone plate when illuminated with a plane wave. The hologram is the complex superposition of those zone plates.

helpful in understanding the properties and limitations of a hologram and is therefore used in the following sections.

Mathematical description of Rogers' zone plate hologram. To describe Rogers' idea mathematically, the incident plane wavefield can be written as

$$A = A_0 e^{-ikz}. \tag{3.2}$$

In the case of a single elastic scatterer, there is only a phase shift of $\pi/2$ but no attenuation and therefore

$$B = iB_0 \frac{e^{-ikr}}{r}, \tag{3.3}$$

where $r = \sqrt{x^2 + y^2 + z^2}$. Inserting both into Eq. (3.1) gives

$$\begin{aligned} I &= |A + B|^2 \\ &= {A_0}^2 + \frac{B_0^2}{r^2} - 2\frac{A_0 B_0}{r} \sin[k(r - z)]. \end{aligned} \tag{3.4}$$

Since $\frac{x^2+y^2}{z^2} \ll 1$, we can use the binomial expansion of the square root

$$\begin{aligned} \sqrt{1+a} &= 1 + \frac{1}{2}a - \frac{1}{8}a^2 + \frac{1}{16}a^3 - ... \\ &\approx 1 + \frac{1}{2}a \end{aligned} \tag{3.5}$$

to get

$$r \approx z(1 + \frac{x^2 + y^2}{z^2}) \tag{3.6}$$

and

$$r^2 \approx z^2. \tag{3.7}$$

Inserting Eq. (3.6) and Eq. (3.7) into Eq. (3.4) results in the hologram intensity

$$I = {A_0}^2 + \frac{B_0^2}{z^2} - 2\frac{A_0 B_0}{z} \sin[k\frac{x^2 + y^2}{2z}]. \tag{3.8}$$

One of the requirements of in-line holography is that the object is a weak scatterer ($B \ll A$); the second term in Eq. (3.8) can then be dropped to yield the hologram intensity

$$I \approx {A_0}^2 - 2\frac{A_0 B_0}{z}\sin[k\frac{x^2+y^2}{2z}]. \tag{3.9}$$

From previous discussion of zone plates (see Section 1.3) we recognize that the positions of the sinusoidal fringes represented in Eq. (3.9) coincide with the zones used in a zone plate. However, while the usual zone plate gives rise to several higher-order foci due to the step-like profile of a zone plate, the sinusoidal zone plate hologram concentrates the power into the first orders.

3.1.2 Hologram reconstruction

The easiest way to reconstruct a recorded hologram is to simply illuminate the hologram (processed now to produce opacity proportional to the intensity distribution in the recording) with the original wavefield A that was used to record the hologram. We can therefore take Eq. (3.1) and multiply the hologram intensity with the original wavefield A and get

$$\begin{aligned} R &= AI \\ &= A(AA^\star + B^\star B + AB^\star + A^\star B) \\ &= AAA^\star + AB^\star B + AAB^\star + AA^\star B \\ &= AI_r + AI_s + AAB^\star + I_r B \\ &= A(I_r + I_s) + A^2 B^\star + I_r B, \end{aligned} \tag{3.10}$$

where we have substituted $I_r = AA^\star$ and $I_s = BB^\star$ as the intensity of the reference wave and the intensity of the scattered wave (diffraction pattern), respectively. The reference wave has generally no structure (for example, it might be a plane wave) and therefore I_r will be constant, contributing a DC background to the reconstruction. Since a requirement for in-line holography is that the object is a very weak scattering object, the second term I_s, being the diffraction intensity of the scattering object, can be neglected. The third and fourth terms in Eq. (3.10) are the important contributing terms in the reconstruction. The fourth term ($I_r B$) is a direct representation of the scattering object and leads to a real image. The third term ($A^2 B^\star$) leads to a virtual image of the object. These two reconstructions of the object are the so-called **twin images**. In the in-line holography arrangement, both images are on-axis. Therefore when viewing one image, one always has an out-of-focus

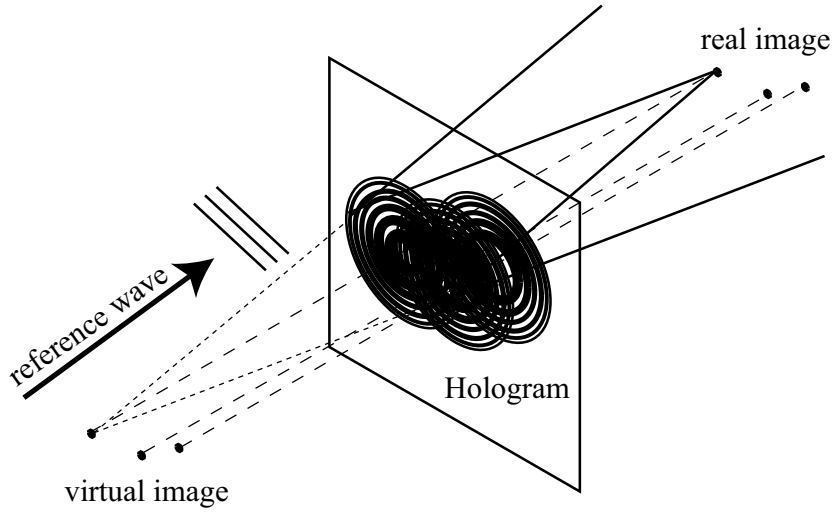

Figure 3.3: The real and virtual images of the scattering object are formed when the hologram is illuminated with the original reference wave. In this example, the illuminating wavefield is a plane wave propagating from left to right.

contribution from the other image; this is generally referred to as the **twin image problem** of holography.

Figure 3.3 demonstrates the emerging real and virtual images using Rogers' zone plate model. Here a plane wave incident on a hologram made of several zone plates will focus the reconstructing wavefield, therefore creating a real image due to the positive diffraction order. The virtual image is created due to the negative diffraction order of the zone plate.

We can also illuminate the hologram with the complex conjugate of the reference wave and get the following reconstruction:

$$R \;=\; A^{\star}(I_r + I_s) + I_r B^{\star} + A^{\star} A^{\star} B \tag{3.11}$$

In this case, the second term is a converging wave which leads to a real image. However, the conjugate nature of the resulting image makes the image pseudoscopic (inverted depth) and the interpretation of the reconstructed object becomes more difficult because of the unusual view.

3.1.3 Empty specimen requirement

From the discussion in Section 3.1.1 we can already recognize a major limitation of in-line holography: in order to form a Fresnel zone plate, **the specimen has to be empty so that the ongoing reference wave is not corrupted**. Gabor suggested that the shadow of the specimen should fill up no more than 1% of the area of the hologram, which means that

$$r_h > 10 r_s. \tag{3.12}$$

Using Eq. (1.27) and that the numerical aperture of the system is $N.A. = r_h/f$, we can write

$$f > \frac{10 r_s \delta_t}{0.61 \lambda}. \tag{3.13}$$

This empty specimen requirement is a major limitation of Gabor holography and restricts the types of specimens that can be used. As an example, we take a specimen radius of $R = 2$ μm, a resolution element of $\delta_t = 20$ nm and 530 eV X rays. This results in a requirement that $f > 280$ μm. Recording the hologram at this distance is not really the limitation. The difficulty lies in providing a reference wave which is coherent over such a large area ($r_h = 20$ μm). This aspect will be further discussed in Section 3.1.6.

3.1.4 How many fringes do we need to detect?

Since the hologram can be thought of as a superposition of several zone plates, we can apply the properties of zone plates from section (1.3). There we found that the number of zones N is given by

$$N = \frac{\lambda f}{4 \delta_{r_N}{}^2}. \tag{3.14}$$

Therefore, $\lambda = 2.34$ nm, $f = 280$ μm and $\delta_t = 20$ nm yields $N = 410$. From Eq. (1.24) we can also determine the diameter of the hologram. For our example we get $d = 2r_N = \sqrt{N \lambda f} = 32.8$ μm. This means that we have to provide a reference wave that is coherent over the diameter d and our detector has to be able to record the $N = 410$ fringes. Providing the necessary spatial coherence is not really difficult to do with an undulator source. However, recording all fringes is quite demanding as we will see in Section 3.1.7.

3.1.5 Fringe visibility

In order to properly record a hologram one has to assure that the recorded fringes have a high enough contrast to be recorded by the detector. We can refer to this as **fringe visibility**, which is written as

$$V = \frac{I_{\max} - I_{\min}}{I_{\max} + I_{\min}}. \tag{3.15}$$

Using Eq. (3.9) we can write for the maximum intensity in the hologram

$$I_{\max} = {I_r}^2 + 2\frac{\sqrt{I_r I_s}}{z} \tag{3.16}$$

and for the minimum intensity

$$I_{\min} = {I_r}^2 - 2\frac{\sqrt{I_r I_s}}{z}. \tag{3.17}$$

Inserting $I_{\max}$ and $I_{\min}$ into Eq. (3.15), we end up with

$$\begin{aligned} V &= \frac{2}{z}\sqrt{\frac{I_s}{I_r}} \\ &= \frac{2}{z}\sqrt{I_s} \\ &= \frac{2}{z}|B_s|, \end{aligned} \tag{3.18}$$

where $|B_s|$ is the amplitude of the scattered wave and we have set the intensity of the reference wave to one. From this we can see that the fringe visibility is directly proportional to the amplitude of the scattered wavefield.

3.1.6 Coherence requirements in holography

In order to record a hologram, we have to ensure that each point within the object is capable of interfering with each point within the reference source. To describe these requirements mathematically, one distinguishes between **temporal** or **longitudinal coherence** and **spatial** or **transverse coherence**. Temporal coherence describes the phase relationship between points along the direction of propagation whereas spatial coherence describes the phase relationship between points located in the plane perpendicular to the direction of propagation. Real light sources have only a degree of temporal and spatial

coherence, usually written as the **complex degree of coherence** γ. The degree of coherence is directly proportional to the fringe visibility [Collier 1971] by

$$V = \frac{2|\gamma_{12}|}{\sqrt{\frac{I_r}{I_s}} + \sqrt{\frac{I_s}{I_r}}}, \tag{3.19}$$

and

$$\gamma_{12(\tau)} = \frac{< E_{1(t+\tau)} E_{2(t)} >}{\sqrt{< |E_1|^2 >< |E_2|^2 >}}. \tag{3.20}$$

Here $\gamma_{12(\tau)}$ is expressed as the normalized correlation between the electric fields of two waves. In order to get good fringe visibility one has to establish sufficient temporal and spatial coherence.

Temporal coherence

The coherence length (considering a phase shift of π) can be written as

$$\begin{aligned} \Delta l &= c\Delta t \\ &= \frac{c}{\Delta\nu} \\ &= \frac{\lambda\nu}{\Delta\nu} \\ &= \frac{\lambda^2}{\Delta\lambda}, \end{aligned} \tag{3.21}$$

where Δt is the coherence or correlation time which then was expressed by the bandwidth $\Delta\lambda$ of the radiation.

Taking again the model by Rogers, we can consider the path difference that a ray emerging from the N-th zone has to an axial ray. The path difference between those two rays is $N\frac{\lambda}{2}$ resulting in a $\pi/2$ phase shift. We can therefore write

$$\frac{\lambda^2}{\Delta\lambda} = N\lambda \tag{3.22}$$

or

$$\frac{\lambda}{\Delta\lambda} = N. \tag{3.23}$$

Using Eq. (1.26) we can substitute the number of zones N and get

$$\frac{\lambda}{\Delta\lambda} = \frac{\lambda f}{4{\delta_r}_N{}^2}. \tag{3.24}$$

As an example we take $\lambda = 2.34$ nm, $f = 280$ μm and $\delta_{rN} = 20$ nm and get $\frac{\lambda}{\Delta\lambda} = 410$. Multiplying the resolving power by the wavelength results in the temporal coherence length and is in this case $\Delta l = 1$ μm. Such a resolving power is relatively easy to achieve with grating monochromators. In fact, the grating monochromator used at the X1A beamlines at the NSLS are able to provide a resolving power of more than 4000. However, narrower bandwidth also goes along with a loss of photon flux.

Spatial coherence

When using a monochromator as described above, the radiation can be treated as quasi-monochromatic and we have to worry about the spatial coherence. The complex degree of coherence $\gamma_{12(\tau)}$ can then be written as a complex degree of spatial coherence ($\gamma_{12(\tau)} \rightarrow \mu_{12}$). The van Cittert-Zernike theorem (see for example [Born 1980]) relates the degree of spatial coherence to the Fourier transform of the intensity distribution of the source. An important implication of this theorem is that partially coherent light can be retrieved even from a non-coherent source by using an aperture in front of the source. If the spatial coherence is provided by a pinhole with radius ρ, we can use the illumination from the center half of the Airy disk to get coherent light. The radius of the first minimum of the Airy function is at an angle of

$$\Theta = 0.61\frac{\lambda}{\rho}. \tag{3.25}$$

Taking half of this angle and a distance l away from the pinhole with the angle Θ which is small, we get sufficient coherence within

$$r_{\mathrm{coh}} = 0.31\frac{\lambda l}{\rho}. \tag{3.26}$$

This is, of course, only valid if we are in the far-field. In the near-field the radius would correspond to the ringing that occurs around the pinhole illumination.

As an example, using $\lambda = 2.34$ nm, $l = 1$ m and $\rho = 20$ μm gives a coherence width of $r_{\mathrm{coh}} = 36$ μm. These requirements are easy to accommodate. However, in addition to decreased photon flux resulting from the monochromator used to provide temporal coherence, we now have an additional decrease in photon flux due to the introduced aperture. We can see from this discussion, that holography is a photon hungry experiment and really needs a bright photon source such as an undulator source!

3.1.7 Detector resolution

Due to the analogy of the hologram as a collection of zone plates, we can state a requirement on the necessary detector resolution. Namely, the detector pixel size can immediately be taken from Eq. (1.28) by substituting δ_t for the desired resolution of the hologram and δ_{r_N} for the maximum detector pixel size which is still sufficient for recording a hologram at the desired resolution. We can therefore write

$$\delta_{r_N} = \frac{\delta_t}{1.22}. \tag{3.27}$$

A desired resolution of 20 nm would for example require a detector pixel size of about 16 nm or less. Here lies yet another limitation of in-line holography: **the resolution is limited by the pixel size of the detector.**

Modern photoresists such as poly(methylmethacrylate) (PMMA) meet those requirements and offers a resolution of about 10 nm [Feder 1976, Spiller 1977]. In fact, PMMA has been successfully used to record high-resolution holograms with fringes out to about 40 nm of biological specimens and test objects using 2.57 nm X rays [Jacobsen 1990]. However, the time spent on processing the resist after a hologram has been recorded and then digitizing the hologram for numerical reconstruction is significant. These complications make this method not feasible for 3D imaging, where several hundred views have to be recorded and processed.

3.1.8 3D in-line holography

The usual conception of holography is that it is a method to yield a complete image of a three-dimensional object. However, this is not correct for X-ray holography. Let us start by considering a two-dimensional object. We can decompose any two-dimensional object into a series of two-dimensional diffraction gratings. As displayed in Figure 3.4 a), we get an intensity maximum when the path difference between two rays is equal to the wavelength. Therefore we can write

$$d(\sin\alpha + \sin\beta) = \lambda, \tag{3.28}$$

where $\alpha > 0$ is the angle of incidence and $\beta > 0$ is the angle of diffraction.

When going to a three-dimensional object, the plane diffraction gratings described by Eq. (3.28) have to be replaced by volume diffraction gratings as shown in Figure 3.4 b). We get maximum intensity when

$$2d\sin\theta = \lambda. \tag{3.29}$$

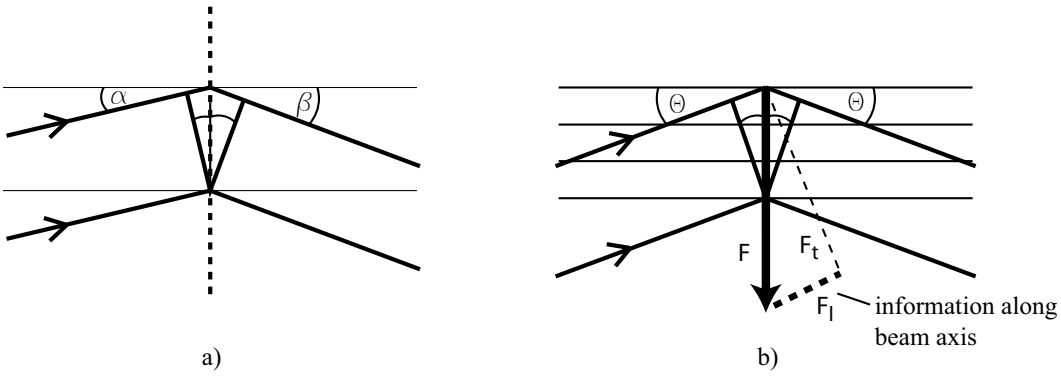

Figure 3.4: a) Plane diffraction grating: intensity maximum when the path difference is equal to the wavelength. b) Volume diffraction grating: intensity maximum when the angles of incidence and reflection are identical.

Here, θ is the angle between the incident wave and the planes and it is also the angle between the outgoing wave and the planes. Eq. (3.29) is also called Bragg's law. We see that it is a much more selective condition, since for a given wavelength λ and diffraction plane spacing d, the angle θ is already determined. In order to get information from all different plane spacings in which the object can be decomposed, one has to change the angle θ. One therefore has to rotate the specimen and record holograms at each rotation angle. By doing this, the longitudinal component F_l of the transfer vector F is being changed, so that the longitudinal information is filled in.

Once all the holograms are recorded, a reconstruction of the object is achieved by numerically backpropagating each hologram intensity throughout the object location (for a discussion of propagating wavefields see Appendix A). All backpropagated 3D wavefields are then added to yield a 3D reconstruction as shown in Figure 3.5.

This method of reconstructing a 3D object also solves the twin-image problem, where the reconstruction of the real image also contains an out-of-focus contribution from the virtual image. In the 3D reconstruction, the contributions from the real image are all in-focus and will add up constructively whereas the out-of-focus contributions from the virtual image will not reinforce each other.

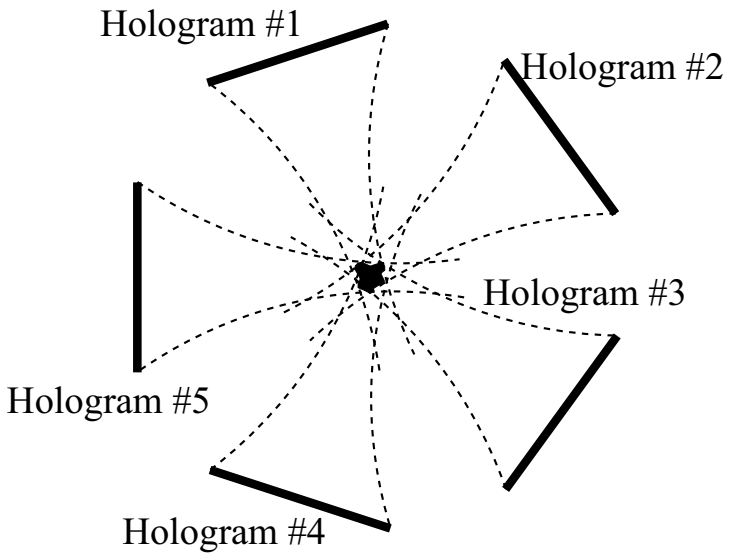

Figure 3.5: Each hologram recorded at different viewing angles is backpropagted throughout the object location. The sum of all backpropagated wavefields yields the reconstruction of the object.

3.2 A brief history of in-line holography

In this section I provide a brief overview of the history of in-line holography. For a more thorough overview, see [Jacobsen 1988].

In the early 1950's, microscopists realized that the achievable resolution in electron microscopes was limited to about 10 Å by the lens. It was Gabor who, in 1947, pointed out that the aberrated image still contained all the information, in amplitude and phase, about the object but in a somewhat encoded form [Gabor 1948] [Gabor 1949]. If this information could be extracted, one could get atomic resolution even from aberrated images. Gabor went on to demonstrate his idea of recording and reconstructing a hologram with visible light.

The first X-ray holograms were reconstructed by El-Sum in 1952 using visible light [El-Sum 1952]. That hologram was actually recorded by Kellström in 1932 using Al Kα X rays ($\lambda = 0.83$ nm). El-Sum used visible light to achieve the reconstruction, therefore introducing aberrations due to the

change in wavelength. After this first reconstruction, many advancements in the recording and reconstruction of X-ray holograms have been made. In 1969, Giles used Be K α X rays ($\lambda = 11.4$ nm) to form a hologram of a 6 μm diameter wire [Giles 1969]. A reconstruction was achieved by using visible laser light. In the early 1970s, Aoki *et al.* used Al Kα X rays ($\lambda = 0.83$ nm) to record Gabor holograms of chemical fibers and red blood cells [Aoki 1974] and reported a resolution of about 4 μm, much better than any previous reconstructions.

Another step forward towards higher resolution came with the advancement of undulators for electron storage rings to provide more coherent photons (see Section 1.2). Howells *et al.* used X rays from a synchrotron ($\lambda = 3.2$ nm) to record Gabor holograms of wires, glass beads, and diatoms [Howells 1984b] [Howells 1984a] [Howells 1985] [Howells 1986] and obtained a resolution of about 1 μm. At this point the photographic film was really the limitation in achieving higher resolution holograms.

Photoresists, such as poly(methymethacrylate) PMMA, proved to overcome the limitations imposed by the photographic film. In 1988 when Joyeux *et al.* used X rays from an undulator ($\lambda = 10$ nm) to record holograms of diatoms, they used a photoresist as the recording medium [Joyeux 1988]. The reported resolution in that experiment was about 0.5 μm. At about the same time, Howells and collaborators also used undulator radiation ($\lambda = 2.4$ nm) and photoresist to record Gabor holograms and reported a resolution of 55 nm [Howells 1987] [Jacobsen 1988]. In their case, holograms were digitized using a transmission electron microscope (TEM) and then numerically reconstructed. Later on Lindaas and collaborators developed an atomic-force microscope (AFM) to read out holograms recorded in photoresist [Lindaas 1994] [Lindaas 1996a]. Using the TEM or AFM to digitize the holograms, instead of doing the reconstruction process with visible light, eliminated aberrations during the reconstruction. However, whereas recording, processing, digitizing and then finally reconstructing numerically works well and provides high resolution, the whole process is very time consuming. Even more, the ultimate goal of a three dimensional reconstruction of an object requires the recording of holograms under several rotation angles. Doing the elaborate reconstruction process for hundreds of views per sample is not really feasible.

In this chapter we will demonstrate the recording of in-line holograms using a charge coupled device (CCD) instead of photoresist. This technique has the potential for immediate numerical reconstruction of the object without the need of digitizing holograms recorded in photoresist, making rapid imaging, needed for 3D imaging, feasible. We should mention at this point, that there has been a proof-of-principle experiment demonstrating in-line holography with a CCD by former graduate student Lindaas and colleagues [Lindaas 1996b].

They successfully recorded holograms of a dried spiral bacteria. However their magnification was estimated to be about 170, resulting in relatively low-resolution holograms. They also did not attempt to reconstruct any of the recorded holograms.

3.3 Experimental realization of Gabor holography

As we have seen in Section 3.1.7, Gabor holograms are limited by the resolution of the detector to record the fine fringes. PMMA was successfully used to record high-resolution holograms. However, to numerically reconstruct the recorded holograms, they had to be digitized using a transmission electron microscope [Jacobsen 1990] or an atomic-force microscope [Lindaas 1996a]. While the actual recording process is very simple and straightforward, digitizing the hologram is very time consuming. When collecting 3D data sets, this method of digitizing the holograms is not feasible to handle the large data sets involved.

The following sections describe how one can collect 3D data sets in a more timely manner using a CCD, providing the possibility of an instant reconstruction on the computer.

3.3.1 Detector

The ideal detector for recording Gabor holograms would have:

- high quantum efficiency to minimize exposure
- low dark noise
- large dynamic range
- good linearity
- fast read-out
- detector resolution matched to the hologram fringes.

A charge-coupled device (CCD) offers all but the last item in the list. Typical CCDs have pixels which are 20 μm by 20 μm and therefore do not match the hologram fringes which require pixel sizes approximately a factor of 1000 smaller.

3.3.2 Experimental geometry

Since we cannot match the detector pixel size to the pixel size of the detector to the hologram, we have to match the hologram to meet the specifications of the detector. In other words: we have to magnify the hologram onto the CCD so that the detector pixel size matches the magnified hologram fringes.

We can achieve such a magnification of the hologram by using a **zone plate as a magnifying lens**. Such an arrangement is shown in Figure 3.6.

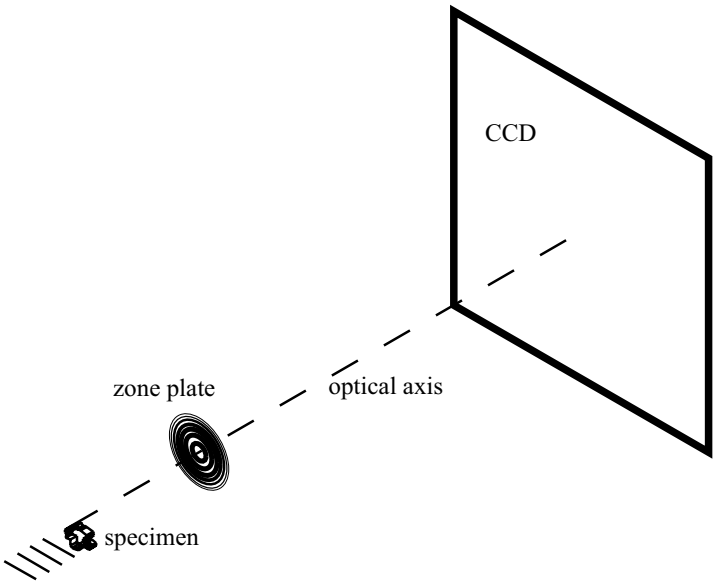

Figure 3.6: Experimental setup for recording in-line holograms on a CCD: a specimen is placed in front of a zone plate and the CCD records the magnified images.

The zone plate acts as a thin lens and therefore following the thin lens equation we can write

$$\frac{1}{f} = \frac{1}{s'} + \frac{1}{s}, \tag{3.30}$$

where s is the object distance and s' is the image distance.

Since the zone plate has positive and negative diffraction orders, we end up with a hologram for each of the orders. In practise only the positive and negative first order are strong enough to give significant contributions (diffraction efficiency of m-th order: $\epsilon_m = \epsilon_1/m^2$). We therefore will neglect all higher orders in the following discussion.

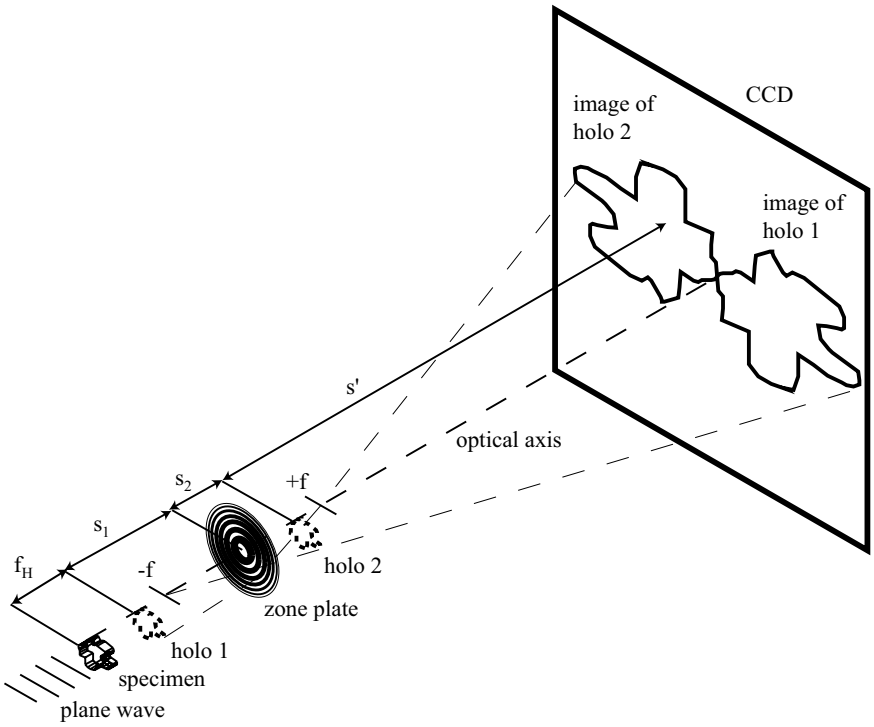

Figure 3.7: A zone plate located behind a specimen magnifies the emerging wavefield onto a CCD. Due to the positive and negative first order of the zone plate, we end up with two wavefields on the detector, emerging from location s_1 and s_2.

Figure 3.7 shows the configuration when only the positive and negative first order of the zone plate is used. The distance s' between the zone plate

and the CCD is usually fixed in an experiment. For a given zone plate with focal length f, we can then calculate the object distance s for the positive and negative first order of the zone plate using the thin lens formula of Eq. (3.30). We have

$$\frac{1}{s} = \frac{1}{f}(1 - \frac{f}{s'}) \tag{3.31}$$

and therefore

$$\begin{aligned} s &= f\frac{1}{1 - f/s'} \\ &= f\sum_{n=0}^{\infty}(\frac{f}{s'})^n \\ &= f(1 + \frac{f}{s'} + (\frac{f}{s'})^2 + ...) \\ &\simeq f(1 + \frac{f}{s'}), \end{aligned} \tag{3.32}$$

where we have used the geometric series since $f/s' \ll 1$ (see example below). Considering that the image due to the positive first-order focus is formed when we use $+f$ in the thin lens equation, we end up with an object distance of

$$s_1 = f(1 + \frac{f}{s}). \tag{3.33}$$

By using $-f$ for the negative first focal order, we get an object distance of

$$s_2 = -f(1 - \frac{f}{s'}). \tag{3.34}$$

From the above we see that the optical wavefields at two different planes are transferred to the detector: one from the distance s_1 upstream of the zone plate, and one from the distance s_2 which is located downstream of the zone plate. Each wavefield is a different in-line hologram of the object, provided that the object is located at a distance larger than s_1 upstream of the zone plate.

As an example we consider a zone plate with focal length $f = 1$ mm and sample to detector distance of $s = 1$ m and get $s_1 = 1.001$ mm and $s_2 = -0.999$ mm. The distance f_H in Figure 3.6 is the hologram recording distance given by Eq. (3.13). This distance would have been used if the hologram were to be recorded with a high resolution detector such as PMMA.

If the axis of the specimen and the zone plate do not coincide, the holograms arising from the positive and negative order of the zone plate will be separated on the CCD camera as shown in Figure 3.7.

Zone plate magnification The magnification M of each of the different waves at the CCD is given by

$$M = \frac{s}{s'}. \tag{3.35}$$

Inserting s' from the lens equations gives

$$\begin{aligned} M &= \frac{s}{f} \cdot \frac{1}{1-(-\frac{f}{s})} \\ &\simeq \frac{s}{f}(1-\frac{f}{s}), \end{aligned} \tag{3.36}$$

where we have used the geometric series again. When we insert the values for the different focal lengths ($\pm f$), we end up with

$$\begin{aligned} M_1 &= \frac{s}{s_1} \\ &= \frac{s}{f} - 1 \end{aligned} \tag{3.37}$$

and

$$\begin{aligned} M_2 &= \frac{s}{s_2} \\ &= -\frac{s}{f} - 1 \end{aligned} \tag{3.38}$$

for the two magnifications due to the positive and negative first-order of the zone plate.

As an example we choose $f = 1$ mm and $s = 1$ m and get $M_1 = 999$ and $M_2 = -1001$. Such a magnification basically takes the 20 μm CCD pixel size down to 20 nm hologram or object pixel size, which we are trying to record.

3.4 First holography data set

3.4.1 Experimental setup

Experiments using a zone plate and a CCD to record in-line X-ray holograms were carried out the NSLS at beamline X1A (see Section 2.2). The zone plate used had no central stop so that the object could be placed close to the optical axis. Such an arrangement made it possible to simultaneously record the image of the far-field and near-field hologram on the CCD. Table

Energy	390 eV
Zone plate diameter	200 μm
Outermost zone width	80 nm
Focal length	5030 μm
Zone plate material	Ni
Distance zone plate to CCD	0.9 m
Magnification	180

Table 3.1: Summary of the experimental parameters used in the first holography experiment.

3.1 summarizes the experimental parameters for the initial experiment. The parameters of the custom zone plate were chosen to give a relatively low magnification in the first experiments. This made the experimental setup easier and was also not too demanding with the state of the zone plate production process available at that time.

3.4.2 The data and analysis

One of the samples consisted of 1 μm diameter latex spheres (Ted Pella, PO Box 2318, Redding, Ca 96099, part ♯610-38. 0.1% solids lot ♯02010). A small amount of the sphere solution was further diluted with distilled water. A drop of the solution was then placed onto a silicon nitride membrane. After the drop had dried on the membrane, the sample was inserted into the experimental chamber for data acquisition. Figure 3.8 shows a hologram of the collection of 1 μm diameter latex spheres. The left part of the CCD image shows the almost in-focus image formed by the positive first order focus. The right part shows the far-field hologram formed by the negative first order focus. To protect the CCD from the intense straight x-ray beam a wire was used as a beamstop. We note here that the sample was prepared at the edge of a SiN3 window so that a clear separation of the positive and negative order image was achieved.

The recorded image clearly shows strong fringes around the optical axis. The appearance of those fringes makes it difficult to collect high quality data and further complicates the reconstruction.

In order to understand the cause of the fringes, the latex spheres were replaced by a 20 μm diameter pinhole in a second experiment. In addition, the

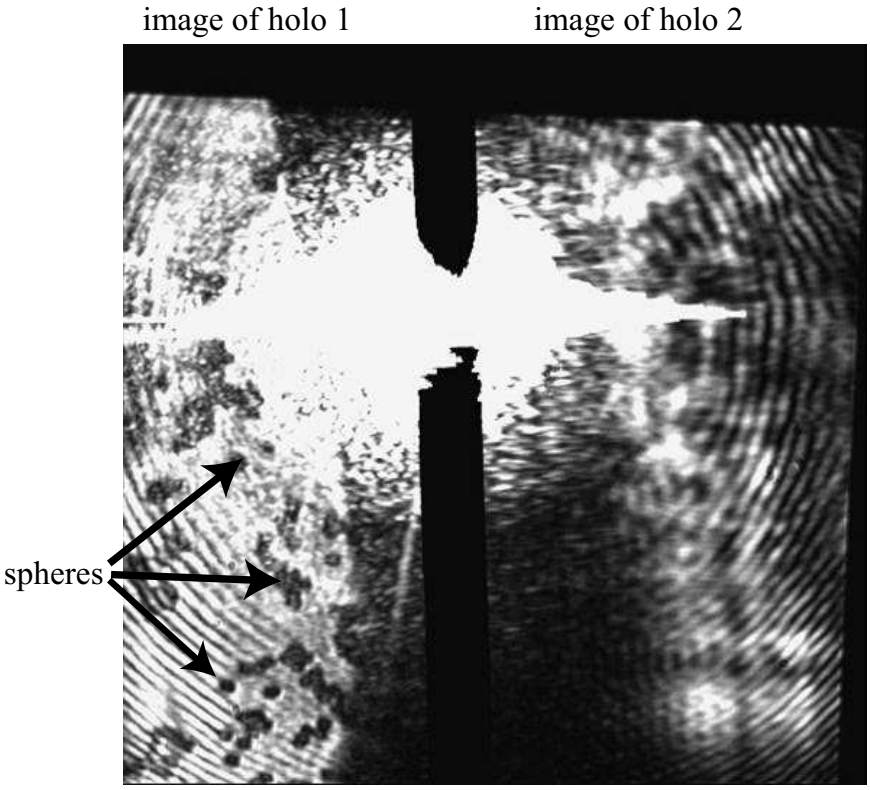

Figure 3.8: CCD image showing the holograms of 1 μm diameter latex spheres. Shown on the left side is the -almost in-focus - hologram produced produced by the positive first-order focus. The right side shows the hologram produced by the negative first-order focus of the zone plate. Concentric fringes around the central beam position are clearly visible.

CCD camera was positioned slightly off-axis to allow for larger offsets between the pinhole (in this case the sample) and the zone plate. The drawback of that arrangement is that either the positive or the negative first-order of the zone plate can be recorded on the CCD, but not both simultaneously.

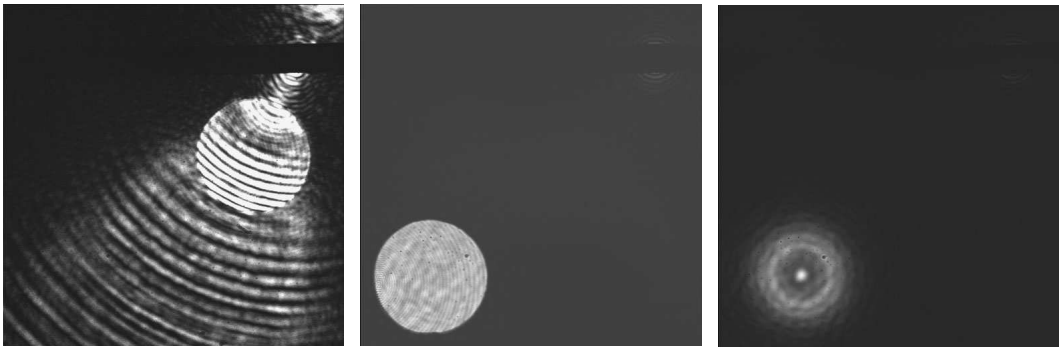

Figure 3.9: Mapping the zone plate - a pinhole is used as the object. a): The pinhole is closer to the optical axis and strong fringes are seen. b): The pinhole is placed further off-axis and the fringes disappear. c:) Same image as b) but formed using the negative first-order of the zone plate.

Figure 3.9 a) shows a recorded in-focus image of the pinhole using the positive first-order focus of the zone plate. Fringes across the image of the pinhole are visible again. However, as the zone plate is moved farther off-axis the image becomes much cleaner (Figure 3.9 b)).

The image formed by the negative first-order focus is located on the other side of the optical axis due to the large off-axis position. However, moving the zone plate to the opposite side of the optical axis puts the image from the negative first-order focus on the detector. Figure 3.9 c) shows the image from the negative first order.

3.4.3 IDL simulations

In order to understand the cause of the fringes, we simulated the experiment on a computer using the Interactive Data Language (IDL). Assuming

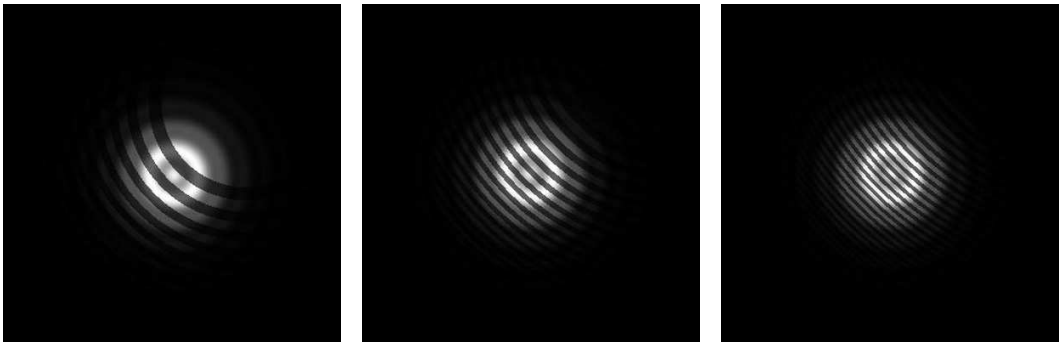

a) b) c)

Figure 3.10: The propagated wavefield emerging from the pinhole is incident on a zone plate which is shifted off-axis.

plane wave illumination (constant phase across the pinhole), the program simulates a pinhole and propagates the wavefield by the distance between the object and the zone plate. A zone plate with absorption and phase shift is generated and shifted by a variable distance to simulate the off-axis configuration. Absorption and phase shift due to the zone plate is applied to the wavefield (see Figure 3.10) and the Fourier transform is taken to simulate the image at the detector plane following Goodman [Goodman 1968].

The simulated data images are shown in Figure 3.11 for three different zone plate offsets. They correctly simulate the straight beam together with the images of the pinhole due to the positive and negative first and third order of the zone plate.

The images also reproduce the fringes that are present in the experimental data. It can be verified that the fringes become less visible as the zone plate is moved farther off-axis. To display the fringes more clearly, Figure 3.12 displays a magnified image of the pinhole produced by the first order of the zone plate. Such an image corresponds to an image that was recorded experimentally as described in the previous section.

We believe that the fringes are caused by the fact that the coarseness of the innermost zones provides a poor local approximation to the desired continuous phase function of a lens. We have therefore attempted to move the zone plate farther away from the optical axis so as to use in the beam path the much greater number of finer zones at larger zone plate radii. Experimental results

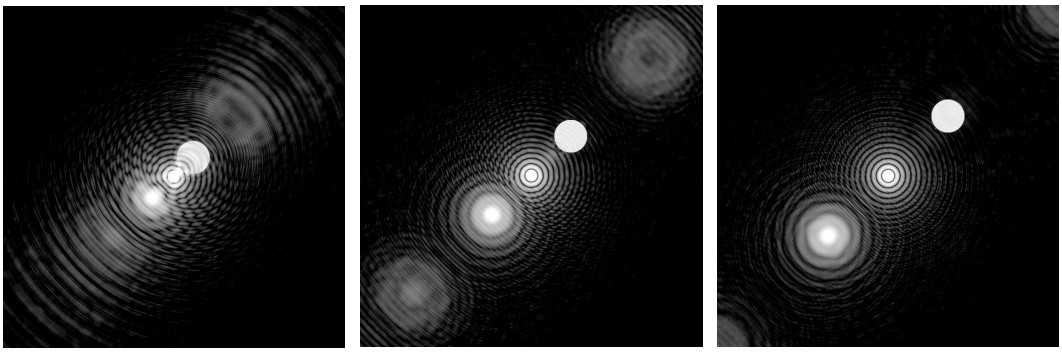

a) b) c)

Figure 3.11: Simulated CCD images for different zone plate shifts (see Figure 3.10). All images show the image produced by the positive and negative first- and third- order of the zone plate.

a) b) c)

Figure 3.12: Magnified view of the positive first-order image for different zone plate to pinhole offsets. The fringes disappear as the offset is increased. The simulated images match well with the experimental data.

with this modified setup are discussed in the following section.

3.5 Second holography data set

3.5.1 The modified experimental setup

Due the experience from the first experiment and the computer simulations of the experiment, the setup was modified to accommodate a zone plate with a central stop. This decision forced us to place the object further off-axis (see Figure 3.13), resulting in a further spatial separation of the two holograms at the detector plane.

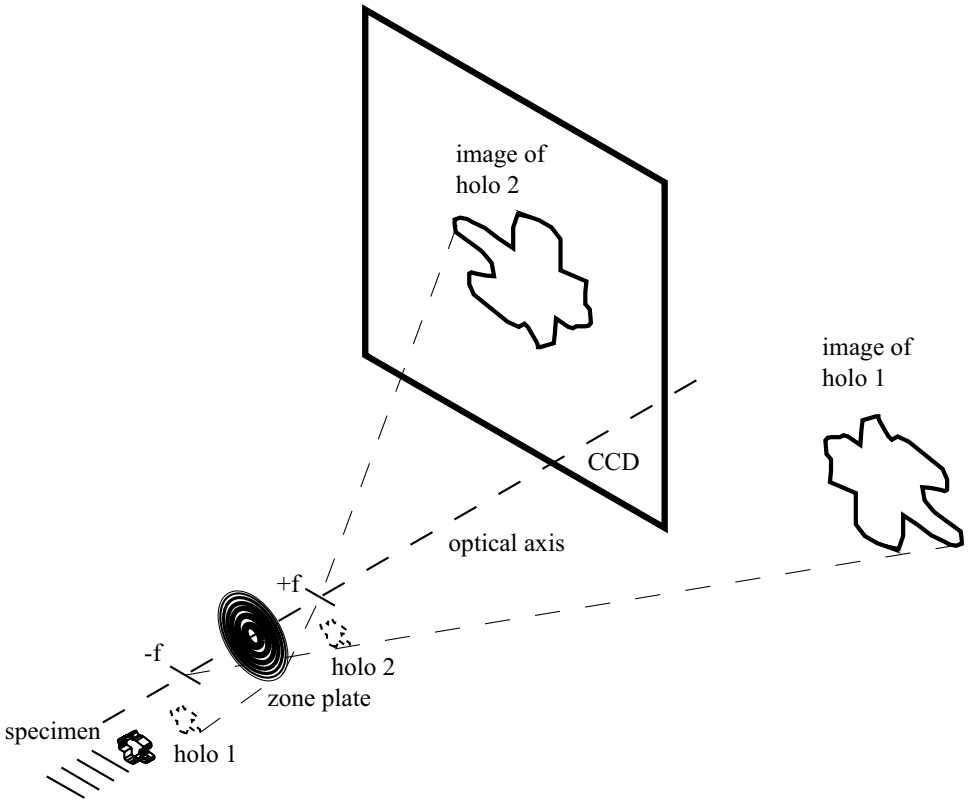

Figure 3.13: Modified experimental setup for recording in-line holograms using a CCD. The zone plate is placed further off-axis resulting in a larger separation of the positive and negative first-order image of the zone plate.

energy	395 eV
zone plate diameter	160 μm
outermost zone width	45 nm
focal length	2.2 mm
zone plate material	Ni
distance zone plate to CCD	0.9 m

Table 3.2: Summary of the experimental parameters used in the modified holography experiment.

The separation of the two holograms at the detector plane was at least 32 mm. It was therefore not possible to record both holograms at the same time anymore. The CCD also had to move off-axis in order to be able to record one of the holograms.

3.5.2 Data collection

Holograms of the 1 μm diameter latex spheres were recorded again together with holograms of a fabricated test object. The test object was a 3 μm diameter gold dot with a thickness of 90 nm. The gold dot was prepared on a silicon nitride membrane by Aaron Stein. Figure 3.14 a) shows a hologram of the latex spheres and Figure 3.14 b) shows a hologram of the gold dot.

The holograms were recorded by bringing the sample into the focus plane of the zone plate and then defocusing the object by certain distance. Several holograms were recorded at different propagation distances and used in the reconstruction.

3.5.3 Reconstruction

The exact defocus distance is very important in a reconstruction. During the alignment procedure an almost in-focus image was recorded before the sample was translated along the beam axis to record the hologram. From this defocus distance, one can get a rough estimate, but a more precise knowledge of the focus distance is needed. Therefore each recorded hologram was back-propagated to several positions along the optical axis, resulting in a complex wavefield for each propagation distance. A line out of each of the backprop-

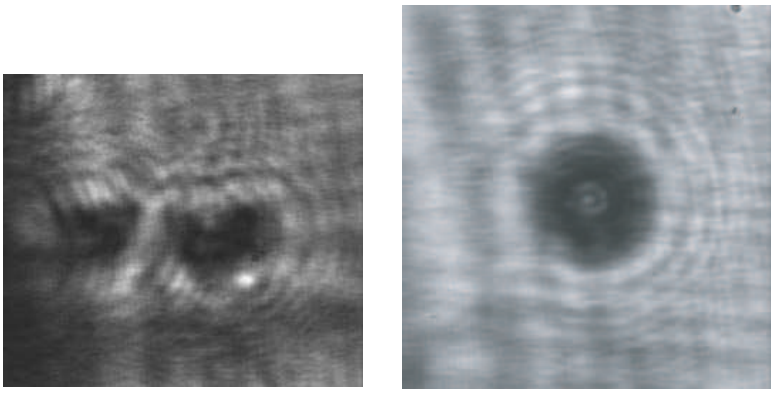

Figure 3.14: a) Hologram of a collection of 1 μm diameter latex spheres. b) Hologram of the 3 μm diameter gold dot.

agated wavefields was then taken and plotted as a function of propagation distance. Figure 3.15 shows a typical focus scan for the latex spheres.

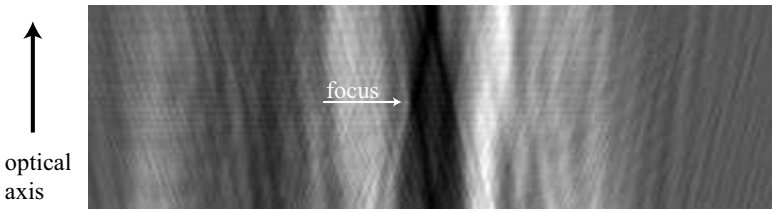

Figure 3.15: The hologram is backpropagated throughout the specimen region. A line of each resulting wavefield is then taken and displayed against the backpropagation distance, resulting in a focus scan.

By clicking on the line that seemed to best show the narrow neck of an hourglass-shaped pattern, the exact focus distance was determined. This procedure was then repeated for each recorded hologram to find the exact focus position.

To yield the final amplitude and phase reconstruction of the latex spheres (Figure 3.16) and the gold dot (Figure 3.17), several backpropagated holograms were added. This additional step of adding several backpropagated holograms is not necessary, but helped a little bit in suppressing noise, since some of the artifacts from each out-of-focus twin image cancel each other.

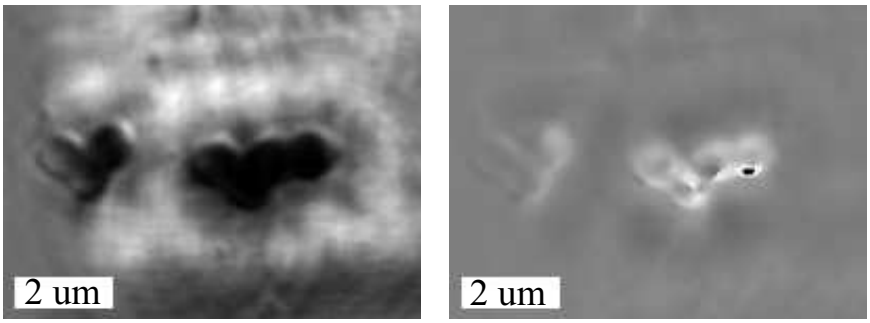

Figure 3.16: Amplitude and phase reconstruction of a 1 μm diameter latex spheres. The reconstruction was obtained by backpropagating the holograms, therefore reconstructing the complex wavefield.

We can compare the expected transmission of the gold with the transmission from the reconstructed image. With a 90 nm gold thickness of the gold dot, we would expect a transmission of about 7 %. In our reconstruction we determine a transmission of about 3 %, which is in reasonable agreement with the expected transmission.

3.6 Discussion and the future of in-line holography

We have successfully demonstrated in-line holography using a CCD to record the holograms. The technique allows for rapid reconstructions of the holograms, which is required for three-dimensional specimen reconstructions. The obtained reconstruction agrees fairly well with an expected reconstruction.

However, the resolution demonstrated is far from the resolution achieved in present-day conventional X-ray microscopes. One of the limiting factors

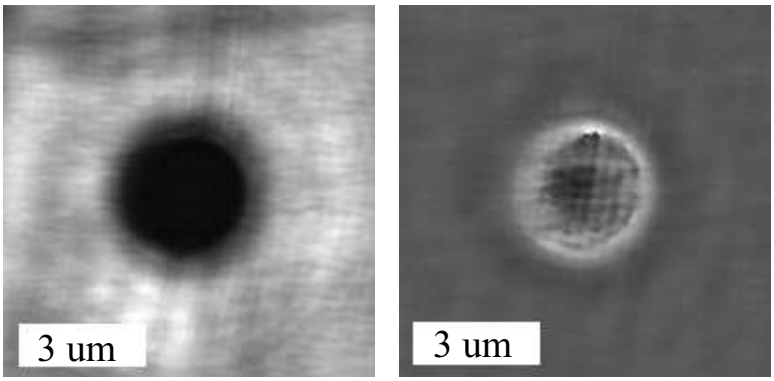

Figure 3.17: Amplitude and phase reconstruction of a 3 μm diameter gold dot. The reconstruction was obtained by backpropagating the holograms, therefore reconstructing the complex wavefield.

in achieving higher resolution is that the experiment is extremely sensitive to vibrations, which was limiting the resolution in our experiments. The current setup would have to be upgraded with higher quality stages to minimize the vibrations. Furthermore, the coherence requirements are very high and appropriate sources are needed that can provide the necessary coherence and still provide a high photon flux. Another shortcoming of the technique (this is also true for present-day conventional X-ray microscopes) is the need for a high-resolution zone plate. Today's best zone plates have 20 nm outermost zone widths, therefore limiting the achievable resolution. Zone plates are also relatively low efficient optics and since they are behind the specimen, the dose on the specimen has to be increased to make up for the low efficiency. Yet another limitation of in-line holography is the artifacts from the twin image. Even though they can be reduced when combining holograms recorded at different viewing angles, they still degrade the reconstruction quality. The experimental chamber is now permanently installed at the ALS 9.0.1 beamline and most of its operation is done in lensless diffraction imaging mode (see Chapter 4). To switch to high-resolution holography, part of the beamline has to reconfigured to provide a larger coherence area. An extension tube has to be inserted between the experimental chamber and the CCD section, to achieve a high magnification. Since such a rearrangement together with the needed realignment of the experimental apparatus is very time consuming, we decided to not further pursue the in-line holography experiments, but rather

invest more time on the more promising lensless diffraction imaging technique. However, as will be described in the next chapter, a low-resolution holography setup is valuable in supplementing diffraction imaging.

Chapter 4

Diffraction imaging

This chapter discusses diffraction imaging as an alternative technique for high-resolution 3D imaging. We start with a brief history and an overview of the principles of diffraction imaging. An overview of the reconstruction algorithms is given together with a discussion of the algorithm used in this dissertation. We show experimental data taken at the ALS 9.0.1 beamline and show that the imaging setup as described in Chapter 3 is well suited to help overcome some of the difficulties of diffraction imaging. Finally, 2D and 3D reconstructions of a prepared specimen are presented. We end with a discussion and an outlook for future developments.

4.1 Fundamentals of diffraction imaging

We have seen in Section 1.1 that an object's electron density will give rise to a complex transmittance function. If, for example, a plane wave is incident on the specimen, the wavefield will be modified by the specimen's complex transmittance. The emerging complex wavefield therefore has all the information necessary to retrieve an image of the object. This can be done by mixing the wavefield with a reference wavefield to form a hologram (see Section 3). Lenses can also be used to recover this information as is done in conventional microscopy. In diffraction imaging, the object is retrieved from a recording of the intensity of the Fourier transform of the complex exit wavefield; that is the far-field diffraction pattern. However, since an intensity measurement only records the magnitude of the Fourier transform but not its phase, iterative algorithms have to be employed to recover the object. In the following, we discuss the details of recording and reconstructing diffraction patterns.

4.1.1 The phase problem

If an object's electron density function is represented by $f_{(\vec{x})}$, then its Fourier transform $F_{(\vec{k})}$ can be written as

$$F_{(\vec{k})} = \int_{-\infty}^{\infty} f_{(\vec{x})} e^{-i2\pi\vec{k}\cdot\vec{x}} d\vec{x} \tag{4.1}$$

$$= \sum_{\vec{x}=0}^{N-1} f_{(\vec{x})} e^{-i2\pi\vec{k}\cdot\vec{x}/N}, \tag{4.2}$$

where we have changed from a continuous to a discrete sampling and x and k run from 0, 1, ..., N-1 [Fienup 1982]. The inverse is given by

$$f_{(\vec{x})} = \frac{1}{N^2} \sum_{\vec{x}=0}^{N-1} F_{(\vec{k})} e^{i2\pi\vec{k}\cdot\vec{x}/N}. \tag{4.3}$$

$f_{(\vec{x})}$ can be expressed as a complex function

$$f_{(\vec{x})} = |f_{(\vec{x})}| e^{i\phi_{(\vec{x})}}. \tag{4.4}$$

In an experiment only the magnitude of the Fourier transform can be measured and the **phase is lost**. We can write

$$|F_{(\vec{k})}| = |\sum_{\vec{x}=0}^{N-1} f_{(\vec{x})} e^{-i2\pi\vec{k}\cdot\vec{x}/N}|. \tag{4.5}$$

We see that it is no longer possible to retrieve the object's electron density function by just taking the Fourier transform of the measured diffraction magnitudes. The following sections discuss the underlying theory of the ability to recover the phase from a single intensity measurement.

4.1.2 Nyquist-Shannon sampling theorem

In 1928, Harry Nyquist [Nyquist 1928] formulated a theorem in the field of information theory which was later proved by Claude E. Shannon in 1949 [Shannon 1949]. This theorem had a great impact on the development of information technology, particularly in telecommunications. The theorem (illustrated in Figure 4.1) states that when a band-limited signal is converted from analog to digital (e.g., the signal is sampled at discrete intervals), the **sampling frequency has to be at least twice the highest frequency of the input signal** in order to be able to completely reconstruct the input signal from the sampled version. If a sampling frequency smaller than twice

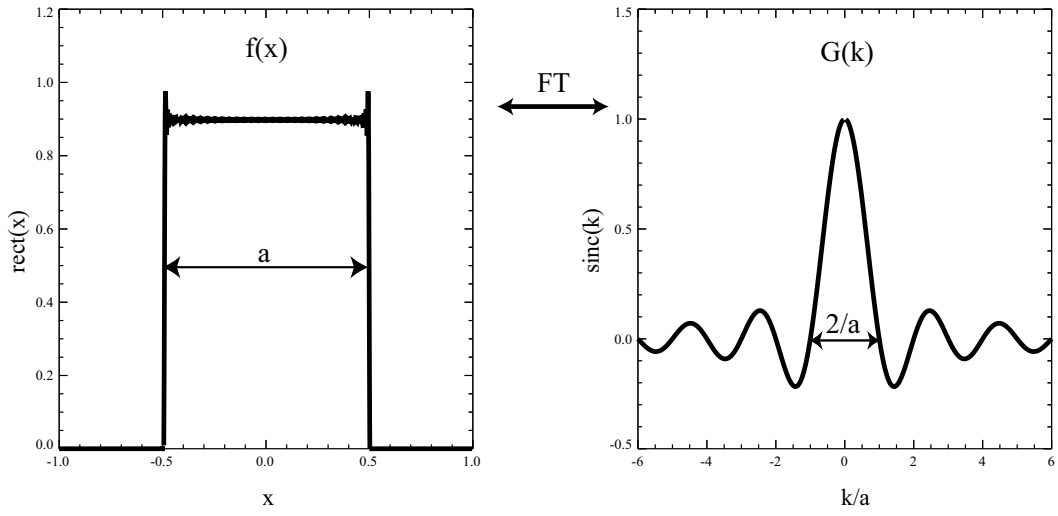

Figure 4.1: Example of the Nyquist-Shannon sampling theorem: the band-limited function $f_{(x)}$ can be completely recovered if its Fourier transform $F_{(k)}$ is measured at the points $k = 0, \pm 1/a, \pm 2/a$, and so on.

the highest frequency is used, frequencies in the original signal that are above

half the sampling rate will be aliased (the high-frequency components are replaced/aliased with low-frequency components and therefore not recorded correctly). To understand the theorem we consider the following function as indicated by Shannon [Shannon 1949]:

"If a function $f_{(x)}$ is known to vanish outside the points $x = \pm a/2$, then its Fourier transform $F_{(k)}$ is completely specified by the values which it assumes at the points $k = 0, \pm 1/a, \pm 2/a, ...$".

In this case, the sampling frequency of $1/a$ is also called the Shannon or Nyquist sampling frequency.

4.1.3 Implications of the Nyquist-Shannon sampling theorem on diffraction imaging

In 1952, Sayre pointed out that when dealing with the intensity $|F_{(k)}|^2$ instead of $F_{(k)}$, it would be sufficient to sample $|F_{(k)}|^2$ at half the sampling interval [Sayre 1952] as given by the Nyquist-Shannon sampling theorem.

For an object of width a and a distance z away from the detection plane, we can write for the highest frequency in a diffraction pattern

$$f_{\max} = \frac{1}{a} \cdot \lambda z. \tag{4.6}$$

The pattern would be sampled at the Nyquist limit if a sampling interval

$$\begin{aligned} f_{\mathrm{NS}} &= \frac{1}{2} f_{\max} \\ &= \frac{1}{2a} \cdot \lambda z \end{aligned} \tag{4.7}$$

were to be used. A diffraction pattern sampled at at least f_{NS} would contain all the information about the diffracting object so that the object could be completely recovered.

Let us return to the function $f_{(x)}$ introduced in the previous section. In an experiment, we measure $|F_{(k)}|^2$, which is related to the autocorrelation of $f_{(x)}$

$$|F_{(k)}|^2 = \mathcal{F}\{f_{(x)} \star f_{(x)}\}, \tag{4.8}$$

where $\star$ stands for a convolution and $\mathcal{F}\{\}$ is the Fourier transform operator (see Appendix D). Figure 4.2 shows the triangle function $f_{(x)} \star f_{(x)}$ due to the rectangle function $f_{(x)}$.

It is important to realize that the autocorrelation $f_{(x)} \star f_{(x)}$ has exactly twice the dimension of $f_{(x)}$. Therefore, if one makes sure that the diffraction pattern $|F_{(k)}|^2$ is exactly Shannon sampled, then $f_{(x)} \star f_{(x)}$ is also exactly

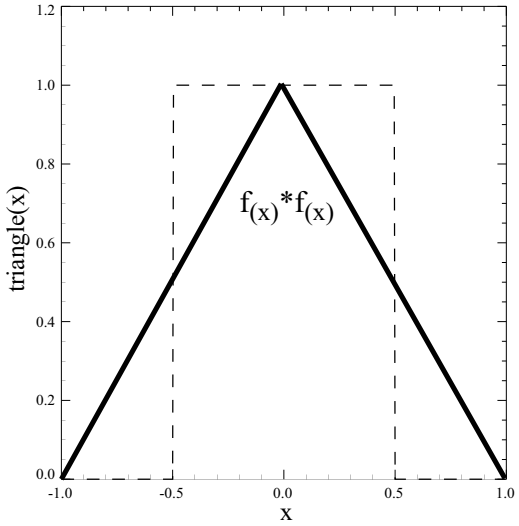

Figure 4.2: The autocorrelation of $f_{(x)}$ is twice the size of $f_{(x)}$. When the autocorrelation is correctly sampled and used to retrieve $f_{(x)}$ this can be used to apply zero-padding.

Shannon sampled. If we now use such a diffraction pattern to reconstruct the object $f_{(x)}$, then the transform of $|F_{(k)}|$ is exactly oversampled by a factor of two. That means that the recovered function $f_{(x)}$ is zero-padded, as indicated in Figure 4.2. This zero-padding is used as a support constraint in the reconstruction algorithms described in Section 4.3.

We can also go back to Eq. (4.2) and increase the sampling frequency by a factor of two

$$F_{(\vec{k})} = \sum_{\vec{x}=0}^{N-1} f_{(\vec{x})} e^{-i2\pi\vec{k}\cdot\vec{x}/2N}. \tag{4.9}$$

By doing so, we have effectively increased the number of points in the object function, by including empty space. The function $f_{(\vec{x})}$ is therefore zero-padded. Figure 4.3 demonstrates the effect of sampling a diffraction pattern at twice the Shannon sampling rate.

The following sections will describe experiments that make use of the finite support of a scattering object to reconstruct the object.

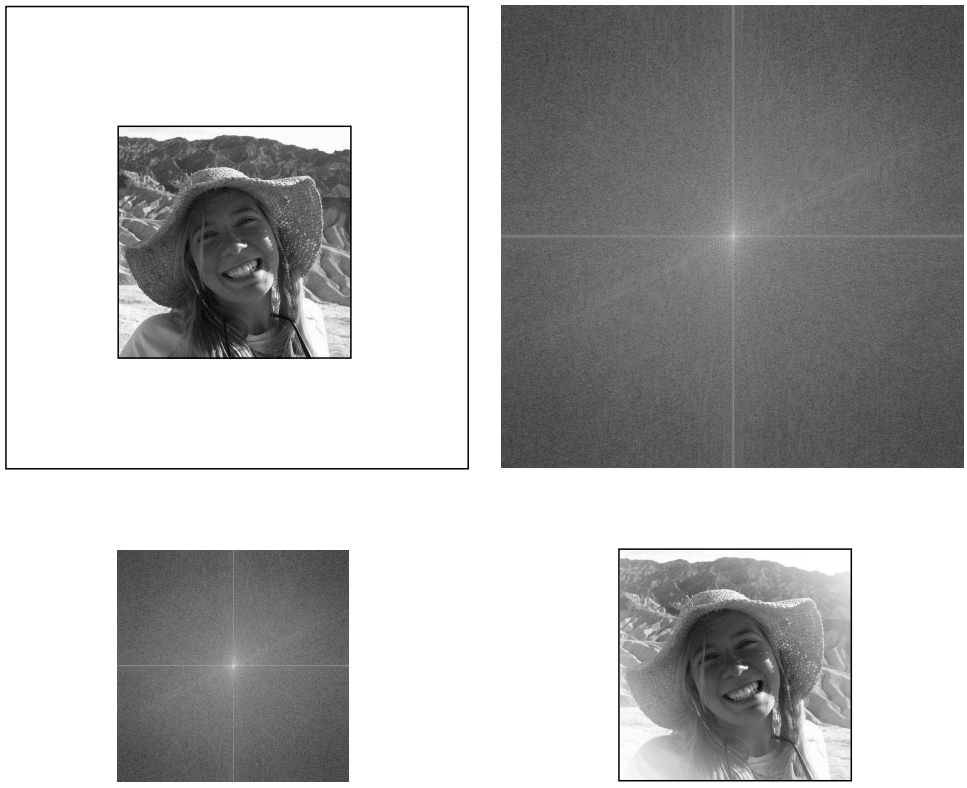

Figure 4.3: Demonstration of sampling the diffraction pattern: Shown is the object padded in a larger area (left, top) and the magnitude of its Fourier transform (right, top). The Fourier transform is then remapped into an array half its size (left, bottom) and the inverse Fourier transform of the resulting array is shown (right, bottom). The resulting object lacks the white area surrounding the object.
Alternatively one can also start with the object (right, bottom) and record the diffraction pattern with a larger array, to then recover the original object padded in the larger array after taking the inverse Fourier transform.

4.1.4 Resolution in a diffraction pattern

The maximum resolution contained in a diffraction pattern is given by the maximum diffraction angle Θ that can be recorded on the detector (see Figure 4.4). From the grating equation with period $2d$ the diffraction angle can be

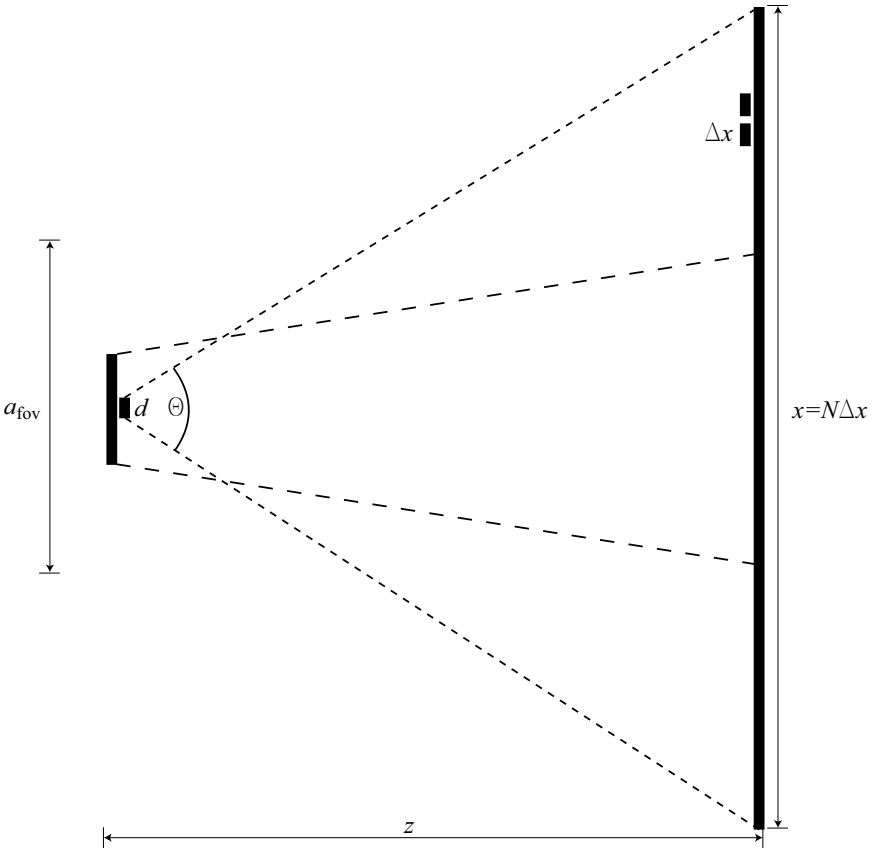

Figure 4.4: Schematic of the diffraction geometry: The sample of width a contains resolution elements of width d. The diffraction pattern is recorded on a detector with pixel size Δx, located a distance z downstream of the sample.

written as

$$\sin\frac{\Theta}{2} \approx \frac{\Theta}{2} = \frac{\lambda}{2d}$$

$$\Rightarrow \Theta = \frac{\lambda}{d}. \tag{4.10}$$

If we now consider the separation distance z of the detector from the diffracting object, we have for small angles

$$\begin{aligned} \tan\frac{\Theta}{2} &\approx \frac{\Theta}{2} = \frac{x/2}{z} \\ \Rightarrow \Theta &= \frac{x}{z}, \end{aligned} \tag{4.11}$$

where x is half of the detector length. Substituting this result into Eq. (4.10) yields

$$d = \frac{\lambda z}{x} \tag{4.12}$$

$$= \frac{\lambda z}{N\Delta x}, \tag{4.13}$$

where we have used the number of detector pixels N and the width of the detector pixels Δx. As an example, for $\lambda = 1.65$ nm, $z = 160$ mm, $N = 1300$, and $\Delta x = 20$ μm, which are typical values for the experiment described in this chapter, we get a theoretical maximum resolution of $d = 10$ nm. In the following we will sometimes use the spatial frequency, defined as $1/2d$, when we talk about the information content in a diffraction pattern. We refer to d as the resolution or resolution element.

4.1.5 Oversampling ratio

In the example above, we have used the number of pixels that we have available in our experiment ($N = 1300$). However, we have not yet considered how many pixels we would really need across the distance of ($x = N\Delta x$). In other words, we might be oversampling or undersampling the diffraction pattern. Of course, as we have seen in Section 4.1.3, we want to sample the diffraction pattern at at least twice the Shannon frequency. We can start by calculating the detector pixel size $\Delta x_{\text{Shannon}}$ needed to record the diffraction pattern at the Shannon frequency for the intensity. From Eq. (4.13) we write

$$\Delta x_{\text{Shannon}} = \frac{\lambda z}{2a}. \tag{4.14}$$

To have sufficient sampling, we require that our detector pixels Δx are not larger than $\Delta x_{\text{Shannon}}$. It is useful to introduce a so-called oversampling ratio

[Miao 1998], which we can define as

$$\sigma_{\text{os}} = \frac{\Delta x_{\text{Shannon}}}{\Delta x} \tag{4.15}$$

$$= \frac{\lambda z}{2a\Delta x}. \tag{4.16}$$

Using again the experimental values of $\lambda = 1.65$ nm, $z = 160$ mm, $\Delta x = 20$ μm and a sample width of $a = 2$ μm, we get $\sigma_{\text{os}} = 3.3$. Note that this definition of the oversampling ratio implies a value of $\sigma_{\text{os}} \geq 1$ to reconstruct a scattering object from its measured diffraction intensity.

4.1.6 Field of view

The field of view can be calculated by again taking Eq. (4.13):

$$a_{\text{fov}} = \frac{\lambda z}{\Delta x}. \tag{4.17}$$

For $\lambda = 1.65$ nm, $z = 160$ mm and $\Delta x = 20$ μm, we get a field of view of $a_{\text{fov}} = 13$ μm and the object size must be no larger than $a_{\text{fov}}/\sigma_{\text{os}}$.

4.1.7 Coherence requirements in diffraction imaging

Spatial coherence. The required spatial coherence can be calculated in the same way as in Section 3.1.6 using the van Cittert-Zernike theorem expressed by Eq. (3.26). We have been using a pinhole of diameter $d_{\text{ph}} = 5$ μm as the beam defining aperture. With the pinhole placed a distance $l = 1$ cm upstream of the specimen, we expect a transverse coherence over a distance

$$d_{\text{coh}} = 0.31\frac{\lambda l}{d_{\text{ph}}}. \tag{4.18}$$

As an example, for $\lambda = 1.65$ nm, $l = 25$ mm, and $d_{\text{ph}} = 5$ μm we get $d_{\text{coh}} = 10.3$ μm. The chosen coherence width is well matched to the size of the scattering object, which was about 2 μm.

Temporal coherence. Yun [Yun 1987a] derived a detailed expression for the required monochromaticity and divergence of the illuminating beam. For a non-diverging beam, the required energy resolution is given by

$$\frac{\lambda}{\Delta\lambda} \geq \frac{a}{\lambda}\sqrt{2(1-\cos\theta)}. \tag{4.19}$$

Here, θ is the diffraction angle and a is the size of the scattering object. If we are interested in a certain spatial resolution in the diffraction pattern, we can express the diffraction angle in terms of the desired resolution element d by using Eq. (4.10) and write

$$\begin{aligned} \frac{\lambda}{\Delta\lambda} &\geq \frac{a}{\lambda}\sqrt{2(1-\cos\frac{\lambda}{d})} \\ &\approx \frac{a}{\lambda}\sqrt{2(1-1+\frac{\lambda^2}{2d^2}-...)} \\ &\approx \frac{a}{d}, \end{aligned} \tag{4.20}$$

where we have used the small angle approximation. As an example, we consider $\lambda = 1.65$ nm, an object of size $a = 2$ μm and a resolution element $d = 10$ nm and get $\frac{\lambda}{\Delta\lambda} \geq 200$. This is a relatively low monochromaticity requirement and is well matched by the zone plate monochromator used at the ALS beamline 9.0.1 (see Section 2.3.1 for details).

Let us now compare this result to the number of required detector pixels N. From Eq. (4.13) we find

$$\begin{aligned} N &= \frac{\lambda z}{d\Delta x} \\ &= \frac{a}{d}, \end{aligned} \tag{4.21}$$

where we have used $\Delta x = \lambda z/d$. Therefore the number of detector pixels corresponds to the required monochromaticity found in Eq. (4.20). We note here, that for a correct Shannon sampling of the diffraction intensity, the detector pixel size is given by Eq. (4.14), which is exactly half the pixel size that we have used to derive Eq. (4.21). Changing the pixel size to the correct Shannon pixel size has the same effect of changing the object to be twice its size ($a \rightarrow 2a$), which corresponds to the object and its support needed for reconstruction of the object from the intensity measurement. Either way, the required monochromaticity is then just double the calculated monochromaticity!

Beam divergence Another constraint for recording the diffraction pattern is on the beam divergence. The formula derived by Yun [Yun 1987a] for a monochromatic but divergent beam is

$$\Delta\theta_0 \leq \frac{\lambda}{a}. \tag{4.22}$$

In our experiment, $\lambda = 1.65$ nm and the object size is $a = 2$ μm and we get the requirement on the beam divergence $\Delta\theta_0 \leq 8.3 \cdot 10^{-4}$ rad. The experimental divergence of the beam is mainly due to the zone plate monochromator. With the zone plate parameters given in Table 2.1, we can write $\Delta\theta_{\text{exp}} \leq \frac{\text{size of zone plate window}}{\text{focal length}} = 4.7 \cdot 10^{-4}$ rad. Therefore the zone plate monochromator is well matched to the divergence requirements.

From the expected experimental divergence, we can calculate the diameter of the illumination a distance s downstream of the monochromator pinhole of diameter d. We get

$$a_{\text{max}} \quad = \quad d_{\text{Ph}} + s\Delta\theta_0. \tag{4.23}$$

Using $d_{\text{Ph}} = 5$ μm, s=10 mm and $\Delta\theta_0 = 4.7 \cdot 10^{-4}$ rad, we calculate $a_{\text{max}} = 9.7$ μm. Comparing this result to the field of view calculated in Eq. (4.17) as $a_{\text{fov}} = 13$ μm, we can see that the illuminating wavefield does not completely fill out the whole area.

4.2 A brief history of diffraction imaging

In 1980, Sayre explicitly proposed to extend the methodology of X-ray crystallography to imaging of non-crystalline objects [Sayre 1980]. Even his work in 1952 already implies such an extension to non-crystalline objects [Sayre 1952]. In the early 1980's, Yun *et al.* started their first experiments at the then newly-built National Synchrotron Light Source (NSLS) at Brookhaven National Laboratory. They were able to collect diffraction patterns from a single diatom (microscopic unicellular marine or freshwater colonial alga having cell walls impregnated with silica) using 3.2 nm X rays. The patterns had diffraction information out to about 40 nm resolution [Yun 1987b]. The resolution estimate was obtained by determining the maximum angular extent of the diffraction pattern that had discernable signal (see Eq. (4.13) for more details). Further improvements were made within the next years when Sayre *et al.* succeeded in recording diffraction patterns of various objects using 1.8 nm X rays at the NSLS. They recorded diffraction patterns of an air-dried bull sperm tail, *minutocellus polymorphis* (marine plankton), and a single myofibril of a honeybee flight muscle. Visual inspection of the diffraction data indicated that data was recorded that corresponds to a resolution ranging from 30 nm to 14 nm [Sayre 1991, Sayre 1998]. However, no reconstruction was attempted. In 1998, Sayre *et al.* took the important step of combining the Fienup-type iterative algorithm [Fienup 1982] with the idea of reconstructing the diffraction pattern. In 1999, Miao *et al.* reported the first successful reconstruction of a microfabricated object [Miao 1999]. In their work they achieved a reconstruction of an array of gold dots at a resolution of ~ 75 nm using 1.7 nm X rays. Their success sparked a number of efforts at different locations and led to more applications of the technique by Miao *et al.* [Miao 2002], He *et al.* [He 2003], Williams *et al.* [Williams 2003], Zuo *et al.* [Zuo 2003] and others.

4.3 Reconstructing diffraction patterns

As mentioned before, the measured diffraction pattern only measures the intensity and therefore the phase is lost and has to be retrieved. In 1972, Gerchberg and Saxton developed a computer algorithm that would reconstruct an object from an intensity measurement of the object in real space ($|f|$) and a measurement of the Fourier modulus of an object ($|F|$) [Gerchberg 1972]. The algorithm iterates between Fourier and object domains and makes use of the modulus constraint in both domains, while keeping the computed phases. A few years later, Fienup improved on the **Gerchberg-Saxton algorithm** to handle reconstructions from just a single measurement of the Fourier modulus of an object $|F|$, without the need of measuring $|f|$ as required for the Gerchberg-Saxton algorithm. In his algorithm, now called the **error-reduction algorithm**, the modulus constraint is applied in the Fourier domain. When calculating the object in real space, the object's support constraint and nonnegativity is applied, before going back into the Fourier domain [Fienup 1980]. Fienup further improved on the slow convergence of the error-reduction algorithm by introducing the **input-output algorithm** [Fienup 1982]. This algorithm differs from the error-reduction algorithm in the object domain. The steps of Fourier transforming the k-th estimate of the object domain estimate g_k, satisfying the Fourier domain constraints and Fourier transforming the result, gives a new estimate g'_k. In this case, g_k is the input and g'_k the output of the k-th iteration and both satisfy the Fourier domain constraint. Note that the input g no longer needs to satisfy the object domain constraint and therefore allows for different versions of the input function. The most successful version is the **hybrid input-output algorithm** [Fienup 1982]. Here, the next input g_{k+1} is made up of a combination of the previous input g_k and the output g'_k, so that

$$g_{k+1} \;=\; g_k - \beta g'_k, \tag{4.24}$$

where β is a constant, which was chosen to be 0.9 as used by Fienup [Fienup 1982]. Fienup's hybrid-input algorithm is the most widely used iterative algorithm and has been very successful. More recently, Elser has generalized the reconstruction algorithms by using an iterative **difference map** constructed from a pair of constraints, which he describes as projections [Elser 2003]. The projections can be the already-used Fourier modulus, support, nonnegativity, or the histogram or atomicity. The hybrid-input algorithm follows as a special case of the difference map described by Elser.

In this thesis, we are using a variation of the hybrid input-output algorithm as introduced by Marchesini *et al.* [Marchesini 2003]. This algorithm adjusts its support after a few iterations, by thresholding the current reconstruction. If the parameters are chosen correctly, the algorithm will slowly shrink the support until a good reconstruction has been achieved. The algorithm is therefore also called the shrink-wrap algorithm [Marchesini 2003, He 2003]. Figure 4.5 shows a schematic diagram of this algorithm. Henry Chapman provided the IDL translation of Stefano Marchesini's MatLab code.

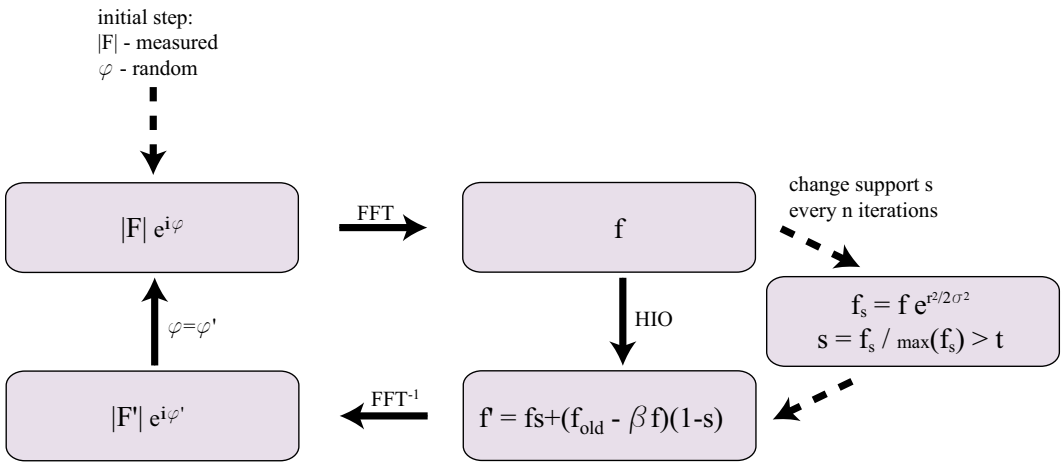

Figure 4.5: Schematic of the shrink-wrap reconstruction algorithm developed by Marchesini *et al.* [Marchesini 2003]. The initial input is the square root of the diffraction pattern intensity $|F|$ with random phases φ. The real space function f is obtained by a discrete Fourier transform. The Fienup hybrid-input algorithm is then applied, to get another estimate $|f'|$, before the inverse Fourier transform is taken. Here, the parameter $\beta = 0.9$. In the next step, the calculated phases φ' are kept and the calculated magnitude $|F'|$ is replaced with the measured magnitude $|F|$. The shrink-wrap modification is done every n loops and basically updates the support s of the object, by smoothing the current object estimate with a Gaussian of σ pixels and then applying a threshold t. In our case, $\sigma = 3$, $t = 0.4$, and $n = 20$.

4.4 Experimental demonstration

In the following, we describe diffraction experiments, conducted with the new experimental apparatus at the ALS beamline 9.0.1.

4.4.1 The sample

Even though the goal of diffraction imaging is to apply the technique to various samples from biology, materials science, etc., it is helpful to start with a rather simple object. In the initial demonstration of diffraction imaging by Miao *et al.* a microfabricated test object was used as a 2D sample [Miao 1998] and as a 3D sample [Miao 2002]. In our case, we chose a sample consisting of several 50 nm diameter gold spheres on top of a hollow silicon nitride pyramid, providing a 3D object. For a gold thickness of 50 nm the transmission is about 45 % and the phase shift is roughly 33^o at a photon energy of 750 eV. The sample has the advantage that it can be characterized in a SEM beforehand. The pyramid sample is also radiation resistant so that one does not have to worry about the radiation damage taking place while collecting a high resolution diffraction pattern. The sample was prepared by Henry Chapman and colleagues at Lawrence Livermore National Laboratory (LLNL). The pyramid was prepared by Dino Ciarlo at LLNL. To get the pyramid, he started with a double-side polished wafer and a mask for each side. The top side of the wafer was then coated with a resist and the pattern was transferred by lithography. Successive etching then produced the pits of the pyramid together with some alignment markers. A thin film of siliconnitride was applied to the top of the wafer and the back side of the wafer was coated with resist. The pattern was again transferred by lithography, while everything was aligned using an infrared transmission microscope and the previously etched alignment markers. Etching then removed the silicon and left the nitride pyramids. A solution of 50 nm diameter gold spheres was then sprinkled onto the window with the pyramid. To make sure that the gold spheres on the pyramid are the only objects contributing to the diffraction pattern, the window was swept with an atomic force microscope (AFM) [1].

[1] In the normal operating mode of an AFM, a tip on a cantilever is raster-scanned across a sample region. The tip is deflected mainly due to the van der Waals forces and the deflections are measured. When two neutral atoms or molecules are brought together they induce a dipole moment on one another, leading to an attractive force (van der Waals force). This then allows the AFM tip to sweep away gold spheres, since they become strongly attracted to the tip.

Figure 4.6 shows an angled view of a pyramid taken with a SEM microscope together with a more detailed SEM picture of the pyramid sample.

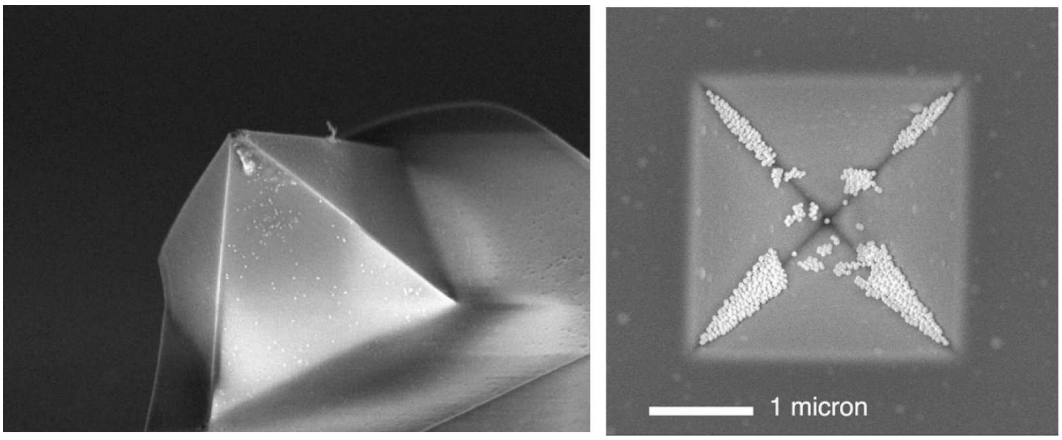

Figure 4.6: View of the pyramid sample. Image on left side taken with a SEM microscope. The image on right side, taken with SEM, shows the gold spheres on top of the pyramid [Figures from H. Chapman].

The 50 nm diameter gold spheres lie in clumps on top of the pyramid. This sample was used for collecting diffraction data together with zone plate images as described in the following sections.

4.4.2 Experimental conditions

The data presented here was collected at the ALS beamline 9.0.1, which was discussed in detail in Section 2.3. Figure 4.7 shows a schematic diagram of the elements used in the experimental chamber.

The X-ray beam from the zone plate monochromator is focused onto the pinhole, located in the experimental chamber. The pinhole serves as the coherence defining aperture (see Section 4.1.7) and as a beam defining aperture. The sample is placed in the central beam coming from the pinhole. Since there is significant scatter from the pinhole (rough edges, even with a laser-drilled pinhole), a corner is placed just in front of the specimen to block out the unwanted light, which would contribute to the diffraction pattern (idea due to

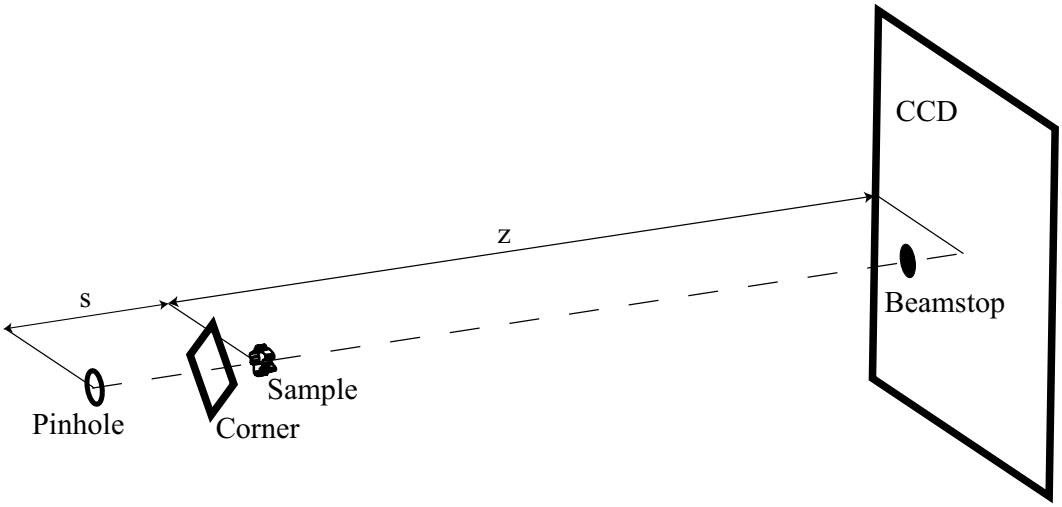

Figure 4.7: Schematic diagram showing the elements used for the diffraction imaging experiment. The X-ray beam passes through the pinhole and is incident on the specimen. A corner, located in front of the specimen, gets rid of unwanted scattered light produced by the pinhole. A CCD detects the diffraction and a beamstop in front protects the CCD from the intense direct beam. The distances s and z are given in Table 4.1.

Henry Chapman, then a postdoc at Stony Brook)[2]. The diffraction pattern is recorded on a CCD and a beamstop in front of the CCD protects it from the intense direct beam. Table 4.1 summarizes the chosen experimental values.

4.4.3 Combining diffraction with imaging/holography

The beamstop in front of the CCD is a problem when reconstructing the scattering object, since it blocks out the low spatial frequency information. The low spatial frequency information is crucial for reconstructing the object. Figure 4.9 shows the effect of missing low spatial frequency information in a diffraction pattern. To keep the missing central region as small as possible,

[2]In the experiments described below, we found that the use of the corner to block out scattering from the pinhole was not really necessary. However, the corner was still used to limit the light coming through the rather large window of the sample.

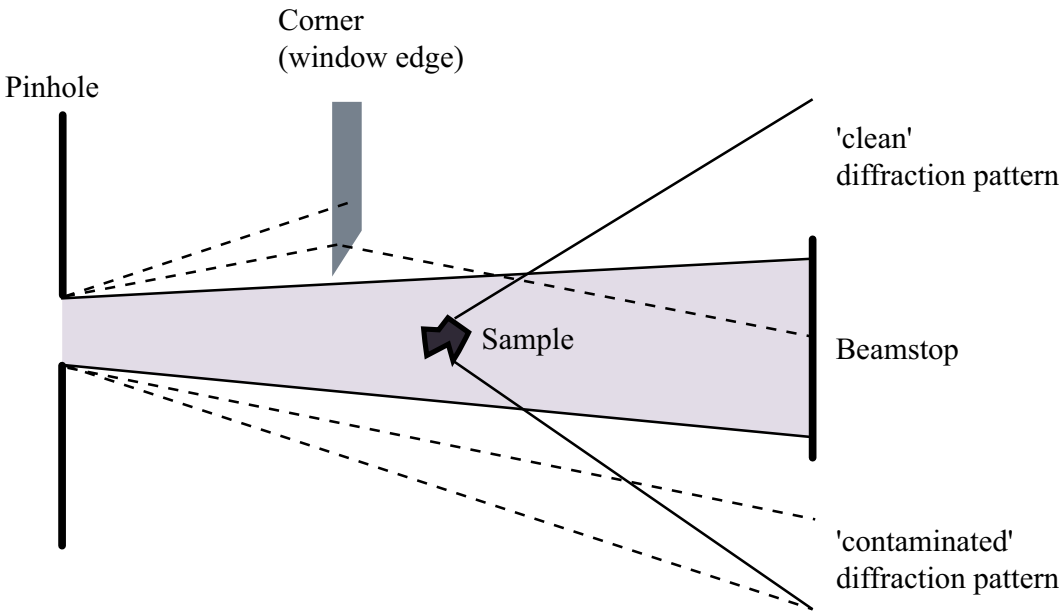

Figure 4.8: Usage of the window corner to record a clean diffraction pattern. Scattered light emerging from the pinhole is blocked or refracted so that a quadrant of the CCD records only the diffraction from the scattering sample [idea due to Henry Chapman, then a postdoc at Stony Brook].

the beamstop can be slightly moved to acquire diffraction patterns using short exposure times. Later on, these diffraction patterns are added up. In our experiments, the missing central region is a patch of about 65 by 80 CCD pixels, corresponding to a resolution element of 200 nm by 160 nm and a spatial frequency of 2.5 μm^{-1} by 3.0 μm^{-1}.

To record the high spatial frequency information, diffraction patterns with larger exposure times have to be recorded too. Figure 4.10 shows diffraction patterns acquired with an exposure time of 0.5 s and 100 s. All the diffraction patterns with different exposure times and different beamstop positions are then subject to a threshold, to take out pixels that were overflowing during an exposure. In addition to that, the recorded intensity is normalized by the exposure time, before all recordings are added up, to yield the complete diffraction pattern shown in Figure 4.11.

However, even though the missing central region of the diffraction pattern can be minimized, there are still a significant number of pixels missing. In

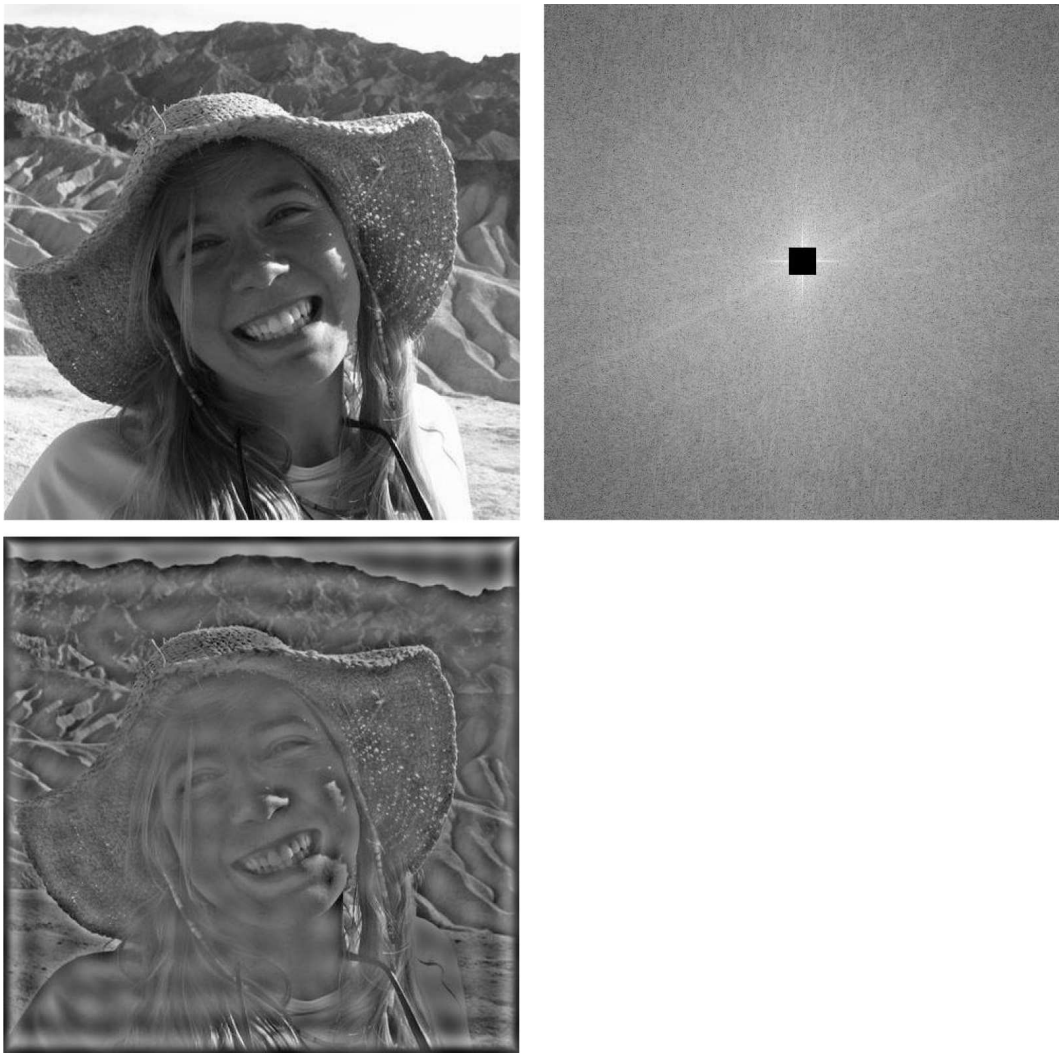

Figure 4.9: Demonstration of missing low spatial frequency information in the diffraction pattern. Top left: image of Meghan Sumner at Zabriskie Point; top right: Fourier transform (log scale) of the image with a central region missing; bottom left: inverse Fourier transform of top right image. The resulting image is a high-pass filtered version of the original image. The number of missing pixels corresponds roughly to the number of pixels in a real diffraction pattern.

Description	**Symbol**	**Value**
Energy [eV]	E	750
Wavelength [nm]	λ	1.65
Detector pixel size [μm]	Δx	20
Number of detector pixels	N_x	1300
	N_y	1340
Illuminating pinhole diameter [μm]	d_{ph}	5
Distance pinhole-sample [mm]	s	~ 25
Distance sample-CCD [mm]	z	150

Table 4.1: Summary of the experimental parameters used in the diffraction experiment.

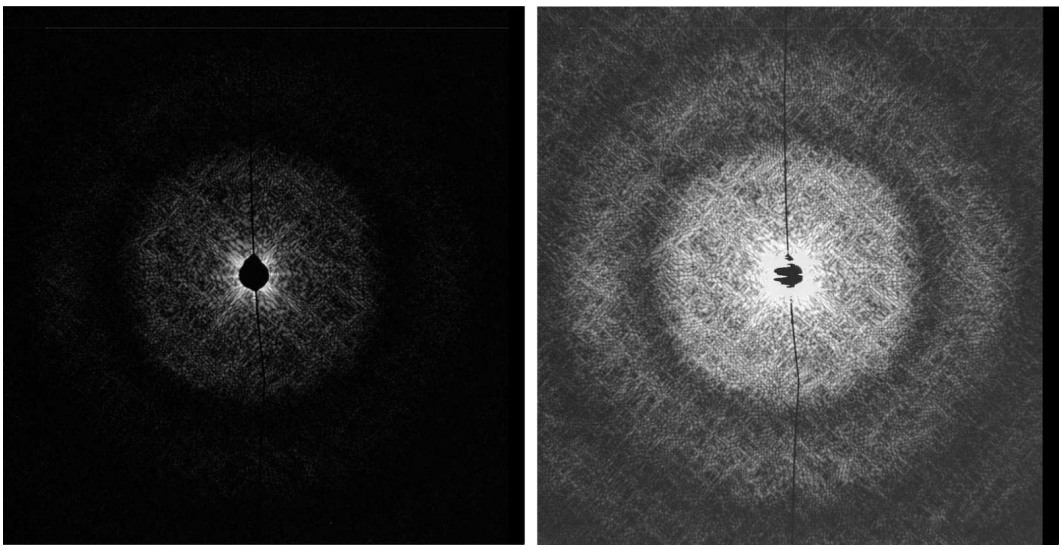

Figure 4.10: Diffraction patterns of the pyramid sample. The exposure time for the left image was 0.5 s, whereas the exposure time for the right image was 100 s. Both images are displayed on a logarithmic scale. In the image with the 100 s exposure time, one can see a bright region around the outer region of the beamstop. Since a CCD pixel is like a bucket, which fills up with charges generated by the incoming photons, the charge will overflow into neighboring CCD pixels. Before a reconstruction is attempted, one has to threshold the image, so that overflowing pixels are taken out.

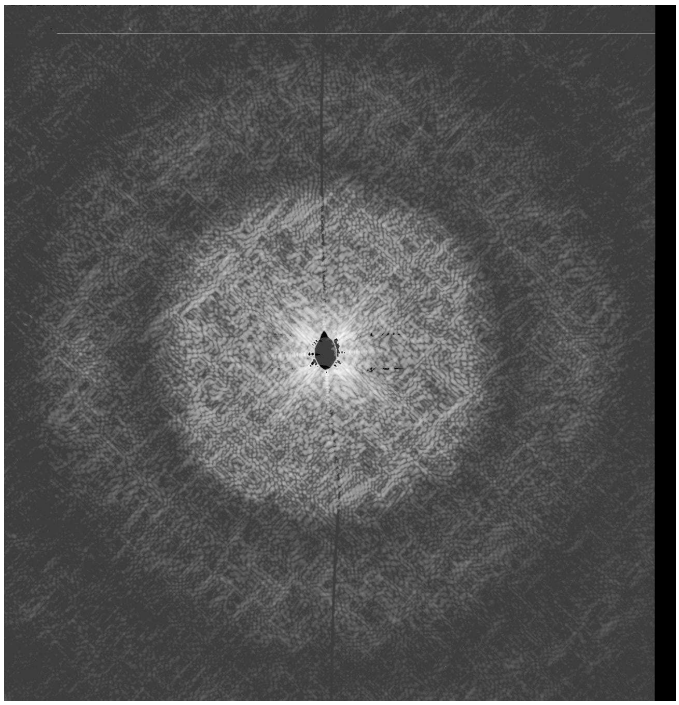

Figure 4.11: Combined diffraction pattern of the pyramid sample on a logarithmic scale. Several diffraction patterns with various exposure times were added up after a threshold was applied and the intensity was normalized by the exposure time. The central region is blocked out by the beamstop.

the past, low-resolution images obtained with a visible light microscope have been used to fill in the missing data [Miao 1999]. But since two different types of microscopes are being used, one has to ensure that the sample can be located in both microscopes. Furthermore both techniques should have similar contrast mechanisms and the exact sample orientation has to be matched and distortions eliminated. Changing imaging stations is even more difficult when dealing with cryogenically cooled specimens.

To overcome these difficulties, we have constructed our new apparatus so that the holography setup as described in Section 3.3.2, can be used to record a low-resolution zone plate image of the specimen. That image can then be used to provide the low-spatial frequency information in the diffraction pattern. The image recorded with the zone plate is in practice also a low magnification image, since the magnification is proportional to the separation distance between zone plate and detector (see below). With the detector at a close distance to the sample as required by diffraction imaging, it is not feasible to insert an extension tube when switching to the imaging configuration. Figure 4.12 shows a zone plate image of the pyramid sample.

The right image of Figure 4.12 is a cut-out, magnified view of the pyramid sample. The edges of the image have been smoothed using a Gaussian for subsequent image manipulation. To switch between diffraction mode and imaging mode is a matter of moving a few motors, to accommodate the different optics used for each technique. After the initial alignment procedure, switching between diffraction imaging and zone plate imaging takes only a few minutes. We have been using a 80 μm diameter nickel zone plate with an outermost zone width of 20 nm. The zone plate was produced several years ago by former graduate student Steve Spector. According to Eq. (1.25), the focal length of the zone plate is then 968 μm. With a separation distance of about $z = 160$ mm between the zone plate and the CCD, the magnification is roughly 165. Therefore a detector resolution element of $\Delta x = 20$ μm (CCD pixel size) corresponds to a sample resolution element of $d = 121$ nm. We should therefore be able to fill in a section of N by N pixels in the central region of the diffraction pattern, where N is given as

$$\begin{aligned} N &= \frac{\lambda z}{d\Delta x} \\ &= 110 \text{ pixels.} \end{aligned}$$

By manually moving the CCD camera back on its slider, the distance between the zone plate and the CCD can be increased from 160 mm to 260 mm, resulting in a magnification of roughly 270. An upgrade from the manual CCD translation stage to a motorized stage is currently under development and will

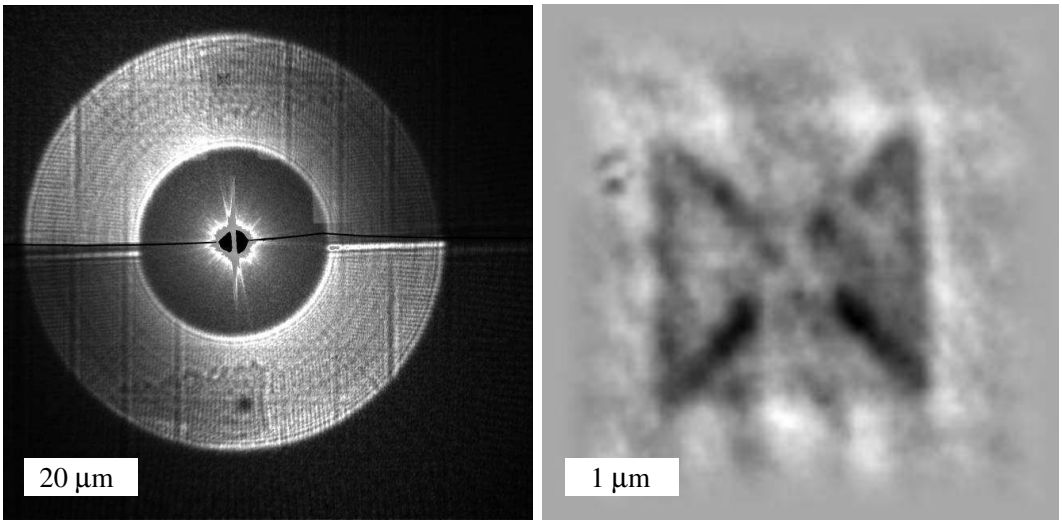

Figure 4.12: Zone plate image of the pyramid sample. **Left image**: Zone plate image showing the pyramid in focus (top) from the positive first-order focus and out of focus (bottom) from the negative first-order focus. Also visible are the 10 μm by 10 μm writing fields from the e-beam writer (JEOL JBX-6000) used to produce the zone plate. **Right image**: Magnified (and rotated) version of the image produced by the positive first-order focus. The cut image is also smoothed at the edges for subsequent image manipulation.

make switching between the diffraction and zone plate mode easier and faster.

In order to fill in the central pixels of the diffraction pattern, the following steps were done using software:

- calculate the Fourier transform of the zone plate image as shown in Figure 4.12
- determine speckle size and speckle intensity of the Fourier transform of the zone plate image (see Figure 4.13 a))
- determine speckle size and speckle intensity of the diffraction pattern (see Figure 4.13 b))
- calculate and apply the correct size and intensity scaling
- apply a beamstop mask to the diffraction pattern
- fill the beamstop mask with the data from Fourier transform of the zone plate image (see Figure 4.13 c))
- use merged diffraction pattern as input for the reconstruction algorithm

The resulting merged diffraction pattern for the pyramid sample is shown in Figure 4.14. It has all the missing low-spatial frequency information filled in and can be directly used as input for the reconstruction algorithm to reconstruct the scattering object as described in the following section.

We also note here another advantage of using the zone plate imaging setup for the diffraction experiment. Namely, one wants to make sure that the scattering object is isolated from other scattering objects that would otherwise contribute to the recorded intensity of the diffraction pattern [3]. As can be seen in Figure 4.12, the surrounding of the scattering object can be checked with a zone plate image. This large field of view was achieved by taking out the illuminating pinhole, which is normally in front of the specimen and restricts the field of view to about 5-10 μm.

[3] In certain cases, one actually prefers samples that consist of, for example, two clustered locations. The recorded diffraction pattern will then be the superposition of the wavefields emerging from the two clusters. A reconstruction of the two clusters can be easier, since it can be treated as a holographic recording [He 2003].

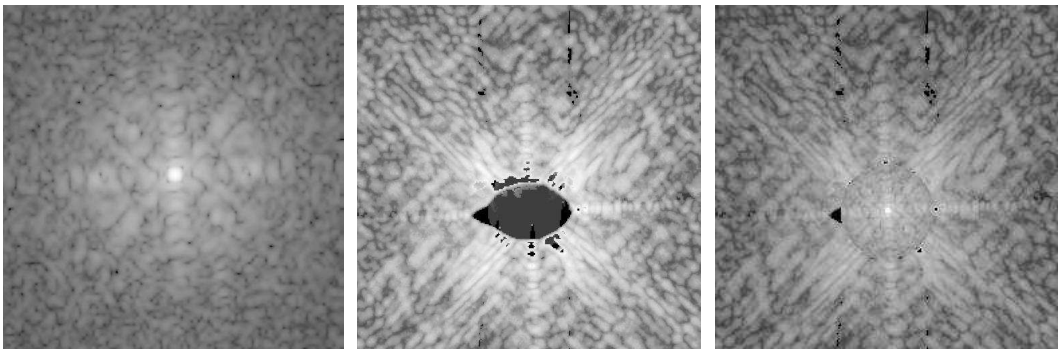

Figure 4.13: Patching the diffraction pattern with a zone plate image. a) Fourier transform of the zone plate image as shown in Figure 4.12. This image is used to determine the speckle size and intensity obtained from the zone plate image. b) Central region of the merged diffraction pattern. This image is used to determine the speckle size and intensity obtained from the measured diffraction pattern. c) Scaled patch from the zone plate image is merged into the diffraction pattern.

4.4.4 Reconstruction of the experimental data

A reconstruction was achieved by taking the assembled diffraction pattern, as described in the previous section, and using it as an input for the reconstruction algorithm (see Section 4.3). Figure 4.15 shows several steps of the reconstruction algorithm together with the best reconstruction. The reconstruction after iteration 740 was taken as the best reconstruction. The 740 iterations took about 150 minutes on a Pentium 450 MHz computer with 512 MB of RAM. With each iteration, the current estimate of the object function was saved and later assembled into a movie. The movie can be found in Appendix C.1.

For judging the quality and the progress of a reconstruction, it can be helpful to introduce an error function. There is a variety of error functions being used in the literature (see for example [Fienup 1982, Elser 2003]). In our reconstruction, we have found that the function G, defined as

$$G = \frac{\sum_N \{|f|(1-s)\}^2}{\sum_N |f|^2}, \tag{4.25}$$

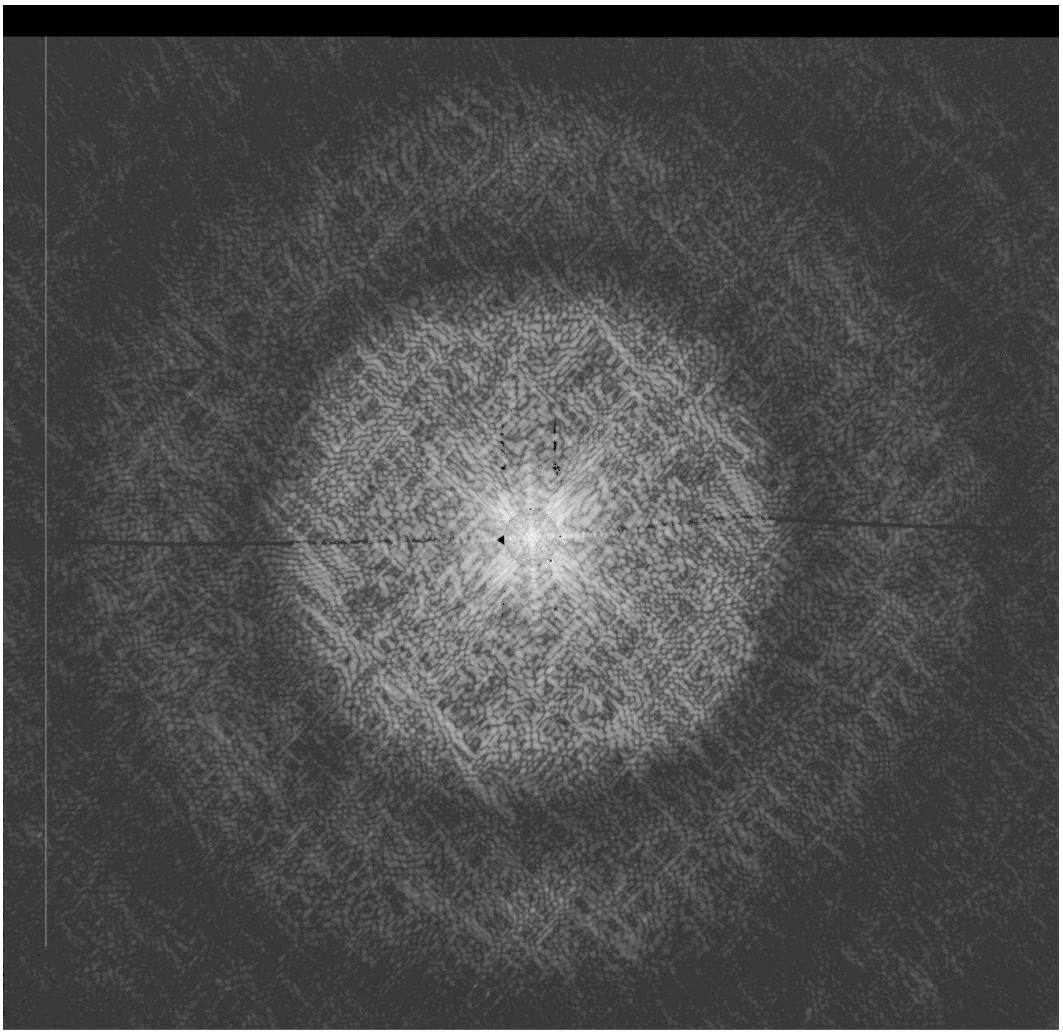

Figure 4.14: Combined diffraction pattern of the pyramid sample on a logarithmic scale. The missing low spatial information, covered by the beamstop, is filled in with data from the zone plate images. Part of the wire which holds the beamstop can be still seen as a dark horizontal line.

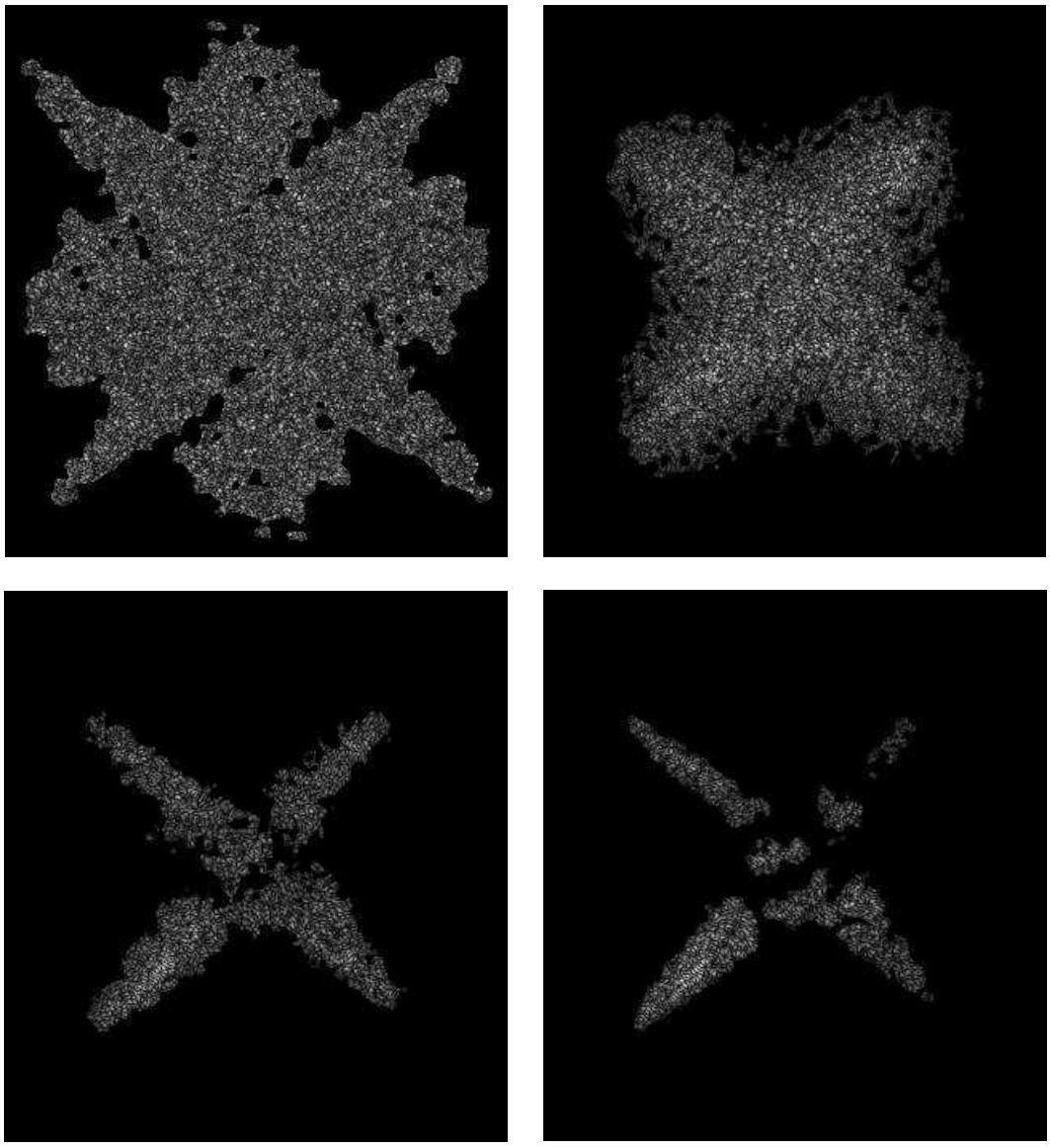

Figure 4.15: Reconstruction of the pyramid sample after 1 iteration (top, left), after 501 iterations (top, right), after 701 iterations (bottom, left), and after 740 iterations (bottom, right).

allows a good judgment of the goodness-of-fit for the reconstruction. Here, f is the current real space estimate, s the real space support, and the sum is over all pixels. Figure 4.16 shows the goodness of the fit plotted for each iteration. From the plot, we can see that the quality of the reconstruction improves with

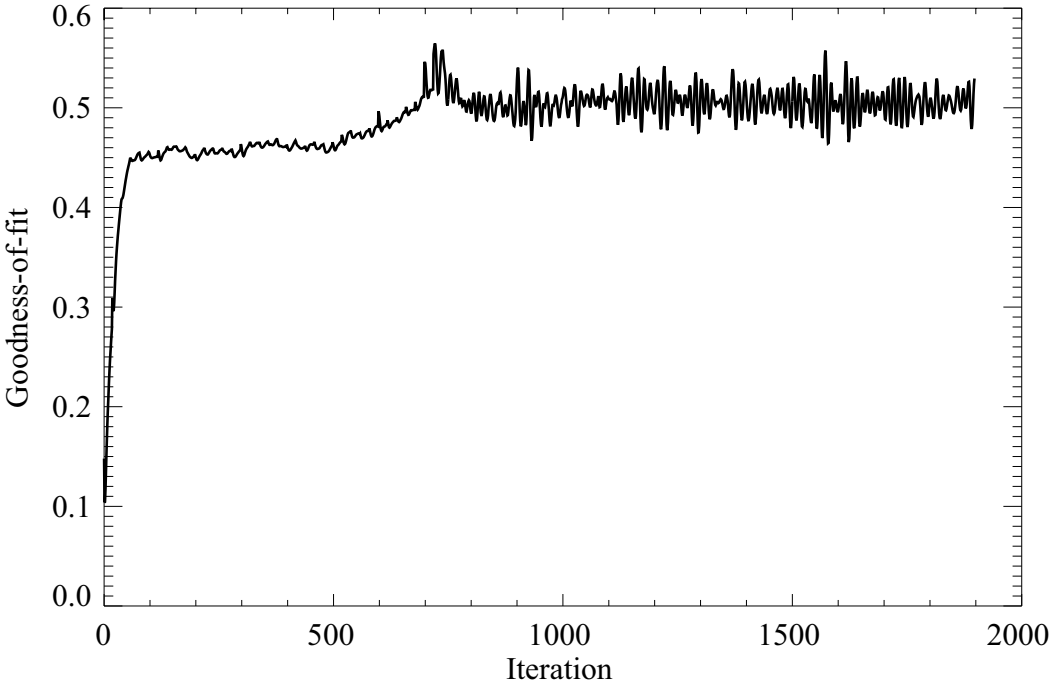

Figure 4.16: Goodness-of-fit for the pyramid reconstruction. The quality of the reconstruction improves with subsequent iterations. As the shrink-wrap algorithm is continuing to tighten the object support, it will eventually take parts of the object away. This can be seen in the plot at iteration 740.

subsequent iterations (a perfect reconstruction would have a value of 1). As the shrink-wrap algorithm is continuing to tighten the object support, it will eventually take parts of the object away. This can be seen in the plot after iteration 740. At that point, the algorithm therefore has to be changed so that the support is not changed any further and only the hybrid-input together with the error-reduction algorithm is used.

The quality of the reconstruction is far from what is expected by just looking at the diffraction pattern, which extends well out to a resolution of about 12 nm (see Eqn. 4.13). However, the reconstruction does not clearly reproduce all the individual 50 nm diameter gold spheres which make up the specimen. We chose not to specify a resolution for the reconstruction, since the previously used method of measuring the slope for the contrast between the object and the surrounding [Miao 2002] can be influenced by changing the contrast level during the reconstruction process. There is some controversy on what would be the best way to determine the achieved resolution. Recently, Chris Jacobsen suggested that one could judge the quality of the achieved reconstruction by looking at the difference between the measured and calculated spatial frequencies for several reconstruction attempts that started with a random phase input. One would expect that the lower spatial frequencies show less variations than the higher spatial frequencies. This change in difference could be used to determine the obtained resolution cut-off.

At this point it is not yet clear why the reconstruction does not yield a better image of the specimen. One of the next steps to obtain a better reconstruction should be to obtain a more thorough investigation of the reconstruction algorithm, to determine how sensitive the outcome of the reconstruction is to imperfect diffraction data. For example, the intensity and size scaling applied to the Fourier transform of the zone plate image is a potential source of errors. Instead of imposing the whole assembled diffraction pattern, one could mask the region where the zone plate image was filled in, and then let those pixels be adjusted by the algorithm. We have seen in the above discussion, that the shrink-wrap algorithm keeps shrinking the support. A devised version of the algorithm should therefore stop shrinking the support at some point. Improvements to the reconstruction algorithm should also account for the contribution coming from the pyramid silicon nitride structure itself. The silicon nitride should be about 100 nm thick. With the 55^o angle of the pyramid faces this gives about 73 nm of additional thickness of the silicon nitride at the pyramid faces, resulting in an absorption of 10 % and a phase shift of roughly 14^o at 750 eV. Although this is a rather small contribution, it should be included in the reconstruction. Determining the exact center of the diffraction pattern needed to fill in the patch is another problem. Using model data to test and alter the reconstruction algorithm should improve the final reconstruction and give a feedback of how to determine the quality of a recorded diffraction pattern. With this knowledge, the recording process and optical components in the system can be optimized.

4.5 Extending diffraction imaging to 3D

One of our goals is to extend diffraction imaging to obtain three-dimensional reconstructions of non-periodic objects. We have made the first steps towards this goal by designing the experimental apparatus that make 3D data collection feasible. We have further used the pyramid sample to collect diffraction patterns at several sample orientations. Diffraction data from the pyramid was collected from -65 degrees to +65 degrees in 1 degree steps.

A reconstruction was obtained by Henry Chapman. He assembled a diffraction pattern at each sample orientation by combining several diffraction patterns with different exposure times, as described in Section 4.4.3. However, instead of patching the diffraction pattern with the Fourier transform of the zone plate image, he used the SEM image to get the position of each gold sphere. He was then able to generate a model which was used to fill in the missing data. Each of the assembled diffraction patterns was then reconstructed. Finally, a three-dimensional view of the pyramid sample was obtained by combining all the two-dimensional reconstructions. A movie of the reconstruction can be found in Appendix C.2. As in the two-dimensional case, the achieved resolution is far from what we expected from the frequency information contained in the diffraction pattern and far from the 8 nm resolution reported by Miao *et al.* for their three-dimensional microfabricted object [Miao 2002].

4.6 Discussion and future developments

We have demonstrated diffraction imaging of a single non-periodic object without the help of another microscopy technique. This was achieved by a combination of diffraction imaging with zone plate imaging in one designated purpose-built instrument. The use of the the low-magnification zone plate provides an easy tool for making sure that the surroundings of a scattering object are not occupied by other scattering objects which would otherwise contribute to the diffraction pattern. It was also shown that the low-resolution image obtained can be used to fill in the missing low-spatial frequency information in the diffraction pattern. The merged pattern was directly used in the reconstruction algorithm without the need for further manipulation.

We have successfully constructed a new experimental chamber, since this was pointed out by Sayre *et al.* to be one of the crucial elements for success of the diffraction imaging technique ("The principle need at present is for better instrumentation for collecting the diffraction data, including the additional motions needed for collecting data in three dimensions", Sayre *et*

al. [Sayre 1998]). The described apparatus and technique are well suited for experiments where the scattering object is, for example, a frozen-hydrated biological cell and cannot be well prepared before the experiment. Efforts are already under way in our group by Shapiro *et al.* to study yeast cells, which are made more radiation resistant by plunge-freezing them.

Future of diffraction imaging The necessary hardware has been successfully constructed and characterized to see the diffraction imaging technique prosper throughout the next few years. The technique itself is established, but more work needs to be invested in improving the quality of the reconstruction. In addition, acquiring better diffraction data (for example, by using an absorber as discussed below) and work on improved reconstruction algorithms should be investigated, to take full advantage of the technique to improve the possible resolution. With steady improvements in both fields, the technique will have to provide images that could not be obtained with any other imaging technique. This would make diffraction imaging the method of choice for many researchers.

Future upgrades The next few years of operation will also see a number of improvements in the operations of the experimental apparatus making data collection easier. One of the upgrades will be a motorized stage to translate the CCD along the optical axis. This will make the process of switching between the diffraction mode and a good zone plate image much faster so that it could also be automated. Another upgrade will be a motorized stage to translate the CCD transverse to the optical axis or an improved set of beamstops. An absorber could also be placed in the beam instead of the beamstop to record the low spatial frequency information and find the center of the diffraction patterns. One has to be careful in choosing the right thickness of a material so that the CCD is not damaged by the direct beam. If this can be managed, one could simply add all the diffraction patterns obtained with a beamstop and the diffraction pattern obtained with the absorber, to get the complete pattern without much processing. Furthermore, the experimental control software is constantly improving, allowing for easier and more efficient data acquisition. Software tools that will allow the user to judge the quality of the recorded diffraction pattern are planned to be incorporated in the acquisition software. Finally, a large-scale computing infrastructure is currently being acquired and will be set up at BNL's Center for Data Intensive Computing. The computer cluster will probably consist of 20 nodes of 3.06 GHz Xeon processors, each with 1 Gbytes RAM. It will be capable of providing reconstructions of ac-

quired data sets within a few hours. More importantly, it will also be able to run the reconstruction algorithms on 3D data sets by doing 3D Fast Fourier transforms instead of reconstructing each diffraction pattern in 2D and then assembling the reconstruction to yield a 3D image.

We hope to have shown that diffraction imaging will become a valuable technique which can be used as a tool by a large community for research in many fields, such as biology and materials science.

Chapter 5

Radiation damage

This chapter offers an overview of the mechanisms of radiation damage and how radiation damage influences the achievable resolution in an image. Radiation damage sets a fundamental limit to high-resolution imaging using ionizing radiation. We also give some typical doses necessary for high-resolution imaging.

Cryo fixation is one technique that has been known to improve the radiation resistance of objects. However, data presented here indicate that there is no advantage for cryo fixation when the main interest is in obtaining the spectroscopic information of radiation sensitive specimens.

5.1 Fundamentals of radiation damage

When dealing with ionizing radiation, one distinguishes between two types of radiation damage: **Primary damage** is caused by the direct interaction of the ionizing radiation with the electrons in the object. The interaction via the photoelectric, Auger, or Compton effect generates energetic electrons from the breakage of chemical bonds within the specimen. These energetic electrons are responsible for creating 'free radicals' that are the cause of **secondary damage**. In this case, the free radicals can diffuse and further alter the chemical state of the object giving rise to further damage. Whereas primary damage depends only on the energy of the incident radiation and the number of photons absorbed, secondary damage depends on the properties of the object.

5.1.1 Radiation dose

The radiation dose is a measure of absorbed energy per mass

$$\text{Dose} = \frac{\text{absorbed energy}}{\text{mass}}. \tag{5.1}$$

The SI unit of the dose is the Gray (Gy). One Gray is equal to an absorbed dose of 1 joule/kilogram. For a given number of photons N per unit area A the energy per unit area is given as

$$\Phi = \frac{NE}{A}, \tag{5.2}$$

where E is the photon energy. From Eq. (1.15), we know that the number of photons decreases with increasing penetration distance, meaning $\Phi = \frac{N_0}{A} e^{-\mu z} E$. Therefore the deposited energy at the surface is

$$\begin{aligned} \frac{\partial \Phi}{\partial z}|_{z=0} &= \frac{\partial}{\partial z}(\frac{N_0}{A} e^{-\mu z} E)|_{z=0} \\ &= -\mu \frac{N_0}{A} E. \end{aligned} \tag{5.3}$$

And finally, the dose in a material with density ρ can be written as

$$\text{Dose} = \frac{\mu N_0 E}{\rho A}. \tag{5.4}$$

The effects of ionizing radiation on biological specimens have been studied; a typical result is that at about 3 Gy half of a cell culture will die [Okada 1970]. Structural changes become visible at a much higher dose of about $10^4 - 10^5$ Gy [Kirz 1995].

5.2 Image resolution

Radiation damage measurements have been done by Williams *et al.* [Williams 1993] on a glutaraldehyde-fixed *Vicia faba* chromosomes using the Stony Brook room-temperature STXM. Figure 5.1 shows images of the chromosome after certain applied doses.

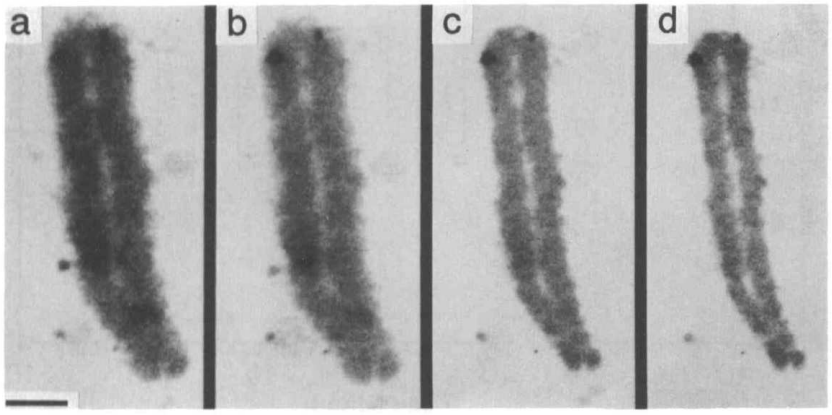

Figure 5.1: Repeated images of a single 0.1 % glutaraldehyde-fixed *Vicia faba* chromosome in 65 mM buffer after previous doses of (a) 0 Gy, (b) 0.35 MGy, (c) 1.39 MGy and (d) 2.40 MGy. Scale bar = 2 μm [reprinted from [Williams 1993]].

Shrinkage of the chromosome, which is attributed to mass loss, is clearly visible in the images as the applied dose increases and the damage takes place.

In the above experiment, absorption contrast between different materials within the chromosome gives rise to the image contrast. We can estimate the dose that is needed to record the image at a given resolution following an argument by Rose [Rose 1948]. The **Rose criterium** states that the signal to noise ratio must be at least 5 in order to distinguish an arbitrary object from noise. In 1977, Sayre *et al.* applied the Rose criterium to estimate the dose expected in X-ray microscopy [Sayre 1977]. Later work on calculating the required dose in X-ray microscopy also included phase contrast imaging [Rudolph 1990, Gölz 1992, Schneider 1992, Jacobsen 1998]. The calculated dose for 50 nm resolution imaging with soft X rays is about 10^6 Gy.

For diffraction imaging, Howells *et al.* [Howells 2003] derived an expression for the needed dose to image a voxel with dimensions d x d x d and electron density $\tilde{\rho}$. They found that the scattering cross section σ_s is proportional to d^4

$$\sigma_s = r_e^2 \lambda^2 |\tilde{\rho}|^2 d^4. \tag{5.5}$$

Further, the number of photons scattered into the detector is

$$\begin{aligned} N_s &= N d^2 \sigma_s \\ &= N d^2 r_e^2 \lambda^2 |\tilde{\rho}|^2 d^4, \end{aligned} \tag{5.6}$$

where N is the number of incident photons per voxel area d^2. If we insert the expression for n_0 from the previous equation into Eq. (5.4), we end up with

$$\text{Dose} = \frac{\mu N E}{\rho r_e^2 \lambda^2 |\tilde{\rho}|^2 d^4}. \tag{5.7}$$

This equation is of great importance since it relates the dose to the imaged feature size by a fourth-power law. As an example, they calculated the dose for imaging a 30 nm protein feature in water, and got about $2 \cdot 10^7$ Gy when imaged using 500 eV X rays.

To verify the calculations, our group has collected diffraction patterns at several radiation doses. Shapiro *et al.* have collected diffraction patterns with different exposure times of freeze-dried yeast cells. We have collected data on 1 μm diameter latex spheres and a 3 μm diameter gold dot. The top of Figure 5.2 shows a typical radial power density spectrum of a diffraction pattern, which is used to determine the cut-off frequency. Note, that the spatial frequency is again defined as $1/2d$, where d is the resolution element or half-period. Here, a straight line is fitted to the decaying part of the spectral power density. The crossing of this line with the noise level then results in the cut-off frequency. The cut-off frequency was determined for each exposure time and is plotted against the dose at the bottom of Figure 5.2. The dose in each image was calculated by use of Eq. (5.4). The actual dose might differ by a factor of about two due to the uncertainty in measurement of the total incident photon flux due to the finite size of the photodiode. Furthermore, the absorption due to the silicon nitride membrane, on which the object was prepared on, has to be taken into account ($\sim$15 %). Unfortunately, we don't know if the silicon nitride membrane was upstream or downstream of the sample, which would decrease or increase the estimated dose. Overall, we would estimate a dose uncertainty of about $\pm$30 %, which would also explain the difference in

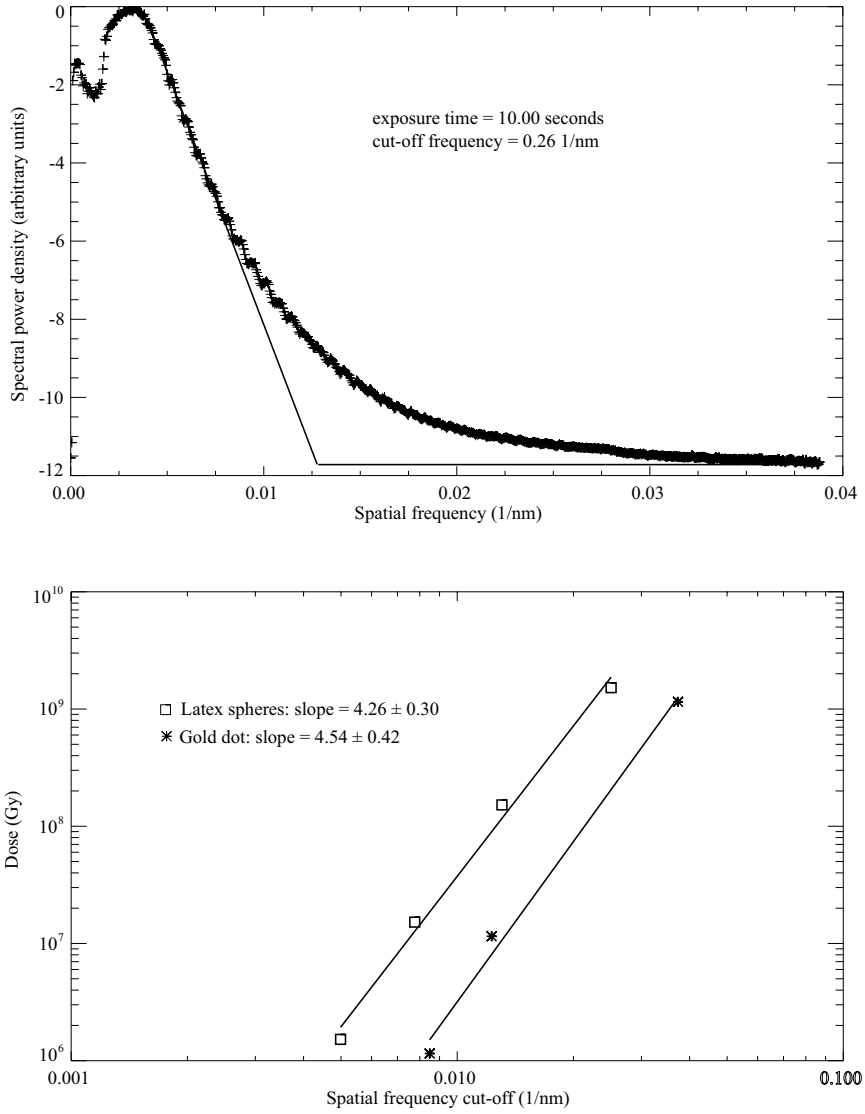

Figure 5.2: Top: Typical power density from a recorded diffraction pattern of 1 μm diameter latex spheres. The power density is used to fit a line to the decaying part of the spectrum. The intersection of the fitted line with the noise level is taken as the cut-off frequency.
Bottom: Dose as a function of spatial frequency for the latex sphere and gold dot diffraction data. The experimental values agree well with the proposed 4-th power law (see Eq. (5.7)).

dose for the measurement of the latex spheres and the gold dot. To verify the suggested 4-th power dependence of the dose on the spatial frequency (Eq. (5.7)), we have fitted the data using a straight line on a log-log plot. Since the dose and spatial frequency are plotted on a logarithmic scale, the slope of the fitted line will give the power law dependence. The slope is 4.26 ± 0.30 for the latex sphere data and 4.54 ± 0.42 for the gold dot data. Both values are in good agreement with the expected 4-th power law and are also in agreement with Shapiro's results on yeast diffraction [Shapiro 2004]. We also note at this point, that even though the uncertainty in the delivered dose is rather large, it will only shift each data point in the same way, so that the slope is not affected. The main contribution for the uncertainty in the slope arises from determining the cut-off frequency and is estimated to be accurate to within $\pm 4\ \mu\mathrm{m}^{-1}$.

From Eq. (5.7) we have seen that we need to increase the dose to get higher resolution images. While this is not generally a problem, it is an issue when dealing with radiation sensitive specimens, like biological cells, etc., where there is a limit on the dose at which the features within the sample are destroyed by the X rays. Howells *et al.* therefore estimate the achievable resolution in biological specimens to be around 10 nm [Howells 2002, Marchesini 2003].

Dose fractionation

A very important realization of the required dose when doing 3D imaging was put forward by Hegerl and Hoppe in 1976 [Hegerl 1976]. They proved theoretically that 'A three-dimensional reconstruction requires the same integral dose as a conventional two-dimensional micrograph provided that the level of significance and the resolution are identical. The necessary dose D for one of the K projections in a reconstruction series is therefore the integral dose divided by K.' In other words, the data at each viewing angle can be of much worse quality than the desired 3D reconstruction. This revolutionary idea was received with much skepticism, but gradually reached acceptance, backed by detailed computer simulations in 1995 by McEwen *et al.* [McEwen 1995].

5.3 Cryo fixation to improve radiation resistance

Even though radiation damage is always present when ionizing radiation interacts with matter, it may be reduced or minimized. It is well known from the electron microscopy community that cryo methods can greatly reduce radiation damage [Glaeser 1978, Dubochet 1987, Lamvik 1991]. For example, Glaeser and Taylor have studied the fading of diffraction spots of crystalline specimens that are exposed to electrons [Glaeser 1978]. Figure 5.3 shows the result of their measurement for samples kept at room temperature and frozen samples. They found that the frozen specimen can tolerate three to six times

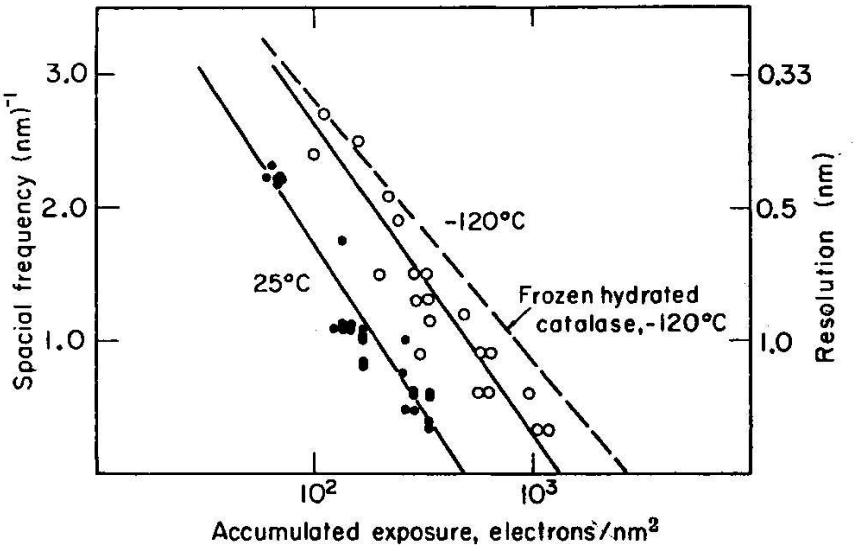

Figure 5.3: Measurement of the fading of diffraction spots for crystalline catalase after exposure with an electron beam. The cooled specimen can tolerate an approximately three times higher dose than the room temperature specimen [reprinted from [Glaeser 1978]].

higher doses than the room temperature specimen. Lamvik *et al.* studied mass loss in Epon 812 as a function of dose, when exposed to an electron

beam [Lamvik 1991]. Figure 5.4 shows their result for several temperatures, which find that the rate of mass loss is much slower and more residual mass is preserved at low temperatures.

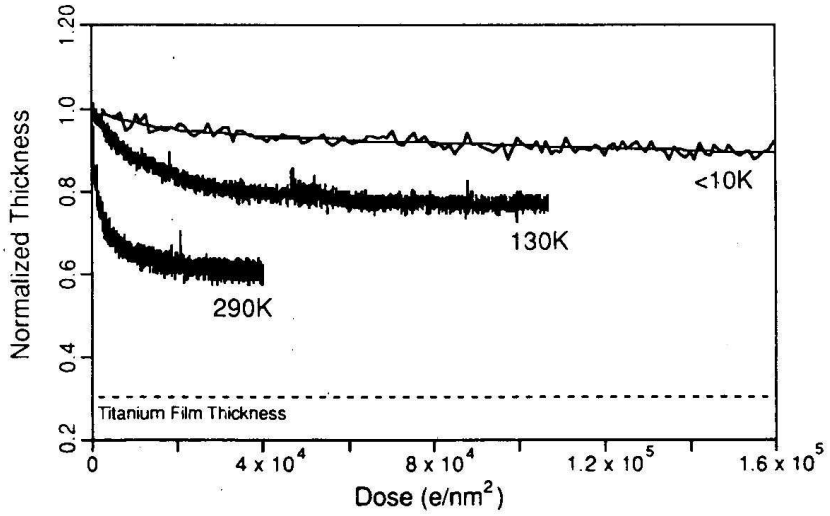

Figure 5.4: Mass loss from Epon 812 at three different temperatures. As the temperature is reduced, the rate of mass loss is slower and more residual mass is preserved. A thin titanium film was added to account for the low electrical conductivity from the carbon at low temperatures. [reprinted from [Lamvik 1991]]

Cryo X-ray microscopy experiments at -160 ^{o}C have shown essentially no observable mass loss at the 50 nm spatial resolution level with radiation doses up to about 10^{10} Gy [Schneider 1998, Maser 2000].

5.4 Cryo fixation to preserve chemical states - a study in PMMA

In the previous section we have stated that cryo fixation improves the dose limits for mass loss. However, mass loss is not the only means of radiation

damage, and cryo methods are found to improve but not eliminate degradation of high resolution electron diffraction data [Glaeser 1978]. Overall mass density can be preserved while chemical bonds are not preserved. This suggests that cryo methods may offer differing degrees of protection for spectroscopy, atomic resolution imaging, or diffraction, than simple mass loss measurements would suggest.

Radiation damage effects in soft X-ray spectroscopy have been studied by measuring the loss of X-ray absorption near-edge structure or XANES spectroscopic resonances in thin organic films. Zhang *et al.* used carbon XANES to monitor the decrease in C=O bond density due to chain scission, and the increase in C=C bond density due to crosslinking in room temperature PMMA films that were first baked at various temperatures [Zhang 1995]. C=O bond density was found to decrease exponentially with increasing dose, with a characteristic dose of about $13{\cdot}10^6$ Gy. Coffey *et al.* studied several other thin polymer films again with carbon XANES, and investigated the influence of atmospheric oxygen on the radiation damage chemistry and found that the damage rate in a helium atmosphere is slowed down by a factor of approximately 100 relative to air for their poly(ethylene therephthalate) (PET) sample [Coffey 2002]. Their experiments were also conducted at room temperature. These studies provide the background to our research of examining radiation damage using XANES spectroscopy for samples at cryogenic and room temperatures.

5.4.1 Experimental description

A film of poly(methylmethacrylate) (PMMA) prepared on top of a silicon nitride window served as our sample (see also Appendix F for more details on the experiment). PMMA (chemical structure shown in Figure 5.5) has a carbonyl functional group, which gives rise to a peak in the oxygen XANES spectra at 531.5 eV (Figure 5.7) which is due to the O 1s(C=O) $\rightarrow \pi^{\star}_{\mathrm{C=O}}$ transition [Tinone 1994]. The decrease in intensity of this transition with increasing dose is later used to quantify the damaging effects.

The imaging mode of the cryo-STXM was used to deliver a known dose to the specimen. After the dose scan, the spectroscopy mode of the cryo-STXM was used to record an oxygen XANES spectrum across the oxygen K edge. Using Eq. (5.4), we can readily derive an expression for the dose applied during a dose scan or spectrum. The dose becomes

$$\mathrm{Dose} = 1.602 \cdot 10^{-4} \frac{ENt\mu}{\rho A \eta} \text{ Gray}, \tag{5.8}$$

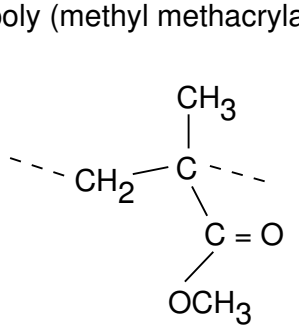

Figure 5.5: Chemical structure of PMMA.

where E is the photon energy in eV, N the number of photons per second absorbed by the sample, measured in kHz, η_{Det} the efficiency of the detector, t the exposure time in ms, ρ the density in g/cm^3, A the radiated area in μm^2, and μ the inverse absorption length in $1/\mu$m. The $1/e$ absorption length can be expressed as $1/\mu = 2r_e\lambda\frac{N_A}{A}\rho f_2$, where $r_e = 2.812 \cdot 10^{-15}$ m, N_A is Avogadro's number, A the atomic weight and f_2 is the imaginary part of the complex atomic scattering factor, which can be found from tabulated values [Henke 1993].

Since radiation dose is defined as energy absorbed per mass which is in turn proportional to the exposed area, during spectrum scans the beam was defocused to about 3.6 μm to produce a dose of only about $0.6 \cdot 10^6$ Gy per scan. This sequence was repeated many times and finally, an in-focus image with lower dwell time and a larger step size over a larger field was taken to ensure that the specimen remained centered on the X-ray beam axis. Figure 5.6 shows such images of dosed regions at both recording temperatures. A typical dose during an exposure was approximately $7.0 \cdot 10^6$ Gy for an exposure at liquid nitrogen temperature and approximately $3.7 \cdot 10^6$ Gy for an exposure at room temperature. During a spectral scan, a typical dose was about $0.6 \cdot 10^6$ Gy.

The absorption peak due to C=O bond density was fitted with a Gaussian. The height of the Gaussian was later used to quantify the loss of the C=O bond density under radiation. To determine the mass loss, each spectrum was fitted with an average value at the low (528.0 eV - 529.5 eV) and at the high

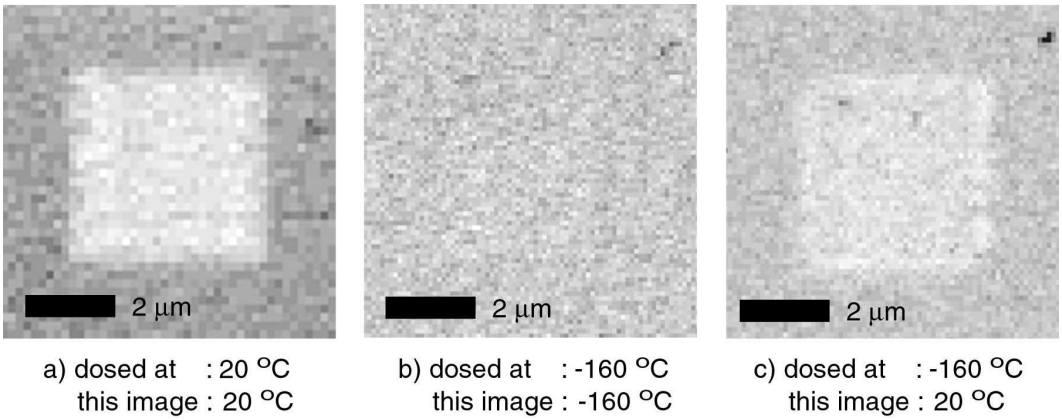

Figure 5.6: a) Coarse area scan at room temperature of a region that was dosed at room temperature. The square in the middle indicates the mass loss of the dosed region. b) Coarse area scan at liquid nitrogen temperature of region that was dosed at liquid nitrogen temperature. The image shows no visible mass loss at the dosed region. c) Same area as image b) but after warming up the sample; the dosed region becomes visible.

(538.5 eV - 540.0 eV) energy end of the spectrum (Figure 5.7). The ratio of the two average values was used to determine the oxygen mass loss as a function of dose using differential absorption analysis [Engström 1946].

5.4.2 Results

Spectroscopic observations To quantify the loss of the carbonyl group, the heights of the C=O absorption peaks determined from the XANES spectra are plotted versus the dose in Figure 5.8 a). The data was fitted using an exponential decay. The determined critical dose of about $18 \cdot 10^6$ Gray at 525.0 eV for the control experiment at room temperature is in good agreement with the previously obtained value of $13 \cdot 10^6$ Gray at 317 eV by Zhang [Zhang 1995] and $14 \cdot 10^6$ Gray at 315 eV by Coffey [Coffey 2002].

From the decay rate of the C=O bond density at both temperatures, it can be concluded that the specimen temperature has no influence on preserving XANES signatures of the chemical state of the specimen, at least in this example system.

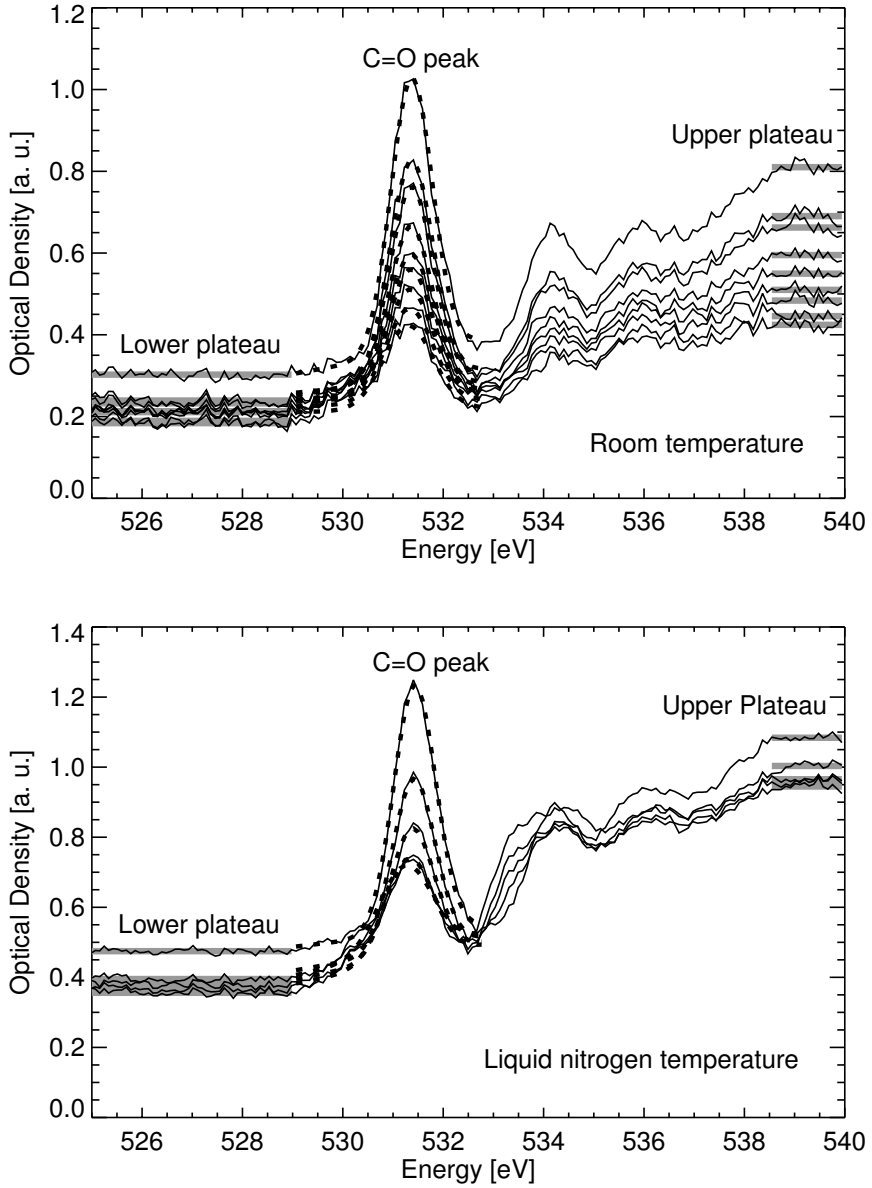

Figure 5.7: Oxygen XANES spectra of PMMA in dependence of the dose for a) room temperature and b) liquid nitrogen temperature. The spectra show the decrease of the C=O bond density with increasing dose. The C=O bond peaks were fitted using Gaussians. Also shown are the average values, denoted by upper and lower plateaus, used to determine the oxygen mass loss.

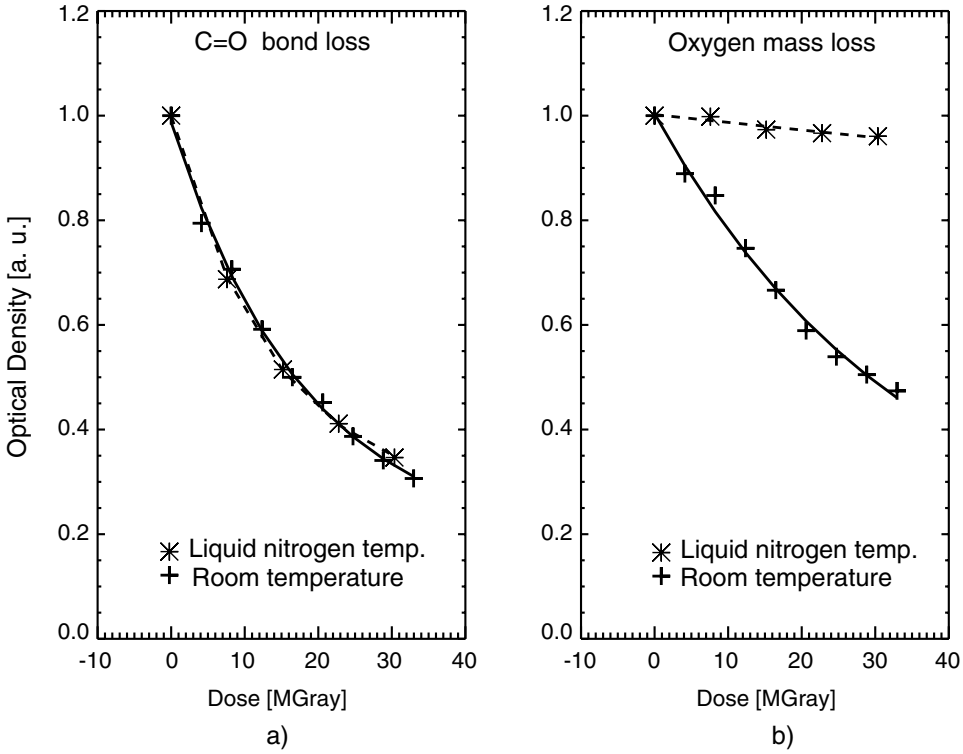

Figure 5.8: a) Loss of C=O peak intensity and b) mass loss as a function of dose at liquid nitrogen and room temperatures.

Mass loss The dependence of mass loss on dose is shown in Figure 5.8 b) for both temperatures. The data was fitted using an exponential decay. The data verifies the results mentioned earlier, that cryo helps greatly to protect the sample against mass loss.

5.4.3 Implications

We have shown that the C=O bond in irradiated PMMA is broken at comparable rates at liquid nitrogen and room temperatures. We have confirmed that cryogenic sample conditions are extremely effective for reducing mass loss, as is required for non-atomic-resolution imaging applications such as nanotomography [Wang 2000, Weiß 2000]. However, cryogenic sample conditions do not have a measurable affect on the soft X-ray radiation dose sensitivity of chemical bonds, at least in this model case of XANES spectroscopy of PMMA with no water present. This implies that chemical bonds are broken independent of temperature. However, it is the diffusion of the created radicals which is suppressed at low temperatures, that is inhibiting secondary damage, which would otherwise result in mass loss.

5.5 Conclusions

We have verified the calculations by Howells *et al.* that the required dose scales with the inverse fourth power of the desired resolution element. We have further verified that cryogenic sample preparation is effective for reducing mass loss. However, our investigations on radiation damage in PMMA have shown that there is no protection against damage to chemical bonds at cryogenic sample temperatures.

Future experiments should investigate at which doses certain feature sizes of the specimen are destroyed and can no longer be detected. A systematic measurement of this feature-destroying dose is important to determine what kind of resolution could be possible for radiation sensitive specimens.

Appendix A

Propagation

Given a wavefield at an input plane $(x_i, y_i, 0)$ we would like to know the wavefield at the output plane (x_o, y_o, d) as shown in Figure A.1. Following

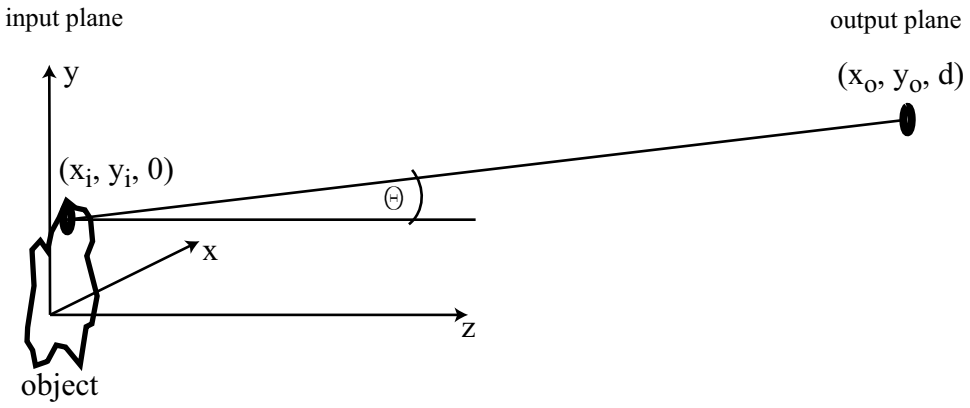

Figure A.1: Schematic diagram of the Fresnel-Kirchhoff diffraction formalism to get from an input plane $(x_i, y_i, 0)$ to an output plane (x_o, y_o, d).

the Huygens-Fresnel construction we have to sum over all spherical waves $\psi = \psi_0 \exp[-ikr]/r$ emerging from the input plane (see for example Goodman [Goodman 1968] or Born and Wolf [Born 1980]). The wavefield at the output plane can be written according to the Fersnel-Kirchhoff integral as

$$\psi_o \;=\; \int_{x_i}\int_{y_i} \psi_i \, \frac{i}{\lambda}\frac{e^{-ikr}}{r} \, \cos\theta$$

$$= \int_{x_i} \int_{y_i} \psi_i \, h(x_i, y_i), \tag{A.1}$$

where

$$h_{(x,y)} = \frac{i}{\lambda} \frac{e^{-ikr}}{r} \cos\theta \tag{A.2}$$

and $\cos\theta = d/r$ is an obliquity factor. The function $h_{(x,y)}$ is also called the propagator. We can see that Eq. (A.1) has the form of a convolution integral. If we want to calculate the output wavefield we have to convolve the input wavefield ψ_i with the phase e^{-ikr} and the obliquity factor $\cos\theta$.

A.1 Propagation in IDL

The ability to propagate a wavefield numerically in IDL has been implemented by Lindaas and Jacobsen and is discussed in detail in Lindaas' PhD thesis [Lindaas 1994]. It basically involves approximating and then calculating the distance $r = \sqrt{x^2 + y^2 + z^2}$ when $z \gg x$ and $z \ll y$, so that it can be written as

$$kr = \frac{2\pi}{\lambda} \sqrt{x^2 + y^2 + z^2} \tag{A.3}$$

$$= \frac{2\pi z}{\lambda} \sqrt{\frac{x}{y}^2 + \frac{y}{z}^2 + 1} \tag{A.4}$$

$$\simeq \frac{2\pi z}{\lambda} - \pi\left(-\frac{x^2 + y^2}{\lambda z} + \frac{(x^2 + y^2)^2}{4\lambda z^3} - \frac{(x^2 + y^2)^3}{8\lambda z^5} + \ldots\right). \tag{A.5}$$

The same approximation is also done for the obliquity factor. The IDL routine `propagate.pro`, written by Lindaas and Jacobsen will calculate the necessary propagator functions for an input wavefield and return the output wavefield. This routine was used in this dissertation to propagate wavefields.

Appendix B

Motor amplifier box

We designed and produced a motor amplifier box that takes the signals coming from two Galil DMC-2180 motion controllers and passes them on to our motors. Figure B.1 shows a schematic diagram of the devices together with connecting cables.

The motion controller applies a control voltage to move a DC motor. However, the controller does not provide the necessary power to move the motor. The necessary power is provided by an amplifier circuit located on two printed circuit boards (PCB's). Each PCB holds 8 amplifier circuits and provides the necessary connections to take signals (motor encoder, limit switches, etc.) from the controller's 100 PIN connectors to the individual cables going to the motor stacks. The boards were designed in collaboration with Chuck Pancake, Jane Wu and Bonnie Smart from the Stony Brook electronics shop. The following images show the three layers of each printed circuit board, a connection diagram for the 100 PIN connector and a schematic diagram of the amplifier circuit used for each motor.

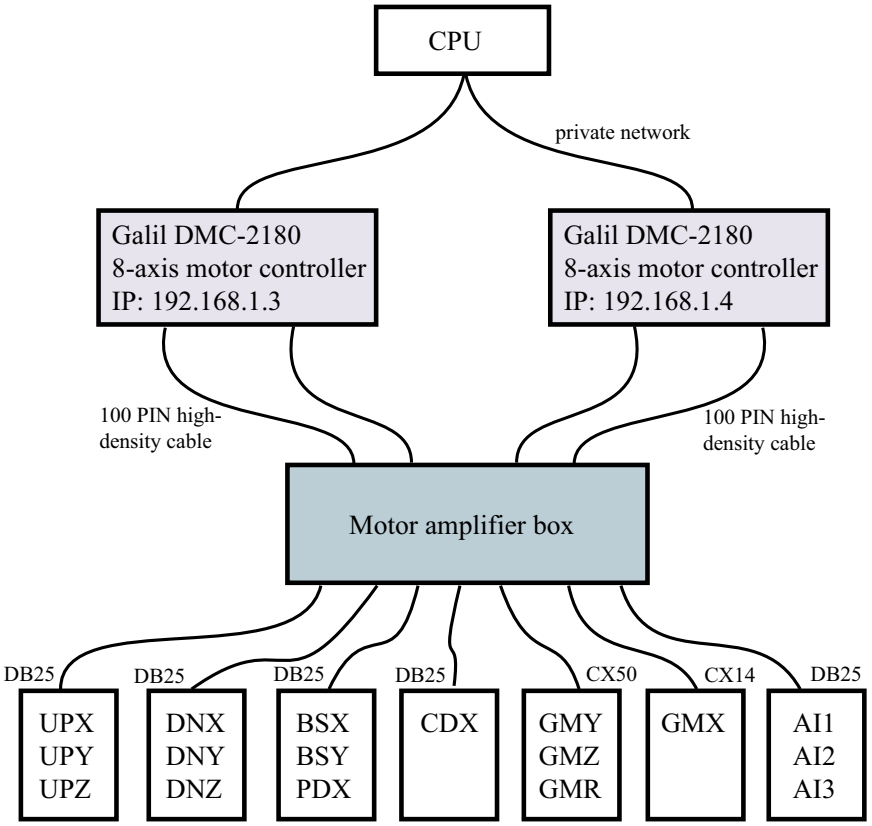

Figure B.1: Schematic showing the connections to the motor amplifier box. The computer sends instructions over a private network to the two Galil motion controllers. The signals from the motion controllers enter the motor amplifier box over four 100 PIN high-density cables. The motor signal is amplified and distributed to the motor stacks via DB25 and Centronix cables.

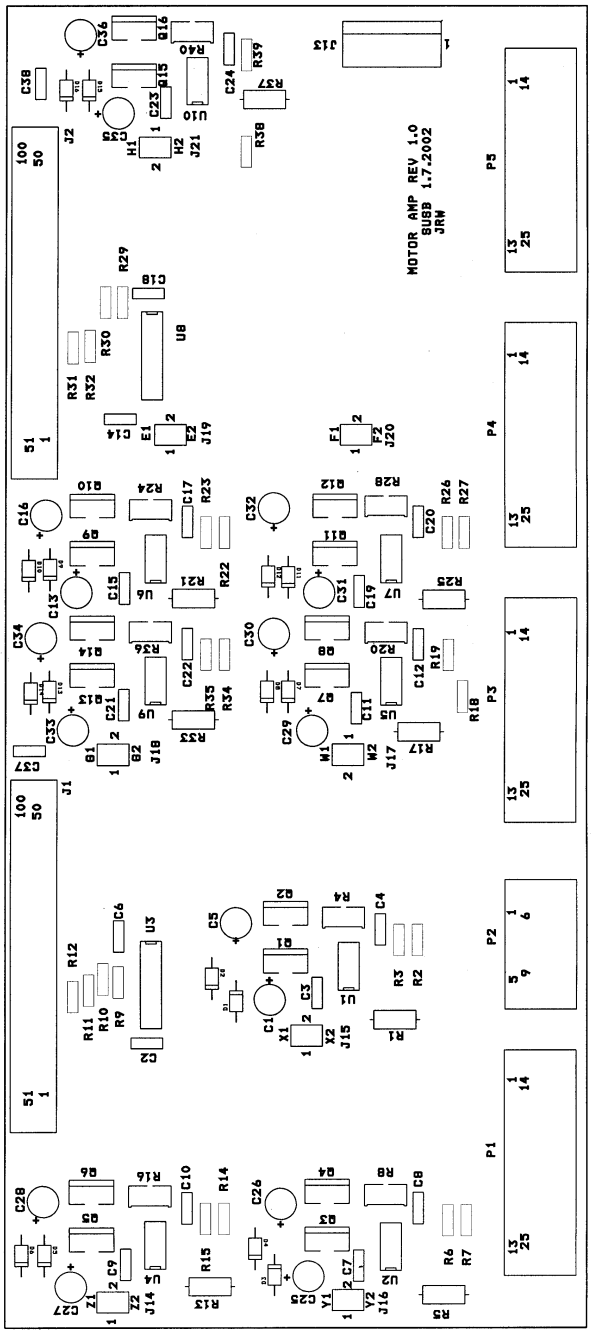

Motor_Amp PCB

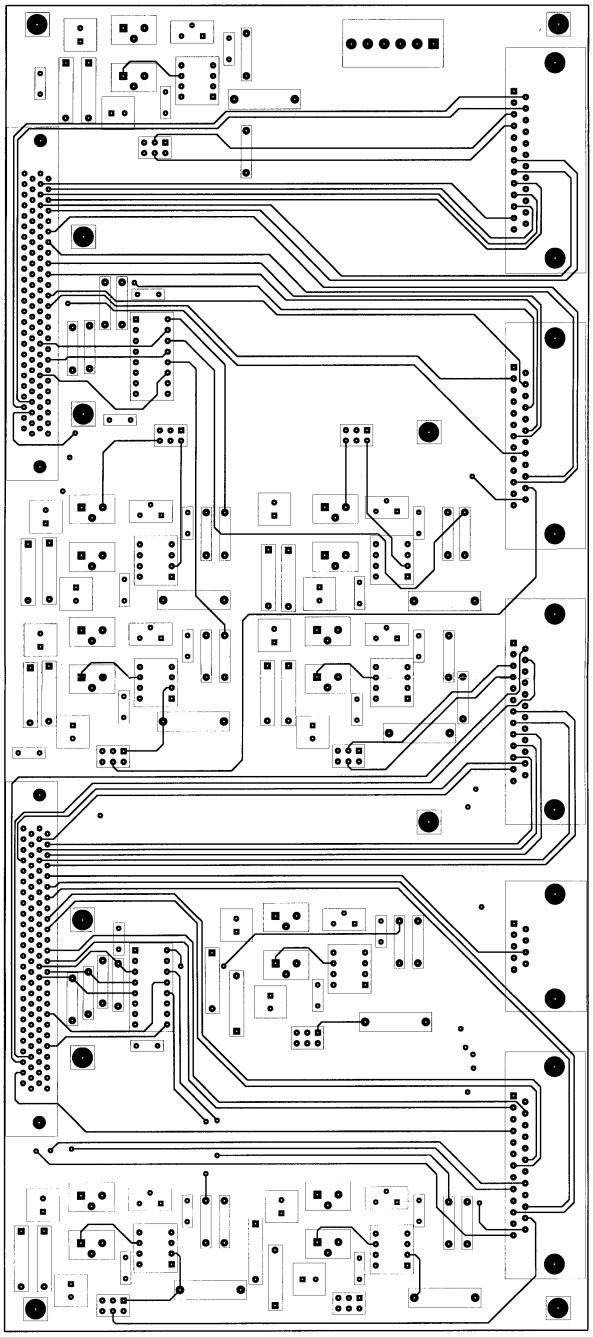

Motor Amp PCB, Top Layer

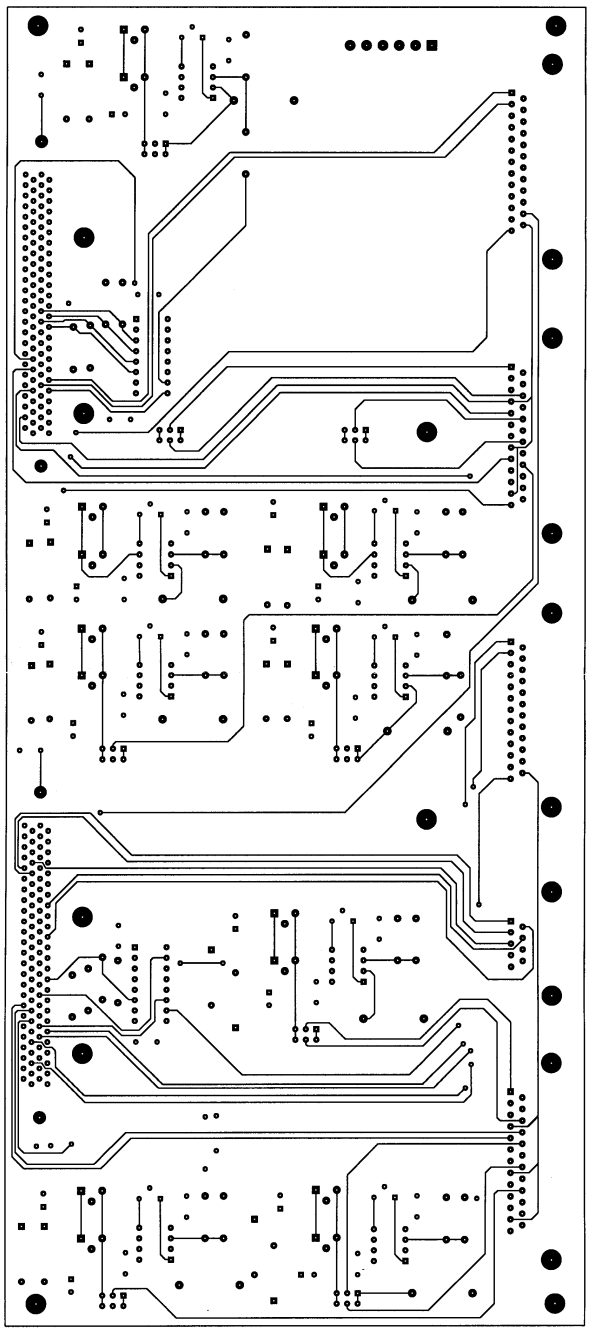

Mistir_Amp PCB, Bottom Layer

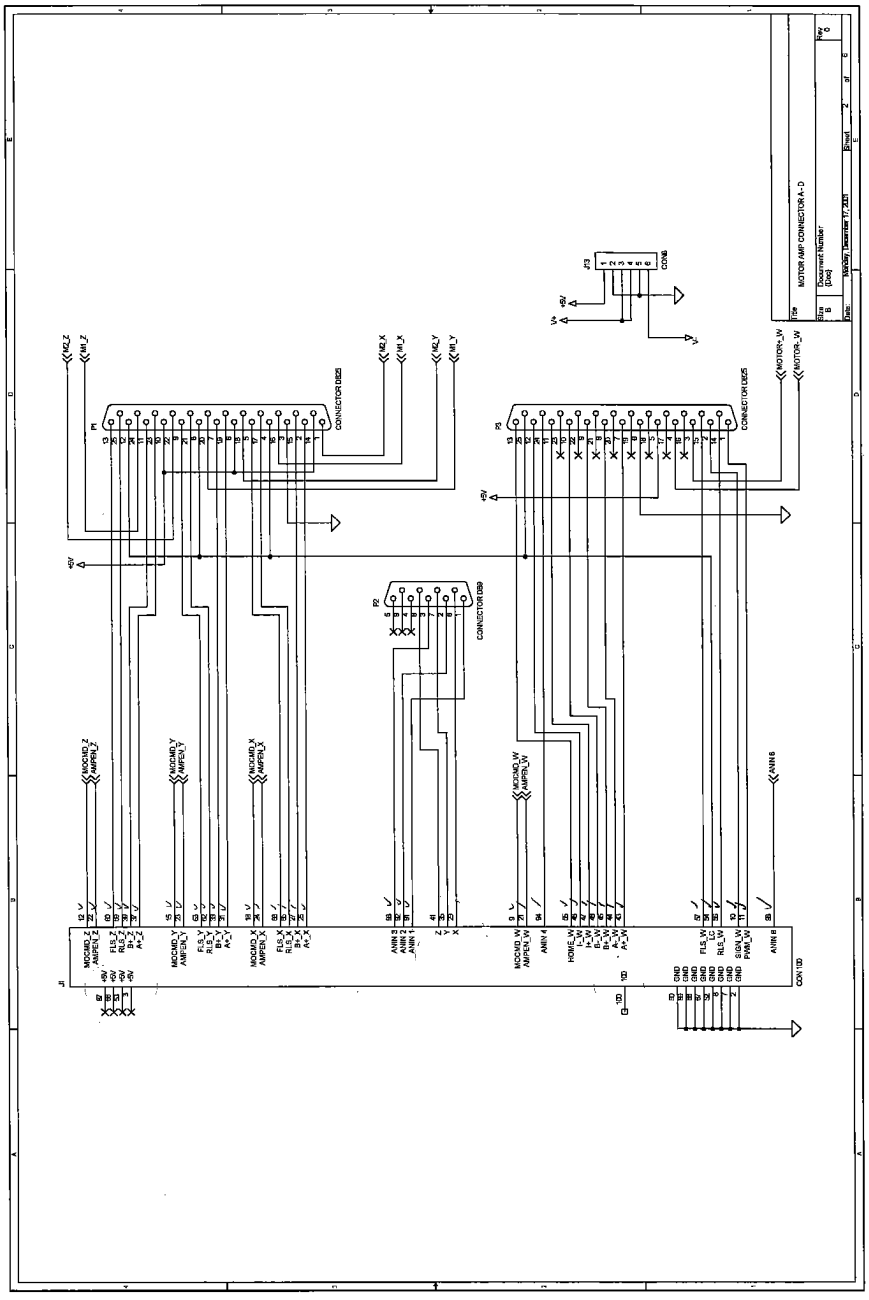
MOTOR AMP CONNECTOR A-D
Document Number:
Thursday, December 17, 2020
CONNECTOR DB25
CONNECTOR DB9
CON10D
+5V
GND

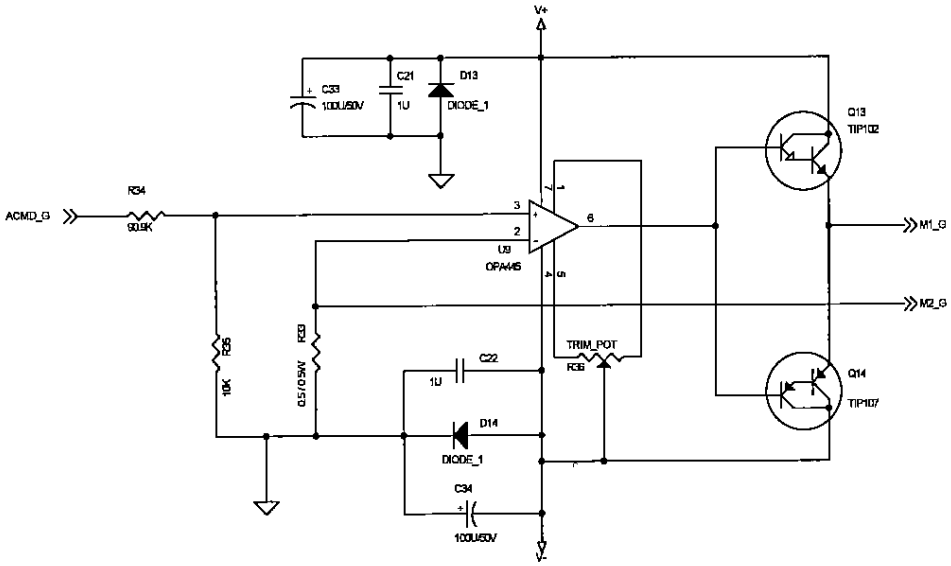
V+
C33
100U/50V
C21
1U
D13
DIODE_1
Q13
TIP102
R34
ACMD_G
90.9K
3
2
6
U9
OPA445
M1_G
M2_G
R35
10K
R33
0.5/0.5W
C22
1U
TRIM_POT
R36
Q14
TIP107
D14
DIODE_1
C34
100U/50V
V-

Appendix C

Multimedia CD

C.1 Progress of the reconstruction algorithm

CD: pyramid_progress.mpg

WWW: http://xray1.physics.sunysb.edu/~tbeetz/publications/thesis/pyramid_progress.mpg

C.2 3D reconstruction

CD: pyramid_3d.avi

WWW: http://xray1.physics.sunysb.edu/~tbeetz/publications/thesis/pyramid_3d.avi

Appendix D

The Fourier transform and its properties

We state here the definition of the Fourier transform and give a brief summary of the most important Fourier transform theorems. For more information and proofs, the reader is referred to the literature [Bracewell 1986].

Definition: The Fourier transform $F_{(\vec{k})}$ of a function $f_{(\vec{x})}$ is

$$\begin{aligned} F_{(\vec{k})} &= \mathcal{F}\{f_{(\vec{x})}\} \\ &= \int_{-\infty}^{\infty} f_{(\vec{x})} e^{-i2\pi\vec{k}\cdot\vec{x}} d\vec{x}. \end{aligned} \tag{D.1}$$

Here the operator $\mathcal{F}\{\}$ is the Fourier transform operator. The inverse Fourier transform is the given as

$$f_{(\vec{x})} = \int_{-\infty}^{\infty} F_{(\vec{k})} e^{i2\pi\vec{k}\cdot\vec{x}} d\vec{k}. \tag{D.2}$$

In the following, we will only consider one-dimensional functions even though the theorems are readily applicable to higher dimensions.

Shift: If a is a real-valued constant, then

$$\mathcal{F}\{f_{(x-a)}\} = e^{-i2\pi ka} F_{(k)} \tag{D.3}$$

Convolution: The convolution of a function $f_{(x)}$ with a function $g_{(x)}$ is written as

$$f_{(x)} \star g_{(x)} = \int_{-\infty}^{\infty} f_{(\xi)} g_{(x-\xi)} d\xi, \tag{D.4}$$

where $\star$ stands for the convolution operator. If we take the Fourier transform, we get

$$\mathcal{F}\{f_{(x)} \star g_{(x)}\} = F_{(k)} G_{(k)}. \tag{D.5}$$

For the convolution of the function $f_{(x)}$ with itself, we can write

$$\mathcal{F}\{f_{(x)} \star f_{(x)}\} \quad = \quad |F_{(k)}|^2, \tag{D.6}$$

which is also described as **autocorrelation**.

Appendix E

Protocol for zone plate imaging with the diffraction chamber

The zone plate is 80 um in diameter and has an outermost zone width of 20 nm. At an energy of 750 eV that corresponds to a focal length of about 1 mm. Described below is a suggested procedure to get the zone plate aligned for taking images of the specimen.

- insert the specimen
- roughly align the zone plate in x and y
- bring the zone plate to about 1.5 mm downstream of the sample
- remove the specimen
- scan the zone plate in x and y (large scan to locate the window - see Figure E.1 a))
- do a smaller scan (see Figure E.1 a)) - note: this membrane is broken, but still has the intact zone plates (3 zone plates) on there
- use the CCD and image the illuminating pinhole (see Figure E.1 c))
- move the zone plate so that you can clearly see the negative and positive first order (see Figure E.1 d))
- bring in the sample (you might want to move DNZ downstream while you insert)
- if you have a lot of objects on the membrane, you should be able to see them in the positive first order see Figure E.1 e))

- move DNZ in increments of about 50 um to get the sample into focus
- you might have to use DNX and DNY (5-10 um steps) to adjust the position of the orders as you move in DNZ
- use GMX, GMY to keep a specimen of interest in the field of view

If you don't have a lot of objects on the membrane, you might want to take out the upstream pinhole and let all the beam hit the specimen (choose a very short exposure time first!). Taking out the pinhole will give you a much larger field of view so that you can look at the surroundings of a cluster etc. as shown in Figure E.1 f) and pick out a region of interest. Since you already know where the illuminating pinhole will be (you can also check that by moving it in again), you can now position GMX and GMY to match the location of the illuminating pinhole. Now you can move the illuminating pinhole back and start recording zone plate images.

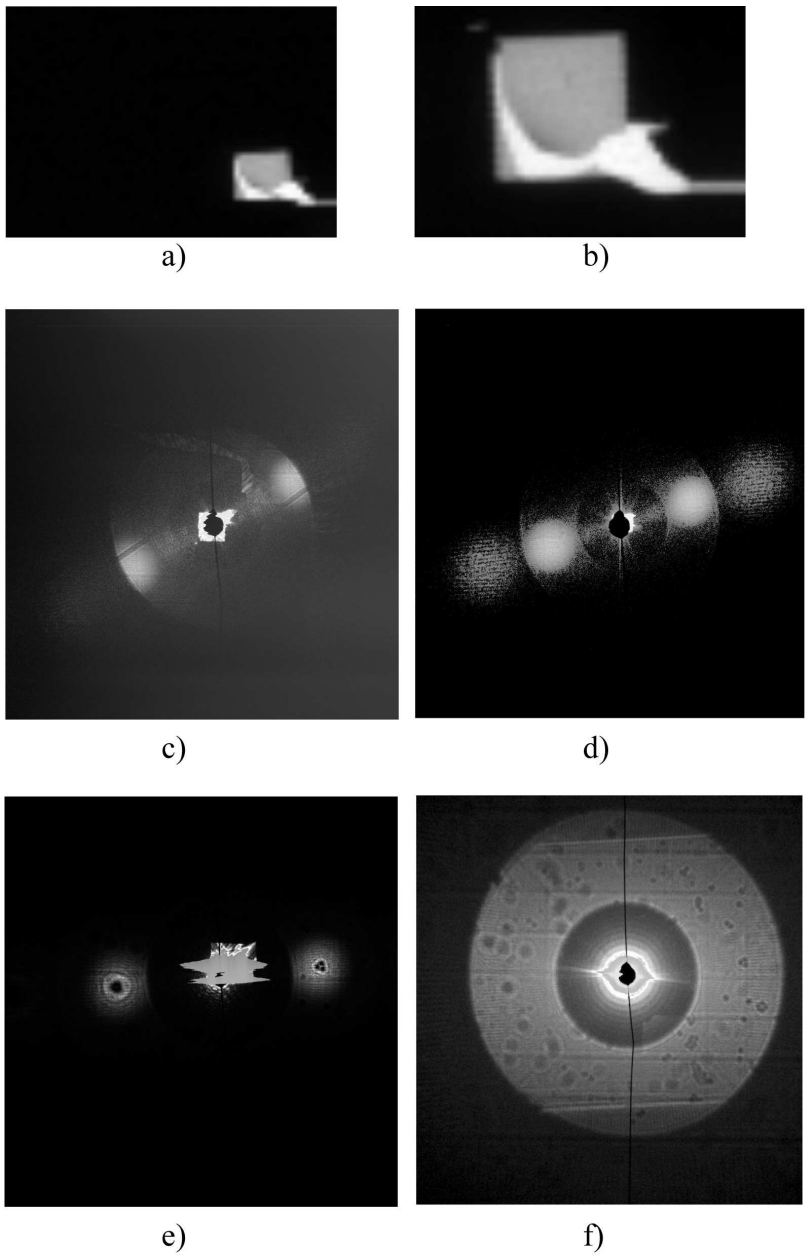

Figure E.1: a), b): scanned images of the zone plate window. c), d): CCD image showing positive and negative out-of-focus image of the illuminating pinhole. e) CCD image of aligned sample. The right image shows the positive first-order image (in focus) and the left side shows the negative first-order image. f) to extent the field of view, the illuminating pinhole can be taken out.

Appendix F

Soft X-ray radiation damage studies in PMMA using a cryo STXM (reprint)

short communications

Soft X-ray radiation-damage studies in PMMA using a cryo-STXM

Tobias Beetz* and Chris Jacobsen

Department of Physics and Astronomy, SUNY Stony Brook, Stony Brook, NY 11794-3800, USA.
E-mail: tobias.beetz@stonybrook.edu

Radiation damage sets a fundamental limit for studies with ionizing radiation; cryo-methods are known to ease these limits. Here, measurements on mass loss and the decrease in the C═O bond density as measured by oxygen-edge XANES (NEXAFS) spectroscopy in thin films of poly(methylmethacrylate) (PMMA), studied in a vacuum, are reported. While cryo-methods allow more than 95% of the mass to remain at doses up to 10^7 Gy, there is little difference in C═O bond density *versus* dose between 298 K and 113 K sample temperatures. At both temperatures the critical dose for bond breaking is $\sim 15 \times 10^6$ Gy.

Keywords: soft X-rays; radiation damage; PMMA; XANES; STXM.

1. Introduction

Radiation damage is a limiting factor in imaging at high resolution with ionizing radiation. Basic considerations of image contrast indicate that doses of $\sim 10^6$ Gy are involved in 50 nm resolution imaging with soft X-rays (Sayre *et al.*, 1977; Gölz, 1992). These doses are sufficient to cause immediate changes in living cells, and to produce noticeable mass loss and shrinkage in some specimens that are wet but chemically fixed (Williams *et al.*, 1993). It is well known that cryo-methods can greatly reduce radiation damage in biological specimens (Glaeser & Taylor, 1978; Dubochet *et al.*, 1987). Cryo-X-ray microscopy experiments at 113 K have shown essentially no observable mass loss at the 50 nm spatial resolution level with radiation doses up to $\sim 10^{10}$ Gy (Schneider, 1998; Maser *et al.*, 2000). However, mass loss is not the only mechanism of radiation damage, and cryo-methods are found to improve but not eliminate degradation of high-resolution electron diffraction data (Glaeser & Taylor, 1978). Overall mass density can be preserved while chemical bonds are not preserved. This suggests that cryo-methods may offer differing degrees of protection for spectroscopy, atomic-resolution imaging or diffraction than simple mass-loss measurements would suggest.

Radiation-damage effects in soft X-ray spectroscopy have been studied by measuring the loss of X-ray absorption near-edge structure (XANES) spectroscopic resonances in thin organic films. Zhang *et al.* (1995) used carbon XANES to monitor the decrease in C═O bond density due to chain scission, and the increase in C═C bond density due to crosslinking, in room-temperature PMMA films that were first baked at various temperatures. The C═O bond density was found to decrease exponentially with increasing dose, with a characteristic dose of $\sim 13 \times 10^6$ Gy. Coffey *et al.* (2002) studied several other thin polymer films with carbon XANES, and investigated the influence of atmospheric oxygen on the radiation-damage chemistry. These authors found that the damage rate in a helium atmosphere is slowed down by a factor of approximately 100 relative to air for their poly-(ethyleneterephthalate) (PET) sample. Their experiments were also conducted at room temperature. These studies provide the background to our goal of examining radiation damage using XANES spectroscopy for samples at cryogenic and room temperatures.

2. Materials and methods

2.1. PMMA sample

A PMMA film prepared on top of a silicon nitride window served as our sample. The silicon nitride window was produced by back-etching silicon from a wafer with a nitride layer grown on it, resulting in 100 nm-thick silicon nitride windows. The PMMA (MW 950 KD PMMA C6 from MicroChem) was spun onto the window at 7000 r.p.m. from a solution 6% by weight in chlorobenzene. We note here that the high molecular weight of the PMMA used should not affect the relative molecular weight reduction since the G-factor is largely independent of the molecular weight (Dawes & Glover, 1996; Smith *et al.*, 2001). The PMMA samples were baked at 423 ± 1 K for 2 h. The thickness of the PMMA layer was then measured using a Tencor Instruments Alpha-Step 200 profiler to be 580 ± 20 nm. The chemical structure of PMMA is shown in Fig. 1.

The carbonyl functional group gives rise to a peak in the oxygen XANES spectra at 531.5 eV (Fig. 3) which is due to the O 1*s*(C═O) $\rightarrow \pi^*_{C=O}$ transition (Tinone *et al.*, 1994). The decrease in intensity of this transition with increasing dose is used later to quantify the damaging effects.

2.2. Experimental description

The data presented here were acquired using the Stony Brook cryo-scanning transmission X-ray microscope (cryo-STXM) (Maser *et al.*, 2000), which is part of the X1A undulator beamline at the National Synchrotron Light Source (Winn *et al.*, 2000). The imaging mode of the cryo-STXM was used to deliver a known dose to the specimen. This was achieved by scanning the specimen with a step size of 40 nm through the focal spot provided by a Fresnel zone plate with a diameter of 160 µm, a central stop diameter of 80 µm and 45 nm outermost zone width. A phosphor-coated photomultiplier tube with 6.6% detection efficiency at 525 eV (see §2.2.3) recorded the transmitted flux at each step. A typical focused flux during exposure was approximately 1.8 MHz, resulting in 1.1 MHz after transmission through the PMMA sample. The incident flux of 1.8 MHz corresponds to a flux density of ~ 7 photons s^{-1} nm^{-2} averaged over the central Airy disc of the zone-plate's point spread function. The exposure at liquid-nitrogen temperature was carried out using a 10 ms pixel dwell time whereas the room-temperature exposure was carried out using a 5 ms pixel dwell time. With the energy of the damaging X-rays tuned to 525.0 eV, the dose during such a scan was approximately 7.0×10^6 Gy at liquid-nitrogen temperature and approximately 3.7×10^6 Gy at room temperature (see §2.3 for details). After the dose scan, the spectroscopy mode of the cryo-STXM was used to record an oxygen XANES spectrum across the oxygen *K*-edge. Since radiation dose is defined as energy

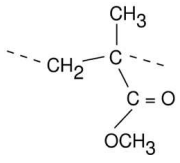

Figure 1
Chemical structure of PMMA.

absorbed per mass, which in turn is proportional to the exposed area, the beam was defocused to ~3.6 µm during spectrum scans to produce a dose of only $\sim 0.6 \times 10^6$ Gy per scan.† The same absorbed energy was therefore put into a larger area, allowing for low-dose spectroscopy. The sequence of dose scan and spectroscopy scan was then repeated about 20 times to give a cumulative dose to the specimen of more than 10^8 Gy. Finally, an in-focus image with a lower dwell time and a larger step size over a larger field was taken to ensure that the specimen remained centred on the X-ray beam axis. Fig. 2 shows such images of dosed regions at both recording temperatures.

To normalize the recorded spectra, a spectrum of an area with no PMMA on the window was recorded at the beginning of each sequence and used as an I_0 spectrum.

2.2.1. Sample conditions. The cryo-STXM with its vacuum chamber was designed to handle specimens cooled to liquid-nitrogen temperature. In the first set of experiments the PMMA sample was cooled down to liquid-nitrogen temperature prior to exposure. The sample was then allowed to warm up to room temperature, before Fig. 2(*c*) was acquired. The second experiment was conducted with the PMMA sample at room temperature.

2.2.2. Energy calibration. To calibrate the energy of the oxygen XANES spectra, we added O_2 gas into the path of the X-ray beam. The strong absorption at 530.82 eV (Hitchcock, 1994) was then used to calibrate the spectra.

2.2.3. Detector calibration. Knowledge of the efficiency of the phosphor-coated photomultiplier detector is important for calculating the exact dose delivered to the sample. This was determined by comparing the count rate on the detector of a collimated beam of focused X-rays with the current measured on a photodiode that has an almost 100% efficiency (Funsten *et al.*, 1997). The measured detector efficiency was about 6.6% at 525 eV.

2.3. Dose calculations

The skin dose (dose deposited in the surface layer of an absorber) can be calculated using the 1/*e* absorption length as

$$\text{Dose} = 1.602 \times 10^{-4} (ENt\mu/\rho A\eta)\ \text{Gy}, \quad (1)$$

where E is the photon energy in eV, N is the number of photons per second absorbed by the sample, measured in kHz, η is the efficiency of the detector, t is the exposure time in ms, ρ is the density in g cm^{-3}, A is the radiated area in µm^2, d is the thickness and μ is the inverse absorption length in µm^{-1}.

The 1/*e* absorption length can be expressed as

$$1/\mu = 2r_e\lambda(N_A/A)\rho f_2,$$

where $r_e = 2.812 \times 10^{-15}$ m, N_A is Avogadro's number, A is the atomic weight and f_2 is the imaginary part of the complex atomic scattering factor, which can be found from tabulated values (Henke *et al.*, 1993). This gave, for example, an assumed absorption length for PMMA of $1/\mu$ = 1.1 µm at 525.0 eV. A typical dose during an exposure was approximately 7.0×10^6 Gy for an exposure at liquid-nitrogen temperature and approximately 3.7×10^6 Gy for an exposure at room temperature. During a spectral scan, a typical dose was $\sim 0.6 \times 10^6$ Gy. Note that the dose in a spectral scan is still a high dose even though we widened the X-ray beam to a diameter of ~3.6 µm and used a short dwell time. The short dwell time is also the reason for the relatively low signal-to-noise ratio in the spectral scan.

2.4. Fitting the spectra

The absorption peak due to the C═O bond density was fitted with a Gaussian. The height of the Gaussian was later used to quantify the loss of the C═O bond density under radiation. We note here that although XANES spectra were recorded at doses exceeding 10^8 Gy we only used data up to $\sim 35 \times 10^6$ Gy for our analysis, since the fit of the C═O bond peak for higher doses could not be made with a high level of certainty.

To determine the mass loss, each spectrum was fitted with an average value at the low-energy (528.0–529.5 eV) and at the high-energy (538.5–540.0 eV) end of the spectrum (Fig. 3). The ratio of the two average values was used to determine the oxygen mass loss as a function of dose using differential absorption analysis (Engström, 1946).

3. Results and discussion

3.1. Spectroscopic observations

To quantify the loss of the carbonyl group, the heights of the C═O absorption peaks determined from the XANES spectra are plotted *versus* the dose in Fig. 4. The data were fitted according to

$$\text{BD} = \text{BD}_\infty + A\exp(-a/a_c), \quad (2)$$

where a is the radiation dose, a_c is called the critical dose for the loss of the C═O bond density and BD_∞ is the remaining C═O bond density after infinite radiation dose. The figure shows both curves for the PMMA sample at liquid-nitrogen and room temperatures. Table 1 summarizes the fitting coefficients obtained.

From the decay rate of the C═O bond density at both temperatures it can be concluded that the specimen temperature has no influence on preserving XANES signatures of the chemical state of the specimen, at least in this example system.

3.2. Mass loss

The dependence of mass loss on dose is shown in Fig. 4 for both temperatures. Following Coffey *et al.* (2002), the mass loss (or loss in optical density) can be quantified by

$$\text{OD} = \text{OD}_\infty + B\exp(-b/b_c), \quad (3)$$

where b is the radiation dose, b_c is called the critical dose and OD_∞ is the remaining optical density after infinite radiation dose. The fitting coefficients are also summarized in Table 1. We note here that, for a confident value of OD_∞ at liquid-nitrogen temperature, more data at

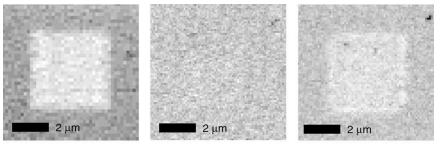

(*a*) (*b*) (*c*)

Figure 2
(*a*) Coarse area scan at room temperature of a region that was dosed at room temperature. The square in the middle indicates the mass loss of the dosed region. (*b*) Coarse area scan at liquid-nitrogen temperature of the region that was dosed at liquid-nitrogen temperature. The image shows no visible mass loss at the dosed region. (*c*) Same area as that in image (*b*) but after warming up the sample; the dosed region becomes visible.

† During a spectrum scan the widened beam will drift slightly off the previously radiated area as we scan to higher energies. From alignment measurements we calculate that drift-off effects become important above 534 eV and reach a maximum at an energy of 540 eV, where 10% of the incident photons will be off the radiated area, corresponding to a systematic error of 0.1 in terms of the optical density.

higher radiation doses would have to be collected. However, since the focus of this report is on spectroscopic limits, we did not investigate higher radiation doses.

Our critical dose of $\sim 18 \times 10^6$ Gy at 525.0 eV for the control experiment at room temperature is in good agreement with the previously obtained value of 13×10^6 Gy at 317 eV by Zhang *et al.* (1995) and 14×10^6 Gy at 315 eV by Coffey *et al.* (2002). The higher dose that we obtained in our measurements may be explained in part by the fact that an additional dose of $\sim 0.6 \times 10^6$ Gy was estimated to be applied while acquiring a spectral scan. As we have seen in §2.3, the dose during a spectral scan is relatively high even though the beam was defocused. A better quantitative measurement of the dose should therefore include more exact information on the dose delivered during such a spectral scan. We also note that the difference may be due to the fact that a different weighting of molecular dissociations is obtained at 525.0 eV than at 315 or 317 eV, respectively.

4. Conclusions

We have shown that the C═O bond in irradiated PMMA is broken at comparable rates at liquid-nitrogen and room temperatures. We have confirmed that cryogenic sample conditions are extremely effective for reducing mass loss, as is required for non-atomic-resolution imaging applications such as nanotomography (Wang *et al.*, 2000; Weiss *et al.*, 2000). However, cryogenic sample conditions do not have a measurable affect on the soft X-ray radiation dose sensitivity of chemical bonds, at least in this model case of XANES spectroscopy of PMMA with no water present. We note that PMMA is much more sensitive to radiation damage than many other polymers, and that there also may be significantly different mechanisms (such as free-radical formation) acting in the case of hydrated organic molecules. Further experiments to study radiation-damage effects on hydrated protein solutions are in preparation.

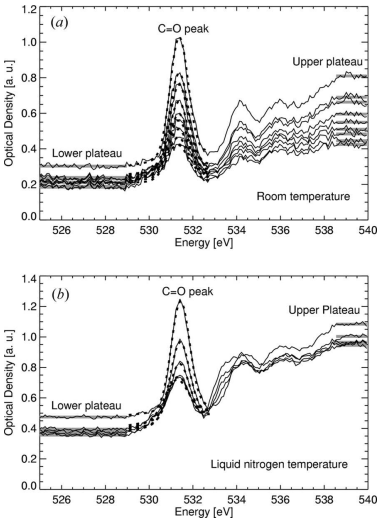

Figure 3
Oxygen XANES spectra of PMMA, showing the dependence on the dose at (*a*) room temperature and (*b*) liquid-nitrogen temperature. The spectra show the decrease of the C═O bond density with increasing dose. The C═O bond peaks were fitted using Gaussians. Also shown are the average values, denoted by upper and lower plateaus, used to determine the oxygen mass loss.

Table 1
Fit coefficients for loss of C═O bond density and mass loss according to equations (2) and (3).

The data and the actual fit are shown in Fig. 4. The critical dose values are given in units of 10^6 Gy. The remaining optical density at 113 K is uncertain owing to the limited range of radiation doses that were probed in this experiment.

	C═O loss			Mass loss		
	A	a_c	BD_∞	B	b_c	OD_∞
298 K	0.81	18	0.18	0.89	34.8	0.12
113 K	0.73	13	0.18	0.89	597	(0.11)

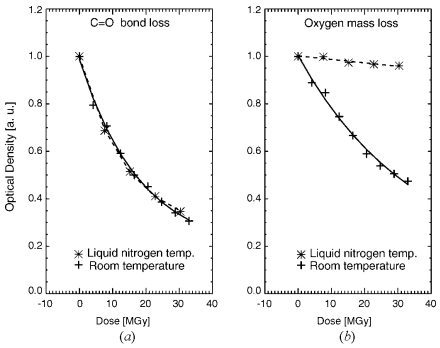

Figure 4
(*a*) Loss of C═O peak intensity and (*b*) mass loss as a function of dose at liquid-nitrogen and room temperatures. The data were fitted using equations (2) and (3), where the fitting coefficients are summarized in Table 1.

We thank Jaan Mannik for the PMMA sample preparation, and Michael Feser, Sue Wirick and Barry Winn for great help with the cryo-STXM and for stimulating discussions. This research was carried out at the National Synchrotron Light Source, Brookhaven National Laboratory, and was supported by the NSF under grants ECS-0099893 and DBI-9986819.

References

Coffey, T., Urquhart, S. G. & Ade, H. (2002). *J. Electron Spectrosc. Relat. Phenom.* **122**, 65–78.
Dawes, K. & Glover, L. C. (1996). *Physical Properties of Polymers Handbook*, edited by J. E. Mark, ch. 41, pp. 557–576. New York: AIP Press.
Dubochet, J., Adrian, M., Chang, J. J., Lepault, J. & McDowall, A. W. (1987). *Cryotechniques in Biological Electron Microscopy*, edited by R. A. Steinbrecht & K. Zierold, pp. 114–131. Berlin: Springer-Verlag.
Engström, A. (1946). *Acta Radiol. Suppl.* **63**, 1–106.
Funsten, H. O., Suszcynsky, D. M., Ritzau, S. M. & Korde, R. (1997). *IEEE Trans. Nucl. Sci.* **44**, 2561–2565.
Glaeser, R. M. & Taylor, K. A. (1978). *J. Microsc.* **112**, 127–138.

Gölz, P. (1992). *X-ray Microscopy III*, edited by A. G. Michette, G. R. Morrison & C. J. Buckley, *Springer Series in Optical Sciences*, Vol. 67, pp. 313–315. Berlin: Springer-Verlag.
Henke, B. L., Gullikson, E. M. & Davis, J. C. (1993). *Atom. Data Nucl. Data Tables*, **54**, 181–342.
Hitchcock, A. P. (1994). *J. Electron Spectrosc. Relat. Phenom.* **67**, 1–132.
Maser, J., Osanna, A., Wang, Y., Jacobsen, C., Kirz, J., Spector, S., Winn, B. & Tennant, D. (2000). *J. Microsc.* **197**, 68–79.
Sayre, D., Kirz, J., Feder, R., Kim, D. M. & Spiller, E. (1977). *Ultramicroscopy*, **2**, 337–341.
Schneider, G. (1998). *Ultramicroscopy*, **75**, 85–104.
Smith, A. P., Spontak, R. J. & Ade, H. (2001). *Polym. Degrad. Stab.* **72**, 519–524.
Tinone, M. C. K., Tanaka, K., Maruyama, J., Ueno, N., Imamura, M. & Matsubayashi, N. (1994). *J. Chem. Phys.* **100**, 5988–5995.
Wang, Y., Jacobsen, C., Maser, J. & Osanna, A. (2000). *J. Microsc.* **197**, 80–93.
Weiss, D., Schneider, G., Niemann, B., Guttmann, P., Rudolph, D. & Schmahl, G. (2000). *Ultramicroscopy*, **84**, 185–197.
Williams, S., Zhang, X., Jacobsen, C., Kirz, J., Lindaas, S., van't Hof, J. & Lamm, S. S. (1993). *J. Microsc.* **170**, 155–165.
Winn, B., Ade, H., Buckley, C., Feser, M., Howells, M., Hulbert, S., Jacobsen, C., Kaznacheyev, K., Kirz, J., Osanna, A., Maser, J., McNulty, I., Miao, J., Oversluizen, T., Spector, S., Sullivan, B., Wang, S., Wirick, S. & Zhang, H. (2000). *J. Synchrotron Rad.* **7**, 395–404.
Zhang, X., Jacobsen, C., Lindaas, S. & Williams, S. (1995). *J. Vac. Sci. Technol.* B**13**, 1477–1483.

Received 5 July 2002 • Accepted 7 February 2003

Appendix G

List of Publications

- T. Beetz, C. Jacobsen,
  Soft X-ray radiation damage studies in PMMA using a cryo-STXM,
  Journal of Synchrotron Radiation **10**: 280-283 (2003)

- T. Beetz, M. Feser, H. Fleckenstein, B. Hornberger, C. Jacobsen, J. Kirz, M. Lerotic, E. Lima, M. Lu, D. Sayre, D. Shapiro, A. Stein, D. Tennant and S. Wirick *Soft X-ray Microscopy at the NSLS,*,
  Synchrotron Radiation News **16** (3): 11-15 (2003)

- T. Beetz, C. Jacobsen and A. Stein,
  Soft X-ray diffraction tomography - Simulations and first results,
  Journal de Physique IV **104**: 27-30 (2003)

- T. Beetz, C. Jacobsen, C. C. Kao, J. Kirz, T. O. Mentes, C. Sanchez-Hanke, D. Sayre and D. Shapiro,
  Development of a novel apparatus for experiments in soft X-ray diffraction imaging and diffraction tomography,
  Journal de Physique IV **104**: 31-34 (2003)

- C. Jacobsen, T. Beetz, M. Feser, A. Osanna, A. Stein and S. Wirick
  Spectromicroscopy of biological and environmental systems at Stony Brook: instrumentation and analysis,
  Surface Review and Letters **9** (1): 185-191 (2002)

- M. Feser, T. Beetz, C. Jacobsen, J. Kirz, S. Wirick, A. Stein and T. Schäfer,
  Scanning transmission soft x-ray microscopy at beamline X1-A at the NSLS - advances in instrumentation and selected applications,
  In D. A. Tichenor, J. A. Folta, editors,
  Soft X-ray and EUV Imaging Systems II **4506**: 146-153 (2001)

- M. Feser, T. Beetz, M. Carlucci-Dayton and C. Jacobsen,
  Instrumentation advances and detector development with the Stony Brook scanning transmission X-ray microscope,
  X-ray Microscopy: Proceedings of the Sixth International Conference, W. Meyer-Ilse, A. Warwick and D. T. Attwood, American Institute of Physics **507**: 367-372 (2000)

- C. Jacobsen, S. Abend, T. Beetz, M. Carlucci-Dayton, M. Feser, K. Kaznacheyev, J. Kirz, J. Maser, U. Neuhäusler, A. Osanna, A. Stein, C. Vaa, Y. Wang, B. Winn and S. Wirick,
  New developments in scanning microscopy at Stony Brook,
  X-ray Microscopy: Proceedings of the Sixth International Conference, W. Meyer-Ilse, A. Warwick and D. T. Attwood, American Institute of Physics **507**: 12-18 (2000)

Bibliography

[ALS 2004] ALS storage ring parameters. *http://www-als.lbl.gov/als/techspecs/srparameters.html*, (2004).

[Aoki 1974] S. Aoki and S. Kikuta. X-ray holographic microscopy. *Japanese Journal of Applied Physics*, **13**, pp. 1385–1392, (1974).

[Baez 1950] A. V. Baez and P. Kirkpatrick. Design and construction of an x-ray microscope. *Physical Review*, **78**(1), p. 83, (1950).

[Baez 1960] A. V. Baez. A self-supporting metal Fresnel zone-plate to focus extreme ultra-violet and soft x-rays. *Nature*, **186**, p. 958, (1960).

[Baez 1961] A. V. Baez. Fresnel zone plate for optical image formation using extreme ultraviolet and soft X radiation. *Journal of the Optical Society of America*, **51**, pp. 405–412, (1961).

[Born 1980] M. Born and E. Wolf. **Principles of Optics**. Pergamon Press, Oxford, sixth edition, (1980).

[Bracewell 1986] R. N. Bracewell. **The Fourier Transform and its Applications**. McGraw-Hill, New York, second revised edition, (1986).

[Buckley 1988] C. J. Buckley, M. T. Browne, R. E. Burge, P. Charalambous, K. Ogawa, and T. Takeyoshi. Zone plates for scanning x-ray microscopy: Contamination writing and efficiency enhancement. In Sayre et al. [Sayre 1988], pp. 88–94.

[Coffey 2002] T. Coffey, S. G. Urquhart, and H. Ade. Characterization of the effects of x-ray irradiation on polymers. *Journal of Electron Spectroscopy and Related Phenomena*, **122**, pp. 65–78, (2002).

[Collier 1971] R. J. Collier, C. B. Burckhardt, and L. H. Lin. **Optical Holography**. Academic Press, New York, (1971).

[Dayton 2000] M. C. Dayton. Nomarski differential phase contrast using a scanning transmission x-ray microscope, (2000). MSI thesis, Department of Physics and Astronomy, State University of New York at Stony Brook.

[Dubochet 1987] J. Dubochet, M. Adrian, J. J. Chang, J. Lepault, and A. W. McDowall. Cryoelectron microscopy of vitrified specimens. In R. A. Steinbrecht and K. Zierold, editors, *Cryotechniques in Biological Electron Microscopy*, pp. 114–131, Berlin, (1987). Springer-Verlag.

[El-Sum 1952] H. M. A. El-Sum and P. Kirkpatrick. Microscopy by reconstructed wavefronts. *Physical Review*, **85**, p. 763, (1952). (abstract).

[Elser 2003] V. Elser. Phase retrieval by iterated projections. *Journal of the Optical Society of America A*, **20**(1), pp. 40–55, (2003).

[Engström 1946] A. Engström. Quantitative micro- and histochemical elementary analysis by Roentgen absorption spectrography. *Acta Radiologica (Supplement)*, **63**, pp. 1–106, (1946).

[Feder 1976] R. Feder, D. Sayre, E. Spiller, J. Topalian, and J. Kirz. Specimen replication for electron microscopy using x rays and x-ray resist. *Journal of Applied Physics*, **47**, pp. 1192–1193, (1976).

[Feser 2000] M. Feser, T. Beetz, M. Carlucci-Dayton, and C. Jacobsen. Instrumentation advances and detector development with the Stony Brook scanning transmission x-ray microscope. In W. Meyer-Ilse, T. Warwick, and D. Attwood, editors, *X-ray Microscopy: Proceedings of the Sixth International Conference*, pp. 367–372, Melville, NY, (2000). American Institute of Physics.

[Feser 2001] M. Feser, T. Beetz, C. Jacobsen, J. Kirz, S. Wirick, A. Stein, and T. Schäfer. Scanning transmission soft x-ray microscopy at beamline X-1A at the NSLS–advances in instrumentation and selected applications. In D. A. Tichenor and J. A. Folta, editors, *Soft X-ray and EUV Imaging Systems II*, volume 4506, pp. 146–153, Bellingham, Washington, (2001). Society of Photo-Optical Instrumentation Engineers (SPIE).

[Fienup 1980] J. R. Fienup. Iterative method applied to image reconstruction and to computer-generated holograms. *Optical Engineering*, **19**(3), pp. 297–305, (1980).

[Fienup 1982] J. R. Fienup. Phase retrieval algorithms: a comparison. *Applied Optics*, **20**(15), pp. 2758–2769, (1982).

[Gabor 1948] D. Gabor. A new microscopic principle. *Nature*, **161**, pp. 777–778, (1948).

[Gabor 1949] D. Gabor. Microscopy by reconstructed wavefronts. *Proceedings of the Royal Academy of Science of London*, **A 197**, pp. 454–487, (1949).

[Gerchberg 1972] R. W. Gerchberg and W. O. Saxton. A practical algorithm for the determination of phase from image and diffraction plane pictures. *Optik*, **35**(2), pp. 237–246, (1972).

[Giles 1969] J. W. Giles, Jr. Image reconstruction from a Fraunhofer x-ray hologram with visible light. *Journal of the Optical Society of America*, **59**, pp. 1179–1188, (1969).

[Glaeser 1978] R. M. Glaeser and K. A. Taylor. Radiation damage relative to transmission electron microscopy of biological specimens at low temperature: a review. *Journal of Microscopy*, **112**, pp. 127–138, (1978).

[Gölz 1992] P. Gölz. Calculations on radiation dosages of biological materials in phase contrast and amplitude contrast x-ray microscopy. In Michette et al. [Michette 1992], pp. 313–315.

[Goodman 1968] J. W. Goodman. **An Introduction to Fourier Optics**. McGraw-Hill, San Francisco, (1968).

[He 2003] H. He, S. Marchesini, M. Howells, U. Weierstall, G. Hembree, and J. C. H. Spence. Experimental lensless soft x-ray imaging using iterative algorithms: phasing diffuse scattering. *Acta Cryst. A*, **69**, pp. 143–152, (2003).

[Hegerl 1976] R. Hegerl and W. Hoppe. Influence of electron noise on three-dimensional image reconstruction. *Zeitschrift für Naturforschung*, **31 a**, pp. 1717–1721, (1976).

[Heimann 1997] P. Heimann, M. Koike, C. Hsu, M. Evans, K. Lu, C. Ng, A. Suits, and Y. Lee. Performance of the chemical dynamics beamline at the advanced light source. *Rev. Sci. Instrum.*, **68**, p. 1945, (1997).

[Henke 1982] B. L. Henke, P. Lee, T. J. Tanaka, R. L. Shimabukuro, and B. K. Fujikawa. Low-energy x-ray interaction coefficients: photoabsorption, scattering, and reflection. *Atomic Data and Nuclear Data Tables*, **27**, pp. 1–144, (1982).

[Henke 1993] B. L. Henke, E. M. Gullikson, and J. C. Davis. X-ray interactions: Photoabsorption, scattering, transmission, and reflection at E=50–30,000 eV, Z=1–92. *Atomic Data and Nuclear Data Tables*, **54**, pp. 181–342, (1993).

[Howells 1984a] M. R. Howells. Possibilities for x-ray holography using synchrotron radiation. In G. Schmahl and D. Rudolph, editors, *X-ray Microscopy*, volume 43 of *Springer Series in Optical Sciences*, pp. 318–335, Berlin, (1984). Springer-Verlag.

[Howells 1984b] M. R. Howells, M. Iarocci, J. Kenney, J. Kirz, and H. Rarback. X-ray holographic microscopy experiments at the Brookhaven synchrotron light source. In F. J. Himpsel and R. W. Klaffky, editors, *Science with Soft X-Rays*, volume 447, pp. 193–203, Bellingham, Washington, (1984). Society of Photo-Optical Instrumentation Engineers (SPIE).

[Howells 1985] M. Howells, J. Kirz, D. Sayre, and G. Schmahl. Soft-x-ray microscopes. *Physics Today*, **38**, pp. 22–32, (Aug. 1985).

[Howells 1986] M. R. Howells, M. A. Iarocci, and J. Kirz. Experiments in x-ray holographic microscopy using synchrotron radiation. *Journal of the Optical Society of America*, **A 3**, pp. 2171–2178, (1986).

[Howells 1987] M. Howells, C. Jacobsen, J. Kirz, R. Feder, K. McQuaid, and S. Rothman. X-ray holograms at improved resolution: a study of zymogen granules. *Science*, **238**, pp. 514–517, (1987).

[Howells 2002] M. R. Howells, P. Charalambous, H. He, S. Marchesini, and J. C. H. Spence. An off-axis zone-plate monochromator for high-power undulator radiation. *Proc. of SPIE*, **4783**, pp. 65–73, (2002).

[Howells 2003] M. R. Howells and J. Kirz. Notes on dose calculations for diffraction imaging. *Private communication, not yet published*, (2003).

[Hubbell 1980] J. H. Hubbell, H. A. Gimm, and I. Øverbø. Pair, triplet, and total atomic cross sections (and mass attenuation coefficients) for 1 MeV–100 GeV photons in elements Z=1–100. *Journal of Physical and Chemical Reference Data*, **9**, pp. 1023–1147, (1980).

[Jackson 1975] J. D. Jackson. **Classical Electrodynamics**. John Wiley & Sons, New York, second edition, (1975).

[Jacobsen 1988] C. Jacobsen. **X-ray holographic microscopy of biological specimens using an undulator**. PhD thesis, Department of Physics, State University of New York at Stony Brook, (May 1988).

[Jacobsen 1990] C. Jacobsen, M. Howells, J. Kirz, and S. Rothman. X-ray holographic microscopy using photoresists. *Journal of the Optical Society of America*, **A 7**, pp. 1847–1861, (1990).

[Jacobsen 1992] C. Jacobsen, J. Kirz, and S. Williams. Resolution in soft x-ray microscopes. *Ultramicroscopy*, **47**, pp. 55–79, (1992).

[Jacobsen 1998] C. Jacobsen, R. Medenwaldt, and S. Williams. A perspective on biological x-ray and electron microscopy. In J. Thieme, G. Schmahl, E. Umbach, and D. Rudolph, editors, *X-ray Microscopy and Spectromicroscopy*, pp. II–93–102, Berlin, (1998). Springer-Verlag.

[Jacobsen 2000] C. Jacobsen, G. Flynn, S. Wirick, and C. Zimba. Soft x-ray spectroscopy from image sequences with sub-100 nm spatial resolution. *Journal of Microscopy*, **197**(2), pp. 173–184, (2000).

[Joyeux 1988] D. Joyeux and F. Polack. Progress in optical reconstruction of submicron x-ray holograms. In R. W. Falcone and J. Kirz, editors, *OSA Proceedings on Short Wavelength Coherent Radiation: Generation and Applications*, volume 2, pp. 295–302, Washington, D. C., (1988). Optical Society of America.

[Kirz 1974] J. Kirz. Phase zone plates for X rays and the extreme UV. *Journal of the Optical Society of America*, **64**, pp. 301–309, (1974).

[Kirz 1980] J. Kirz and D. Sayre. Soft x-ray microscopy of biological specimens. In H. Winick and S. Doniach, editors, *Synchrotron Radiation Research*, pp. 277–322, New York, (1980). Plenum Press.

[Kirz 1995] J. Kirz, C. Jacobsen, and M. Howells. Soft x-ray microscopes and their biological applications. *Quarterly Reviews of Biophysics*, **28**(1), pp. 33–130, (1995). Also available as Lawrence Berkeley Laboratory report LBL-36371.

[Lamvik 1991] M. K. Lamvik. Radiation damage in dry and frozen hydrated organic material. *Journal of Microscopy*, **161**, pp. 171–181, (1991).

[Lindaas 1994] S. A. Lindaas. **X-ray Gabor holography using a scanning force microscope**. PhD thesis, Department of Physics, State University of New York at Stony Brook, (1994).

[Lindaas 1996a] S. Lindaas, M. Howells, C. Jacobsen, and A. Kalinovsky. X-ray holographic microscopy by means of photoresist recording and atomic-force microscope readout. *Journal of the Optical Society of America*, **A 13**(9), pp. 1788–1800, (1996).

[Lindaas 1996b] S. Lindaas, M. R. Howells, C. Jacobsen, J. Miao, and S. Spiller. Experimental demonstration of in-line holography using a ccd. *Unpublished*, (1996).

[Marchesini 2003] S. Marchesini, H. N. Chapman, S. P. Hau-Riege, R. A. London, A. Szoke, H. He, M. R. Howells, H. Padmore, R. Rosen, and J. C. H. Spence. Coherent x-ray diffractive imaging: applications and limitations. *Optics Express*, **11**(19), pp. 2344–2353, (2003).

[Maser 2000] J. Maser, A. Osanna, Y. Wang, C. Jacobsen, J. Kirz, S. Spector, B. Winn, and D. Tennant. Soft x-ray microscopy with a cryo STXM: I. Instrumentation, imaging, and spectroscopy. *Journal of Microscopy*, **197**(1), pp. 68–79, (2000).

[McEwen 1995] B. F. McEwen, K. H. Downing, and R. M. Glaeser. The relevance of dose-fractionation in tomography of radiation-sensitive specimens. *Ultramicroscopy*, **60**, pp. 357–373, (1995).

[Miao 1998] J. Miao, D. Sayre, and H. N. Chapman. Phase retrieval from the magnitude of the Fourier transforms of non-periodic objects. *Journal of the Optical Society of America*, **A 15**(6), pp. 1662–1669, (1998).

[Miao 1999] J. Miao, P. Charalambous, J. Kirz, and D. Sayre. An extension of the methods of x-ray crystallography to allow imaging of micron-size non-crystalline specimens. *Nature*, **400**, pp. 342–344, (1999).

[Miao 2002] J. Miao, T. Ishikawa, B. Johnson, E. Anderson, B. Lai, and K. Hodgson. High resolution 3D x-ray diffraction microscopy. *Physical Review Letters*, **89**(8), p. 088303, (2002).

[Michette 1986] A. G. Michette. **Optical Systems for Soft X Rays**. Plenum, New York, (1986).

[Michette 1992] A. G. Michette, G. R. Morrison, and C. J. Buckley, editors. **X-ray Microscopy III**, volume 67 of *Springer Series in Optical Sciences*, Berlin, (1992). Springer-Verlag.

[Niemann 1974] B. Niemann, D. Rudolph, and G. Schmahl. Soft x-ray imaging zone plates with large zone numbers for microscopic and spectroscopic applications. *Optics Communications*, **12**, pp. 160–163, (1974).

[Niemann 1983] B. Niemann, D. Rudolph, and G. Schmahl. The Göttingen x-ray microscopes. *Nuclear Instruments and Methods in Physics Research*, **208**, pp. 367–372, (1983).

[Niemann 1992] B. Niemann. X-ray microscopy with the Göttingen scanning x-ray microscope at 2.4 nm. In Michette et al. [Michette 1992], pp. 143–146.

[Niemann 1994] B. Niemann, G. Schneider, P. Guttmann, D. Rudolph, and G. Schmahl. The new Göttingen x-ray microscope with object holder in air for wet specimens. In V. V. Aristov and A. I. Erko, editors, *X-ray Microscopy IV*, pp. 66–75, Chernogolovka, Russia, (1994). Bogorodskii Pechatnik. Proceedings of the 4$^{\text{th}}$ International Conference, Chernogolovka, Russia, September 20–24, 1993.

[Nyquist 1928] H. Nyquist. Certain topics in telegraph transmission theory. *Trans. AIEE*, **47**, pp. 617–644, (1928).

[Okada 1970] S. Okada. Cells. In K. I. Altman, G. B. Gerber, and S. Okada, editors, *Radiation Biochemistry*, volume I. Academic Press, New York, (1970).

[Rarback 1988] H. Rarback, D. Shu, S. C. Feng, H. Ade, J. Kirz, I. McNulty, D. P. Kern, T. H. P. Chang, Y. Vladimirsky, N. Iskander, D. Attwood, K. McQuaid, and S. Rothman. Scanning x-ray microscope with 75-nm resolution. *Review of Scientific Instruments*, **59**, pp. 52–59, (1988).

[Rarback 1990a] H. Rarback, C. Buckley, H. Ade, F. Camilo, R. DiGennaro, S. Hellman, M. Howells, N. Iskander, C. Jacobsen, J. Kirz, S. Krinsky, S. Lindaas, I. McNulty, M. Oversluizen, S. Rothman, D. Sayre, M. Sharnoff, and D. Shu. Coherent radiation for x-ray imaging—the soft x-ray undulator and the X1A beamline at the NSLS. *Journal of X-ray Science and Technology*, **2**, pp. 274–296, (1990).

[Rarback 1990b] H. Rarback, C. Buckley, K. Goncz, H. Ade, E. Anderson, D. Attwood, P. Batson, S. Hellman, C. Jacobsen, D. Kern, J. Kirz, S. Lindaas, I. McNulty, M. Oversluizen, M. Rivers, S. Rothman, D. Shu, and E. Tang. The scanning transmission microscope at the NSLS. *Nuclear Instruments and Methods in Physics Research*, **A 291**, pp. 54–59, (1990).

[Rogers 1950] G. L. Rogers. Gabor diffraction microscopy: the hologram as a generalized zone-plate. *Nature*, **166**, p. 237, (1950).

[Rose 1948] A. Rose. Television pickup tubes and the problem of vision. In L. Marton, editor, *Advances in Electronics*, volume 1, pp. 131–166. Academic Press, New York, (1948).

[Rudolph 1990] D. Rudolph, G. Schmahl, and B. Niemann. Amplitude and phase contrast in x-ray microscopy. In P. J. Duke and A. G. Michette, editors, *Modern Microscopies*, pp. 59–67. Plenum, New York, (1990).

[Sayre 1952] D. Sayre. Some implications of a theorem due to shannon. *Acta Cryst.*, **5**, p. 843, (1952).

[Sayre 1972] D. Sayre. Proposal for the utilization of electron beam technology in the fabrication of an image forming device for the soft x-ray region. Technical Report RC 3974 (#17965), IBM T. J. Watson Research Laboratory, Yorktown Heights, New York, (1972).

[Sayre 1977] D. Sayre, J. Kirz, R. Feder, D. M. Kim, and E. Spiller. Transmission microscopy of unmodified biological materials: Comparative radiation dosages with electrons and ultrasoft x-ray photons. *Ultramicroscopy*, **2**, pp. 337–341, (1977).

[Sayre 1980] D. Sayre. Prospects for long-wavelength x-ray microscopy and diffraction. In M. Schlenker, editor, *Imaging Processes and Coherence in Physics*, pp. 229–235. Springer-Verlag, Berlin, (1980).

[Sayre 1988] D. Sayre, M. R. Howells, J. Kirz, and H. Rarback, editors. **X-ray Microscopy II**, volume 56 of *Springer Series in Optical Sciences*, Berlin, (1988). Springer-Verlag.

[Sayre 1991] D. Sayre. Note on "superlarge" structures and their phase problem. In H. Schenk, editor, *Direct Methods of Solving Crystal Structures*, pp. 353–356. Plenum, New York, (1991).

[Sayre 1998] D. Sayre, H. N. Chapman, and J. Miao. On the extendibility of x-ray crystallography to noncrystals. *Acta Crystallographica*, **A 54**, pp. 232–239, (1998).

[Schmahl 1974] G. Schmahl. Holographic structures for applications in the vacuum ultraviolet and soft x-ray region. In E.-E. Koch, R. Haensel, and C. Kunz, editors, *Vacuum Ultraviolet Radiation Physics*, pp. 667–681, London, (1974). Pergamon/Vieweg.

[Schneider 1992] G. Schneider. **Röntgenmikroskopie mit Synchrotronstrahlung an wäßrigen biologischen Systemen—experimentelle und theoretische Untersuchungen**. PhD thesis, Universität Göttingen, (1992).

[Schneider 1998] G. Schneider. Cryo x-ray microscopy with high spatial resolution in amplitude and phase contrast. *Ultramicroscopy*, **75**, pp. 85–104, (1998).

[Shannon 1949] C. E. Shannon. Communication in the presence of noise. *Proc. Institute of Radio Engineers*, **37**, pp. 10–21, (1949).

[Shapiro 2004] D. Shapiro. **Biological Microscopy by Single-Particle X-Ray Diffractive Imaging**. PhD thesis, Stony Brook University, Department of Physics and Astronomy, (2004).

[Soret 1875] J. L. Soret. *Arch. Sci. Phys. Nat.*, **52**, p. 320, (1875).

[Spiller 1977] E. Spiller and R. Feder. X-ray lithography. In H.-J. Queisser, editor, *X-ray Optics (Topics in Applied Physics* **22***)*, pp. 35–92. Springer-Verlag, Berlin, (1977).

[Thieme 1988] J. Thieme. Theoretical investigations of imaging properties of zone plates and zone plate systems using diffraction theory. In Sayre et al. [Sayre 1988], pp. 70–79.

[Tinone 1994] M. C. K. Tinone, K. Tanaka, J. Maruyama, N. Ueno, M. Imamura, and N. Matsubayashi. Inner-shell excitation and site specific fragmentation of poly(methylmethacrylate) thin film. *Journal of Chemical Physics*, **100**(8), pp. 5988–5995, (April 1994).

[Wang 1998] Y. Wang. **Three-dimensional imaging in soft x-ray microscopy**. PhD thesis, Department of Physics & Astronomy, State University of New York at Stony Brook, (1998).

[Wang 2000] Y. Wang, C. Jacobsen, J. Maser, and A. Osanna. Soft x-ray microscopy with a cryo STXM: II. Tomography. *Journal of Microscopy*, **197**(1), pp. 80–93, (2000).

[Weiß 2000] D. Weiß, G. Schneider, B. Niemann, P. Guttmann, D. Rudolph, and G. Schmahl. Computed tomography of cryogenic biological specimens based on x-ray microscopic images. *Ultramicroscopy*, **84**, pp. 185–197, (2000).

[Williams 1993] S. Williams, X. Zhang, C. Jacobsen, J. Kirz, S. Lindaas, J. van't Hof, and S. S. Lamm. Measurements of wet metaphase chromosomes in the scanning transmission x-ray microscope. *Journal of Microscopy*, **170**, pp. 155–165, (1993).

[Williams 2003] G. J. Williams, M. A. Pfeiffer, I. A. Vartanyants, and I. K. Robinson. Three-dimensional imaging of microstructure in au nanocrystals. *Physical Review Letters*, **90**(17), (May 2003).

[Winn 2000a] B. Winn, H. Ade, C. Buckley, M. Feser, M. Howells, S. Hulbert, C. Jacobsen, K. Kaznacheyev, J. Kirz, A. Osanna, J. Maser, I. McNulty, J. Miao, T. Oversluizen, S. Spector, B. Sullivan, S. Wang, S. Wirick, and H. Zhang. Illumination for coherent soft x-ray applications: the new X1A beamline at the NSLS. *Journal of Synchrotron Radiation*, **7**, pp. 395–404, (2000).

[Winn 2000b] B. L. Winn. **Tomography with a cryogenic scanning transmission x-ray microscope**. PhD thesis, Department of Physics and Astronomy, State University of New York at Stony Brook, (Nov. 2000).

[Wood 1934] R. W. Wood. **Physical Optics**. Macmillan, New York, 3rd edition, (1934).

[Yun 1987a] W.-B. Yun. **Contributions to soft x-ray diffraction imaging and diffractive optics**. PhD thesis, Department of Physics, State University of New York at Stony Brook, (Aug. 1987).

[Yun 1987b] W. B. Yun, J. Kirz, and D. Sayre. Observation of the soft X-ray diffraction pattern of a single diatom. *Acta Crystallographica*, **A 43**, p. 131, (1987).

[Zhang 1995] X. Zhang, C. Jacobsen, S. Lindaas, and S. Williams. Exposure strategies for PMMA from *in situ* XANES spectroscopy. *Journal of Vacuum Science and Technology*, **B 13**(4), pp. 1477–1483, (1995).

[Zuo 2003] J. M. Zuo, I. Vartanyants, M. Gao, R. Zhang, and L. A. Nagahara. Atomic imaging of a carbon nantube from diffraction intensities. *Science*, **300**, pp. 1419–1421, (May 2003).